AD NUMBER
AD857639
LIMITATION CHANGES
TO: **Approved for public release; distribution is unlimited.**
FROM: **Distribution authorized to U.S. Gov't. agencies and their contractors; Administrative/Operational Use; APR 1969. Other requests shall be referred to Army Aviation Materiel Labs., Fort Eustis, VA.**
AUTHORITY
USAAMRDL ltr 18 Jun 1971

AD

USAAVLABS TECHNICAL REPORT 69-7

THE AERODYNAMIC AND AEROELASTIC CHARACTERISTICS OF A FULL-SCALE ROTOR BLADE STOPPED IN FLIGHT

By

Richard P. White, Jr.

April 1969

U. S. ARMY AVIATION MATERIEL LABORATORIES
FORT EUSTIS, VIRGINIA

CONTRACT DA 44-177-AMC-366(T)
CORNELL AERONAUTICAL LABORATORY, INC.
BUFFALO, NEW YORK

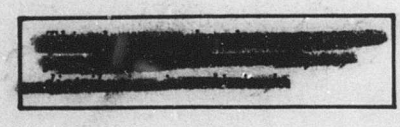

141

DEPARTMENT OF THE ARMY
U. S. ARMY AVIATION MATERIEL LABORATORIES
Fort Eustis, Virginia 23604

ERRATUM

US AAVLABS Technical Report 69-7
TITLE: The Aerodynamic and Aeroelastic Characteristics of a Full-Scale Rotor Blade Stopped in Flight

Delete the statement on cover, title page, and block 10 of DD Form 1473 which reads

> "This document has been approved for public release and sale; its distribution is unlimited."

and replace with the following statement:

> "This document is subject to special export controls, and each transmittal to foreign governments or foreign nationals may be made only with prior approval of US Army Aviation Materiel Laboratories, Fort Eustis, Virginia 23604."

DEPARTMENT OF THE ARMY
HEADQUARTERS US ARMY AVIATION MATERIEL LABORATORIES
FORT EUSTIS, VIRGINIA 23604

This report has been reviewed by the U.S. Army Aviation Materiel Laboratories and is considered to be technically sound.

The report is published for the dissemination of information and the stimulation of research. The basic data from which the report was developed have been compiled and will be held on file at the U.S. Army Aviation Materiel Laboratories. These data can be made available on a limited basis to parties interested in performing further related research.

Task 1F162204A13902
Contract DA 44-177-AMC-366(T)
USAAVLABS Technical Report 69-7
April 1969

THE AERODYNAMIC AND AEROELASTIC CHARACTERISTICS OF A FULL-SCALE ROTOR BLADE STOPPED IN FLIGHT

Final Report

CAL Report BB-2296-S-1

By
Richard P. White, Jr.

Prepared by
Cornell Aeronautical Laboratory, Inc.
Buffalo, New York

for

U. S. ARMY AVIATION MATERIEL LABORATORIES
FORT EUSTIS, VIRGINIA

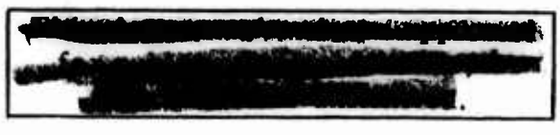

SUMMARY

This report presents the results of a research program to obtain simultaneously a set of blade strain and air-load data for a blade of a stoppable rotor configuration arbitrarily oriented with respect to the free stream. The research program summarized herein obtained data for such a blade configuration over a wide range of shaft tilt angles, blade pitch angles, and azimuth angles during a wind-tunnel test program conducted in the NASA-Ames 40-by-80-foot wind tunnel.

The main results of the program were as follows:

At azimuth angles of 90 and 270 degrees, the variations of the aerodynamic characteristics with angle of attack were generally those that might be expected on the basis of sectional data.

The effect of blade beamwise flexibility is very significant as regards the variation of the aerodynamic characteristics with azimuth angle.

In the azimuth angle range of $225 \leq \psi \leq 330$ degrees, an instability was encountered for both positive and negative blade pitch angles.

The contribution of the flexible blade bending slope to the effective angle of attack was significant in the establishment of the instability boundary.

A linearized lifting-surface theory for estimating aerodynamic forces on the stopped rotor blade was formulated. Limited comparisons were made with test results and with other theoretical solutions.

FOREWORD

This report on the work that was accomplished during the contract effort to investigate the aerodynamic and aeroelastic characteristics of a full-scale rotor blade stopped in flight has been prepared in two parts. This report presents a detailed discussion of all aspects of the program and the analysis of the results that were obtained. All of the basic data that were collected during the test phase of the program are on file at the U. S. Army Aviation Materiel Laboratories (USAAVLABS).

The research program was conducted by the Cornell Aeronautical Laboratory, Inc. (CAL) under USAAVLABS Contract DA 44-177-AMC-366(T) (Task 1F162204A13902) and was carried out under the technical cognizance of Mr. William E. Nettles of USAAVLABS.

The research program began in July 1966 and was completed in June 1968. Personnel associated with the research program included Richard P. White, Jr., Eugene Skelly, Stephen King, and Joseph Nenni of CAL. Mr. John McCloud of the NASA-Ames research staff contributed many valuable suggestions during the formulation and conduct of the tests in the full-scale tunnel and was the NASA project engineer during the test phase of the program.

BLANK PAGE

TABLE OF CONTENTS

LIST OF ILLUSTRATIONS

LIST OF ILLUSTRATIONS (Cont'd)

LIST OF ILLUSTRATIONS (Cont'd)

LIST OF TABLES

LIST OF SYMBOLS

b	half span of blade, ft
BMR	root beamwise moment as measured by the balance system, ft-lbs
c	half chord of blade, ft
D	drag force parallel to free-stream velocity at blade root, lbs
DM	drag moment at blade root, ft-lbs
E	modulus of elasticity, psi
EFR	root edgewise force measured by the balance system, lbs
EMR	root edgewise moment measured by the balance system, ft-lbs
G	shear modulus, psi
I	area moment bending, $in.^4$
J	area moment torsion, $in.^4$
L	lift force perpendicular to free-stream velocity at blade root, lbs
LS	indicates lower surface
NFR	root normal force as measured by the balance system, lbs

PM	pitching moment at blade root, ft-lbs
PMR	root pitching moment about quarter chord as measured by the balance system, ft-lbs
q	dynamic pressure, psf
R	rotor radius, ft
RM	blade rolling moment at blade root, ft-lbs
TS	indicates top surface
V	free-stream velocity, ft/sec
$X_1 = PMR(1)$	signal from root pitching moment balance beam No. 1, volts
$X_2 = PMR(2)$	signal from root pitching moment balance beam No. 2, volts
$X_3 = BMR(1)$	signal from root beamwise moment balance beam No. 1, volts
$X_4 = BMR(2)$	signal from root beamwise moment balance beam No. 2, volts
$X_5 = EMR$	signal from root edgewise moment balance beam, volts
$X_6 = FFR$	signal from root edgewise force balance beam, volts
α_s	shaft tilt angle or angle of rotor head baseplate with respect to the airstream, positive nose up, deg

$\alpha(x,y)$	angle between the local tangent to the mean camber line and the wind reference in the plane containing the wind vector, rad
γ	bound vorticity distribution representing rotor blade
$\theta^* = (\alpha_s + \theta_R \sin\psi)$	composite blade angle at blade root for azimuth angles from 180 to 360 degrees, positive trailing edge down, deg
θ_R	angle of instrumented blade (red) at root with respect to the rotor head baseplate, positive nose up, deg
θ_W	angle of dummy blade (white) at root with respect to the rotor head baseplate, positive nose up, deg
ψ	azimuth angle of instrumented blade, zero in downstream position, positive in counterclockwise direction, deg

INTRODUCTION

During the past decade, the flight speed obtainable with VTOL aircraft has more than doubled. The reason for this rapid increase in flight speed has been twofold: the rapid advance in VTOL technology and the introduction of the lightweight free-turbine engine. The latest advances in flight have been made with compound-type helicopters in which the rotor is slowed and unloaded by means of a lifting surface. It is reasonable to anticipate that the next development step would be toward a stopped rotor configuration in which the rotor now being carried on a compound vehicle would be completely unloaded, decelerated, stopped, locked in position, and trailed or stowed.

Stoppable rotors will necessarily traverse a peculiar operating range. During the last revolution of the rotor, before coming to a complete stop, the blades will effectively vary in behavior between that of a high-aspect-ratio wing at azimuth positions of 90 degrees and 270 degrees to a very low-aspect-ratio wing at 0 degrees and 180 degrees. The aerodynamic load amplitude and distribution on a blade would be expected to undergo large variations during this transition from "high- to low-aspect-ratio" operation and strong nonlinear effects can be anticipated as well as the possibility of aeroelastic problems such as static divergence and flutter.

There is no verified theory for predicting the aerodynamic loads needed to study the blade deformations and stability of rotors stopped at any arbitrary azimuth position in flight. If stoppable rotor configurations are, in fact, going to be developed on a consistent and rational basis, then there is a need for a proven method of predicting the loads developed by such a rotor system in flight. The primary purpose of the research effort reported herein, therefore, was to obtain a set of aerodynamic loading data that was consistent with the resultant blade deformations for a range of pertinent aircraft flight and control parameters for use in checking the validity of any theoretical prediction method that is developed. A secondary purpose of the research effort was to develop a linearized aerodynamic prediction method which includes the effects of blade deformation in order to determine, through comparison with experimental results, the degree to which such a linearized theory could predict the measured results.

This report describes the test equipment, its operation and calibration, and the development of the theoretical prediction method; it presents and discusses the major experimental and theoretical results that were obtained during the research program. The detailed pressure measurements, blade strain data, and integrated blade loading data for the approximately 750 configurations tested are on file at USAAVLABS.

DISCUSSION

A. EQUIPMENT AND TEST APPARATUS

The purpose of the test program was to obtain simultaneously aerodynamic and structural deformation data for a "typical" full-scale rotor blade in a stopped configuration. A special blade-retention structure was constructed that incorporated all of the desired test features for the efficient conduct of the experimental program, and a set of specially instrumented blades that had been constructed previously and tested in a normal helicopter rotor configuration was used as the basic rotor.

The special two-bladed test rotor system that was assembled for the program is shown ready for test in the NASA-Ames 40-by-80-foot wind tunnel in Figure 1. While a two-bladed rotor system was used for the tests, only one blade was fully instrumented to measure the chordwise pressure distributions at six spanwise stations, and the beamwise bending, edgewise bending, and torsional strains at nine spanwise stations. In addition to these quantities, the normal force, beamwise moment, edgewise force, edgewise moment, and pitching moment at the root of the instrumented blade were measured by a five-component balance system which held the root of the blade. Rotor azimuthal position, root angle of attack of each of the two blades, and rotor shaft angle (in the plane of the windstream) were remotely controlled from a console outside the tunnel.

Figure 2 presents a dimensional drawing giving the pertinent dimensions of the test installation in the wind tunnel. Figure 3 presents a close-up view of the rotor-head assembly showing the various drive systems. The blade pitch and shaft tilt drives were linear ball-screw actuators that were designed to change the respective angles at a rate of 1/2 degree per second, and the azimuth drive was designed to rotate the rotor system at a rate of 1 degree per second. The blade pitch-control actuators were driven by a high-speed motor, and thus a large-speed reduction was required to obtain the slow rates of blade pitch-angle change. However, because of the extremely small amount of friction in the ballscrew actuator, the use of a brake was required to keep the applied aerodynamic load from rotating the actuator system after the drive motor had been turned off. This was accomplished by means of a small friction brake that was controlled through a solenoid that released the brake when electrical power was applied to the drive motor. As can be seen from Figure 3, the blade pitch drive for the instrumented blade (designated the red blade) was connected to the inner housing of the balance system.

Figure 4 shows the overall details of the balance system. The outer balance housing was fixed to the head assembly, and the inner balance housing rotated inside the outer housing on two large radial bearings.

One side of each balance flexure was attached to the inner housing, and the other side of the flexure was attached to the blade grip retention. The center of rotation of the balance was coincident with the quarter chord of the blade. As previously noted, the blade angle of attack was changed by rotating the entire blade-balance unit (inner balance housing). The balance, therefore, always measured the forces and moments perpendicular and parallel to the root chord of the blade.

The disc brake shown in Figure 4 was used to lock out the small amount of blacklash in the azimuth drive train once the desired rotor azimuth position had been obtained. The brake was an electrohydraulic system remotely controlled by the test operator in the control room.

Figure 5 is a dimensional drawing which shows the arrangement of the force-beam flexures in the balance system and a detailed sketch of a typical force-beam flexure. As can be seen from the force-beam layout, the root edgewise moments (*EMR*) and the root beamwise moments (*BMR*) were measured by pairs of force beams on approximately 2-foot centers. The root edgewise force (*EFR*) was measured by a single force beam, and the root normal force (*NFR*) and root pitching moment (*PMR*) were both measured by the same set of force beams spaced on 16-inch centers. To obtain the *NFR*, the strain signals from the two force beams were added electrically; to obtain the pitching moment, the strain signals were subtracted electrically.

The detailed sketch of a typical force beam shows how a built-in stress concentration was used to facilitate the attainment of a large signal from the strain gages while maintaining a very rigid balance system. While a certain amount of crosstalk is obtained from such a balance arrangement, it has been shown from experience that, by means of a proper calibration procedure whereby all cross couplings are measured, very accurate force and moment measurements can be obtained. The load ranges to which the present balance system was designed are as follows:

root normal force	(*NFR*)	±1,200 lbs
root edgewise force	(*EFR*)	±500 lbs
root beamwise moments	(*BMR*)	±11,000 ft-lbs
root edgewise moments	(*EMR*)	±5,000 ft-lbs
root pitching moments	(*PMR*)	±920 ft-lbs

The rotor blades that were used for the tests were the instrumented UH-1A blades previously used in 1962 to obtain the blade airload data obtained in flight and presented in Reference 1. A complete and detailed description of the rotor blades can be found in that reference. The blade geometric properties are presented in Figure 6, the blade mass distribution is presented in Figure 7, the blade mass inertia

distribution is presented in Figure 8, the blade-bending stiffness distributions are presented in Figure 9, and the blade torsional stiffness distribution is presented in Figure 10. In the configuration with which the present tests were conducted, the 15-1/4-inch constant-chord rotor blade has a diameter of approximately 45 feet. The trim tab (similar to the one shown on the dummy blade in Figure 1) was removed from the instrumented blade so that, when the blade's trailing edge was facing the airstream, the flow would not be disturbed by the protruding tab.

The transducers located on the test blade were of two types: strain gages to measure the beamwise, edgewise, and torsional strains at nine spanwise stations, and pressure gages to measure the chordwise pressure distributions at six spanwise stations. Figure 11 shows the spanwise location of the strain gages and pressure gages, and Table I lists the chordwise location and pressure range of each pressure gage on the blade. Figure 12 shows both the pressure-gage and the strain-gage installation at approximately 85-percent span. As can be seen, the strain-gage installation is a relatively standard one using four active gages for each of the three independent strain readings. This type of strain-gage installation was used instead of rosettes, as the majority of the strain-gage instrumentation previously installed for use in the flight-loads program was not of the rosette type (Reference 1) and was adaptable for the present tests.

In the pressure-gage installations, two types of gages were used: a NACA-developed miniature differential pressure transducer previously installed in the blade (Reference 1) and an absolute pressure transducer (Reference 2). The differential gages measured the differences between the upper and lower surface pressures. The absolute pressure gages were used to measure the differences between the wind-on and wind-off surface pressures. The absolute pressure transducers were installed only at the 85-percent span station in an attempt to obtain a more complete definition of the pressure distribution than would have been available from the existing differential gages. As can be seen from Figure 12, a chordwise epoxy fairing was made for the 85-percent span station in an attempt to mount the absolute surface gages external to the blade without disrupting the airflow. Prior to testing, the recesses in the epoxy fairing for the gages were filled with a soft plastic to smooth the contour.

A 10-volt, 3,000-cps excitation supplied by a power amplifier was used to excite both the strain gages and pressure transducers.

Figure 13 shows the installation of the transducers used to measure the blade pitch angles of the instrumented and dummy blades with respect to the rotor-head baseplate. The transducers for both blades were one-turn, precision rotary potentiometers mounted at

Table I
LOCATIONS AND RANGES OF PRESSURE GAGES

CHORDWISE STATION (% CHORD)	SPANWISE STATION (% radius)					
	41.1 (psi)	55.7 (psi)	75.4 (psi)	85.2 (psi)	90.1 (psi)	95.0 (psi)
2.1	-	15	15	15	15	15
3.7	8	-	-	15	-	-
9.0	-	15	15	15	15	15
12.9	-	-	-	15	-	-
16.9	8	8	-	15	15	15
22.6	-	8	-	15	15	-
33.5	4	-	-	-	-	-
47.8	-	-	-	4	-	-
62.0	1	2	2	2	4	-
68.9 UPPER SURFACE	-	-	-	5-20*	-	-
68.9 LOWER SURFACE	-	-	-	5-20*	-	-
75.4	-	-	-	2	-	-
82.0 UPPER SURFACE	-	-	-	5-20*	-	-
85.9	1	-	-	-	-	-
88.0	-	1	1	2	2	2
94.1 UPPER SURFACE	-	-	-	5-20*	-	-
94.1 LOWER SURFACE	-	-	-	5-20*	-	-
97.0 UPPER SURFACE	-	-	-	5-20*	-	-
97.0 LOWER SURFACE	-	-	-	5-20*	-	-

*ABSOLUTE GAGES

the center of rotation of the inner housing of the balance for the instrumented blade and at the center of rotation of the blade-bearing housing for the dummy blade. Both potentiometers were powered by a stabilized 40-volt dc power unit.

Figure 14 is a close-up photograph of the rotor head installed in the tunnel prior to testing. The transducers used to measure the shaft angle and azimuth angle can be clearly seen in this picture. The transducer used to measure the shaft angle was a 270-degree precision rotary potentiometer mounted at the center of the shaft tilt bearing housing. The azimuth angle transducer was a 10-turn rotary potentiometer driven through a friction contact with the azimuth brake disc (Figure 4). One revolution of the rotor head corresponded to approximately eight turns of the rotary potentiometer.

Since the azimuth potentiometer was driven by the brake disc through a friction contact, a wind screen (not shown in the photograph) was used to prevent the airstream from altering the contact pressure and a remote means (optical) of checking on possible slippage was used to monitor the performance of the transducer. A fuller discussion of the remote optical check system is presented in the section describing the operational procedures followed during the wind tunnel tests.

All transducer signals, position transducers, pressure gages, strain gages, etc., were recorded both on a digital readout system installed in the control room of the NASA-Ames 40-by-80-foot full-scale wind tunnel (Datex II) and by two 50-channel, type 7-119 oscillographs. The two readout systems were employed to insure that, if the primary digital data recording system (Datex II) malfunctioned, backup direct analog traces would be available to obtain the desired data. In addition, if other than "static conditions" prevailed, time analog traces would be recorded. The latter was the primary reason that the analog backup system was believed to be needed, as it was suspected that the blade would not remain stationary, under certain test conditions, for the relatively long time required by the Datex II unit to punch all the data on digital cards (approximately 12 seconds). Because of mismatched impedances, the analog and digital data could not be recorded simultaneously. A switching system was developed, therefore, to place all the transducer signals on either the Datex II system or the analog recording system. Figure 15 presents a block diagram of the entire instrumentation system and indicates the switching arrangement that was used.

Figure 16, a photograph of the instrumentation installed in the wind tunnel control room, shows the eight banks of amplifiers and the switching box for signal transfer to either the digital recorder or the CEC recording oscillographs, which are also shown in the photograph.

Figure 17 is a photograph of the Datex II strip chart readout, which permitted an immediate inspection of the data that were being punched for each channel on the cards during every cycle of data taking.

Figure 18 is a photograph of the test operator's control panel. All the controls and appropriate readouts of blade pitch angle and blade stress for the dummy blade (white blade) were on the left, and the control panel and readouts for the instrumented blade (red blade) were on the right. The readouts and controls for azimuth angle and shaft tilt angle common to both blades were in the center part of the control panel.

Each drive system had two switches: one to turn the power on or off to the respective control, and a three-position, spring-loaded switch to drive the control in either a plus or a minus direction. At the top center of the control panel was a multichannel selector switch which allowed the appropriate signals to be accurately read out on a digital voltmeter. The blade pitch angles, shaft tilt angle, azimuth angle, control system voltages, and instrumentation voltages were all set and checked by means of the digital voltmeter so that accurate parameter values could be obtained. It should be noted that the readout dials on the control panel were used only as a quick visual indication of the rotor and blade positions and that the digital voltmeter and the recording systems were used to set and record accurate values of the parameters.

B. EQUIPMENT CHECKOUT AND CALIBRATION

Prior to shipment of the rotor system to the NASA-Ames 40-by-80-foot wind tunnel for tests, the entire system was assembled and checked out for proper operation. In addition, all major instrumentation systems were completely and carefully calibrated so that only check calibration would be required after installation in the tunnel. The primary measurement subsystems were calibrated independently, and then as a complete unit. These subsystems were the amplifier-analog recording system, the force-moment balance at the root of the instrumented blade, the various position transducers, the pressure transducers on the blade, and the strain gages mounted on the instrumented blade. The digital recording system installed in the control room of the wind tunnel at Ames was set and calibrated after the rotor system had been mounted in the test section. The following sections of the report will discuss the calibration procedures and results obtained for each of the measurement subsystems that were calibrated independently.

Amplifier-Analog Recording System

The amplifier-recording system was calibrated in two steps. The amplifier input-to-output voltage amplification for each attenuator setting was checked to insure that the specified ratios were accurate to within 1 percent, and then the galvometer deflections in the recording oscillograph were determined for each transducer channel in terms of the voltage output of the amplifiers. Table II presents the recorded trace deflection of each transducer channel per volt input to the associated amplifier set at an attenuation of unity.

Table II

AMPLIFIER-OSCILLOGRAPH CALIBRATION CONSTANTS

TRANSDUCER	TRACE IDENTIFICATION		SPANWISE LOCATION (% SPAN)	CHORDWISE LOCATION (% CHORD)	CALIBRATION CONSTANT (volts/in. OF TRACE DEFL.) (AT AMPLIFIER ATTENUATION = 1)
	OSCILLOGRAPH NUMBER	GALVANOMETER NUMBER			
STRAIN GAGES INSTRUMENTED BLADE					
BEAM BENDING	1	9	93.0	-	0.116
BEAM BENDING	1	8	86.9	-	0.114
BEAM BENDING	1	7	80.7	-	0.115
BEAM BENDING	1	6	70.8	-	0.117
BEAM BENDING	1	5	61.0	-	0.116
BEAM BENDING	1	4	51.1	-	0.113
BEAM BENDING	1	3	37.3	-	0.113
BEAM BENDING	1	2	29.4	-	0.114
BEAM BENDING	1	1	16.6	-	0.132
EDGE BENDING	1	21	93.0	-	0.106
EDGE BENDING	1	20	86.9	-	0.115
EDGE BENDING	1	19	80.7	-	0.112
EDGE BENDING	1	18	70.8	-	0.112
EDGE BENDING	1	17	61.0	-	0.112
EDGE BENDING	1	16	51.1	-	0.109
EDGE BENDING	1	15	37.3	-	0.112
EDGE BENDING	1	14	29.4	-	0.108
EDGE BENDING	1	13	16.6	-	0.113
TORSION	1	35	93.0	-	0.115
TORSION	1	34	86.9	-	0.112
TORSION	1	33	80.7	-	0.116
TORSION	1	32	70.8	-	0.113
TORSION	1	31	61.0	-	0.114
TORSION	1	30	51.1	-	0.111
TORSION	1	29	37.3	-	0.112
TORSION	1	28	29.4	-	0.116
TORSION	1	27	16.6	-	0.112
BALANCE BEAMS					
X1	2	39	-	-	0.096
X2	2	40	-	-	0.092
X3	2	41	-	-	0.094
X4	2	42	-	-	0.099
X5	2	43	-	-	0.090
X6	2	44	-	-	0.096

Table II - Continued

TRANSDUCER	TRACE IDENTIFICATION		SPANWISE LOCATION (% SPAN)	CHORDWISE LOCATION (% CHORD)	CALIBRATION CONSTANT (volts/in. OF TRACE DEFL.) (AT AMPLIFIER (ATTENUATION = 1)
	OSCILLOGRAPH NUMBER	GALVANOMETER NUMBER			
DIFFERENTIAL PRESSURE GAGES	2	1	41.1	3.7	0.105
	2	2	41.1	16.9	0.100
	1	12	41.1	33.5	0.116
	1	39	41.1	62.0	0.116
	1	40	41.1	85.9	0.117
	2	3	55.7	2.1	0.106
	2	4	55.7	9.0	0.107
	2	5	55.7	16.9	0.103
	2	6	55.7	22.6	0.102
	1	41	55.7	62.0	0.114
	1	42	55.7	88.0	0.112
	2	13	75.4	2.1	0.102
	2	14	75.4	9.0	0.104
	1	43	75.4	62.0	0.118
	1	44	75.4	88.0	0.112
	2	7	85.2	2.1	0.107
	2	8	85.2	3.7	0.106
	2	9	85.2	9.0	0.105
	2	10	85.2	12.9	0.105
	2	11	85.2	16.9	0.103
	2	12	85.2	22.6	0.103
	1	36	85.2	47.8	0.114
	1	45	85.2	62.0	0.121
	1	46	85.2	75.4	0.114
	1	47	85.2	88.0	0.115
	2	17	90.1	2.1	0.103
	2	18	90.1	9.0	0.105
	2	19	90.1	16.9	0.104
	2	20	90.1	22.6	0.105
	1	37	90.1	62.0	0.112
	1	50	90.1	88.0	0.118
	2	21	95.0	2.1	0.105
	2	22	95.0	9.0	0.100
	2	23	95.0	16.9	0.103
	1	49	95.0	88.0	0.114
ABSOLUTE PRESSURE GAGES					
TOP SURFACE	2	29	85.2	68.9	0.096
LOWER SURFACE	2	30	85.2	68.9	0.095
TOP SURFACE	2	31	85.2	82.0	0.085
TOP SURFACE	2	33	85.2	94.1	0.099
LOWER SURFACE	2	34	85.2	94.1	0.095
TOP SURFACE	2	35	85.2	97.0	0.098
LOWER SURFACE	2	36	85.2	97.0	0.098

The Balance System

The balance system was calibrated by the instrumentation-calibration group of CAL's Transonic Wind Tunnel Department, which has been responsible for the instrumentation and calibration of all the balance systems developed for use in that facility. The balance was calibrated by applying known loads in each of the six balance-component directions independently. The balance was also subjected to known combined loadings. The data from these calibrations were used to determine the matrix relating the applied loads to the balance output signals. The differences in the calibration constants between positive and negative loadings were also determined. The balance conversion matrix (balance beam transducer outputs to loads) as determined during calibration is presented in Figure 19. The plus or minus sign in front of each row of the conversion matrix indicates which set of numbers in each row should be used for either a positive or a negative load. Care had to be used during data reduction, therefore, to insure that the correct set of matrix elements was used. It is noted, however, that if the balance beam signals X_1 through X_6 resulting from a positive normal force and drag force were used with the matrix elements for negative forces, positive forces would be obtained although their magnitudes would be incorrect. The results would indicate, however, that the matrix elements for a positive force should have been used to obtain the correct forces and moments. The automatic digital data reduction program always used the coefficients for positive forces first and then the sign of the calculated forces was checked with the assumption. If either of the forces was found to be negative, the program would automatically recalculate the loads based upon the other set of coefficients.

It is noted from inspection of the balance conversion matrix (Figure 19) that it is not diagonal and that reasonably large interaction conversion constants are present.

At the completion of the balance calibration, values of dummy load resistors that could be applied across the arms of each balance beam bridge were determined for full-scale loads so that electrical calibration checks of the balance system could be easily made during the tests. The dummy load resistors (DLR's) that were established for the 100-percent load condition of each balance beam are as follows:

X_1	88,000 ohms	X_4	36,000 ohms
X_2	78,000 ohms	X_5	64,000 ohms
X_3	36,000 ohms	X_6	40,000 ohms

The calibration of the balance system as an independent unit indicated repeatedly that, through the use of the balance conversion matrix, the forces and moments could be determined within 1 percent of their designed full-scale values. Checks made during calibration of the entire system established that the loads could be measured to within only 1-1/2 percent of the designed full-scale values. Using this

latter percentage as the possible error range, the various forces and moments have the following error bands:

root normal force	(*NFR*)	±20 lbs
root edgewise force	(*EFR*)	±7 lbs
root beamwise moments	(*BMR*)	±165 ft-lbs
root edgewise moments	(*EMR*)	±75 ft-lbs
root pitching moments	(*PMR*)	±15 ft-lbs

Position Transducers Calibration

The azimuth angle transducer was calibrated by setting the blade at prespecified azimuthal positions and recording the voltage output from the transducer. The prespecified azimuthal positions consisted of twenty-four 15-degree increments. The 15-degree increments were marked on the circular rotor-head baseplate. This baseplate rotated with the blade. A fixed indicator, having a scale scribed on it, was mounted so that the indicator scale and baseplate scale were in close proximity and could be read simultaneously. The indicator scale was divided into increments of 0.1 degree. Thus, the prespecified azimuthal positions could be read to within ± 0.1 degree. The results of the calibration are presented in Figure 20. It is believed that, on the basis of the results obtained during the calibration, the azimuth angle could be set to within ± 0.5 degree when the transducer output was read on the digital voltmeter located on the operator's console.

The transducer for the shaft tilt angle, α_s, the instrumented (red) blade pitch angle, and the dummy (white) blade pitch angle were calibrated using an inclinometer capable of measuring to 0.01 degree. The results of these calibrations are shown in Figures 21 through 23. It is believed, on the basis of the calibration, that the shaft tilt angle and blade pitch angles were measured to within ± 0.20 degree if the linearized curves presented in Figures 21 through 23 are used. It is noted that the accuracy of determining each of the respective angles was significantly improved (± 0.10 degree) when the digital voltmeter was used to set given angles for which a specific output voltage was known.

Pressure Gage Calibration

The equipment used during calibration of the pressure gages is shown in Figure 24. A pressure fitting was contoured to the cross section of the blade so that one whole chordwise station could be calibrated at one time. Since a vacuum was applied to the gages, a good seal between the pressure fitting and the blade could be obtained through the use of a fibrous putty. The vacuum gage was capable of indicating 0.01 psi, and 0.005 psi could be easily estimated. All gages were

calibrated at 0.20-psi increments for increasing and decreasing pressures up to a maximum pressure of 4 psi. The results of those calibrations for typical 1-, 2-, 4-, 8-, and 15-psi differential gages are presented in Figures 25 through 29; for the 5- to 20-psi absolute gages, in Figure 30. Table III presents the calibration constants in terms of volts per psi for all the gages mounted on the blade.

It is noted from the results presented in Figures 25 through 30 that the transducer outputs were surprisingly linear throughout the pressure range of interest. It is noted, for example, that the 1-psi differential gage was linear up to three times its designed output, and the 15-psi gage was surprisingly accurate in a pressure range of ± 1 psi. Although it has not been indicated in the figures, the repeatability of each of the gages was remarkably good, with the differences being too small to be plotted. On the basis of the results obtained, it is believed that the pressure gages were sufficiently well calibrated so that the readings for all gages can be expected to have an error of no more than ± 0.2 psi for the pressure range of interest (0 to ± 2.5 psi).

Calibration of Blade-Mounted Strain Gages

The calibration constants for the strain gage sets which measured the beamwise, edgewise, and torsional moments are presented in Figures 31 through 33. These constants were obtained as follows: consider the beamwise gage set calibration constants given in Figure 31 as typical. The beam was loaded at a given station with a beamwise moment. The signal from the gage set which was designated to measure beamwise moments was recorded for each instrumented spanwise station. The signal from each beamwise gage set was recorded as the moment was increased at the given station. A plot of signal output versus moment applied was made for each spanwise station, and the resultant slope (volts/ft-lb) was determined. The point of application of the moment was changed and the process repeated. The slopes obtained at each spanwise station for the various load stations are presented in Figure 31. For purposes of data reduction, the slopes at each station were averaged; the averaged values are presented in Table IV. Coupling between the various moments was neglected.

To determine the moments induced by the blade weight, the blade was supported in a horizontal position. This position was used as the zero moment reference position during pretest calibrations. The moments due to the blade weight were measured with respect to this reference position. The beamwise and edgewise deflections of the beam were also measured and are presented in Figures 34 and 35, respectively. The torsional deflection of the blade due to its weight was not measurable.

During the tunnel tests, however, the zero reference position, for reasons of convenience, was chosen as that of the blade deformed under its own weight. The moment data were then appropriately modified to account for the weight contribution.

Table III

PRESSURE-GAGE CALIBRATION CONSTANTS

GAGE LOCATION		CALIBRATION CONSTANT VOLTS/PSI (ATTENUATION=1)	GAGE LOCATION		CALIBRATION CONSTANT VOLTS/PSI (ATTENUATION=1)
(% SPAN)	(% CHORD)		(% SPAN)	(% CHORD)	
41.1	3.7	0.161	85.2	47.8	0.275
41.1	16.9	0.160	85.2	62.0	0.620
41.1	33.5	0.420	85.2	68.9 UPPER SURFACE	0.060
41.1	62.0	0.983	85.2	68.9 LOWER SURFACE	0.069
41.1	85.9	0.670	85.2	75.4	0.520
55.7	2.1	0.116	85.2	82.0 UPPER SURFACE	0.051
55.7	3.7	0.117	85.2	88.0	0.326
55.7	16.9	0.179	85.2	94.1 UPPER SURFACE	0.055
55.7	22.6	0.149	85.2	94.1 LOWER SURFACE	0.076
55.7	62.0	0.654	85.2	97.0 UPPER SURFACE	0.044
55.7	88.0	0.840	85.2	97.0 LOWER SURFACE	0.053
75.4	2.1	0.121	90.1	2.1	0.163
75.4	9.0	0.148	90.1	9.0	0.123
75.4	62.0	0.525	90.1	16.9	0.113
75.4	88.0	0.740	90.1	22.6	0.165
85.2	2.1	0.106	90.1	62.0	0.334
85.2	3.7	0.124	90.1	88.0	0.435
85.2	9.0	0.125	95.0	2.1	0.154
85.2	12.9	0.111	95.0	9.0	0.160
85.2	16.9	0.118	95.0	16.9	0.075
85.2	22.6	0.120	95.0	88.0	0.530

Table IV
STRAIN-GAGE CONVERSION CONSTANTS

% SPAN	BEAMWISE (volts/ft-lb x 10^3)	EDGEWISE (volts/ft-lb x 10^3)	TORSION (volts/ft-lb x 10^3)
93.0	1.560	0.097	1.296
86.9	1.790	0.182	1.368
80.7	1.340	0.239	1.332
70.8	1.819	0.267	1.296
61.0	1.670	0.280	1.482
51.1	1.760	0.299	1.230
37.3	1.890	0.200	1.440
28.4	1.810	0.197	1.242
16.6	0.640	0.149	0.197

It should be noted at this point that a considerable effort was expended in an attempt to obtain blade load distribution data from a knowledge of the blade deflection data as determined from the strain gages. This effort failed to yield any meaningful data. It is believed that the reasons for the failure were twofold.

The first reason was the mathematical nature of the equations describing the relationship between the loads and moments and deflections. This relationship can be written in matrix form as

$$\{\varepsilon\} = [c]\{\ell\}$$

where

$\{\varepsilon\}$ column matrix of blade deflections

$\{\ell\}$ column matrix of blade loads and moments

$[c]$ square matrix of blade influence coefficients

The matrix $[c]$ can be determined experimentally. Mathematically, it is possible to obtain the inverse of the matrix $[c]$ and, hence, to obtain load information from deflection data (i. e., strain signals). However, practical difficulties arise in obtaining the inverse of the matrix $[c]$ when $[c]$ has off-diagonal elements which are large compared to the main diagonal elements. The matrix $[c]$ is then said to be ill-conditioned, and an accurate inverse is obtainable only under very stringent conditions. For the case in hand, these conditions were not met. A more detailed discussion of this problem is presented in Reference 18.

A second reason for the lack of success of the effort was that, for the stopped-rotor configurations, blade deflections could arise which result in nonlinear relations between the applied loads. Since the entire approach is based upon the theory of linear superposition, it did not succeed. As an example, consider the pitching deflection of the blade root. A contribution to the pitching deflection from the drag load arises when there is a spanwise bending deflection. However, this spanwise deflection is due principally to the blade normal force. Hence, a pitching deflection arises which is proportional to the product of the drag and normal force acting on the blade.

C. WIND TUNNEL TEST PROCEDURES

After the test rotor had been mounted in the wind tunnel, final calibrations of the shaft tilt, blade pitch, and azimuth angle transducers were conducted. Check calibrations were also conducted on all transducers to insure that they were operating correctly and that their calibration constants had not changed.

Since the axis of the force balance at the root of the instrumented blade rotated with the blade during pitch changes, the gravity effect of the blade on the balance had to be determined over the range of blade pitch angles, shaft tilt angles, and azimuth angles at which the tests were to be conducted. A series of "static runs" (no free-stream velocity) were conducted prior to the "wind-on" tests to obtain the balance tares for the expected range of rotor parameters. Over a hundred data points were taken during the "static runs" to provide balance tare values for various combinations of the rotor control angles, α_s, θ_R, ψ.

Prior to each data run (a data run is measured from the time the air is turned on to the time the tunnel is shut down), the instrumented blade was put at zero azimuth angle, and the shaft tilt angle and blade root angle were also placed at zero. All instrumentation channels were balanced, and all transducer signals were then recorded for a standard attenuation on each channel. These signals were considered to be initial zeros. At the end of each data run, the same procedure was carried out to obtain final zeros, except the instrumentation was not rebalanced. Comparison of before-and-after run zeros permitted "instrumentation drift" to be evaluated. It was found to be negligible in all cases.

The tests were conducted by an operator who sat at the control console in the forward portion of the run shack, where he could have a full view of the rotor. Figure 36 is a photograph of the test operator's station. The transit to the right of the test operator's station was used to check for slippage of the friction wheel on the azimuth transducer during a run. This was accomplished by setting the rotor at $\psi = 90$ degrees with the digital readout and then viewing two scribe marks on the rotor head (one on the rotating side and one on the nonrotating side) to see if they were properly aligned. If the offset between the scribe marks indicated that more than approximately 1/4 degree of slippage had occurred, the tunnel was shut down and the transducer reset. This had to be done only once during the tests, when the amount of slippage indicated that the azimuth angle was approximately 0.4 degree in error.

The test operator communicated with the instrumentation and data engineers located in the back of the run shack (Figure 16) through a sound-powered telephone set.

The test procedure used to obtain the data varied because of limits imposed by static loads and instabilities. To obtain the data at the low dynamic pressure, $q \cong 15$ psf, the red blade pitch angle and the shaft tilt angle were held fixed and the azimuth angle was varied. For nominal dynamic pressures of 30 and 45 psf, the azimuth angle was held fixed and the red blade pitch angle and shaft tilt angle were varied to obtain the data at the desired conditions.

The primary limits that were imposed on the conditions at which data could be obtained were dynamic instabilities encountered in the azimuth-angle range of 225 to 300 degrees, and a prespecified maximum beamwise stress of 30,000 psi at the blade critical section. The blade critical station was chosen to be the 28.4-percent span since this was the inboard-most station prior to the increase of blade stiffness at the root. Thus, the largest blade stresses would probably occur here. The maximum spanwise stress was arrived at by taking three-quarters of the allowable stress for the weakest material used in the blade. The moment at the critical station which would cause a stress of 30,000 psi was approximately 5,500 ft-lbs.

The nominal conditions for which data points were obtained at nominal dynamic pressures of 15, 30 and 45 psf are presented in Tables V, VI, and VII, respectively. In all, over 700 data points were obtained during the tests.

D. PRESENTATION AND DISCUSSION OF RESULTS

The results that will be presented and discussed in this report are primarily those obtained from the balance measurements. All the basic data that were obtained during the test program will be held on file at USAAVLABS. Figure 37 presents a typical printout of the various data items that were obtained at each test condition. As noted in Figure 37, the test parameters are listed in the upper right-hand corner of the data page. These parameters consist of the dynamic pressure (lbs/ft^2), blade azimuth position (degrees), shaft tilt angle (degrees), blade root pitch angle (degrees), and the run and point numbers which define the sequence of the actual test points. Next is presented the matrix of pressures, differential and absolute, in psi. Each column of the matrix represents the chordwise pressure distribution at a given spanwise station. Most of the pressures presented are differential; however, those denoted by the symbols *TS* and *LS* are absolute pressures. The *TS* symbol indicates the pressure measured on the upper surface of the blade at the given station, and the *LS* denotes the lower surface pressure. Positive readings denote pressures which correspond to positive lift; therefore, pressures below atmospheric are positive for the upper surface while pressures above atmospheric are positive on the lower surface.

Considerable care should be exercised in interpreting the pressure distributions that were obtained, particularly for azimuth positions ranging from 180 degrees to 330 degrees. This caution is given as the trailing edge of the blade was blunted because of the significant number of gage instrumentation wires that were bonded along the span near the trailing edge. The effect of the blunted trailing edge might be significant when the flow is such as to make the trailing edge a leading edge. Furthermore, upon inspection of the data, it was found

Table V

TABULATION OF NOMINAL TEST CONDITIONS
(DYNAMIC PRESSURE, q = 15 psf)
X...INDICATES A TEST POINT

AZIMUTHAL POSITION (ψ) deg	SHAFT ANGLE (α_s) deg	BLADE ROOT ANGLE, θ, deg					
		-3	-1	+2	+7	+12	+17
90	+10						X
	+5						X
	0		X	X	X	X	X
	-5	X					
	-10	X					
120	+10						X
	+5						X
	0		X	X	X	X	X
	-5	X					
	-10	X					
150	+10						X
	+5						X
	0		X	X	X	X	X
	-5	X					
	-10	X					
180	+10						X
	+5						X
	0		X	X	X	X	X
	-5	X					
	-10	X					
210	+10						X
	+5						X
	0		X	X	X	X	X
	-5	X					
	-10	X					
240	+10						X
	+5						X
	0		X	X	X	X	X
	-5	X					
	-10	X					
270	+10						X
	+5						X
	0		X	X	X	X	X
	-5	X					
	-10	X					

Table VI

TABULATION OF NOMINAL TEST CONDITIONS

(DYNAMIC PRESSURE, q = 30 psf)

X...INDICATES A TEST POINT

AZIMUTHAL POSITION (ψ) deg	SHAFT ANGLE (α_s) deg	BLADE ROOT ANGLE, θ, deg												
		-8	-5	-2	+1	+4	+7	+10	+12	+13	+16	+17	+19	+22
30	+5				X	X	X	X		X	X	X	X	X
	+2½				X	X	X	X		X				
	0				X	X	X	X		X				
	-2½				X	X	X	X		X				
	-5	X	X	X	X	X	X	X		X				
60	+5				X	X	X	X		X	X	X	X	X
	+2½				X	X	X	X		X				
	0				X	X	X	X	X	X		X		
	-2½				X	X	X	X		X				
	-5	X	X	X	X	X	X	X		X				
90	+5				X	X	X	X	X	X	X	X		
	+2½				X	X	X	X		X				
	0				X	X	X	X	X	X		X		
	-2½					X	X	X		X				
	-5					X	X	X		X				
105	+5				X	X	X	X		X				
	+2½				X	X	X	X		X				
	0					X	X	X		X				
	-2½					X	X	X		X				
	-5						X	X		X				
120	+5				X	X	X	X		X	X	X		
	+2½				X	X	X	X		X				
	0					X	X	X	X	X		X		
	-2½					X	X	X		X				
	-5						X	X		X				
135	+5				X	X	X	X		X				
	+2½				X	X	X	X		X				
	0				X	X	X	X		X				
	-2½					X	X	X		X				
	-5						X	X		X				
150	+10						X							
	+7½						X							
	+5				X	X	X	X		X	X	X	X	X
	+2½				X	X	X	X		X				
	0		X	X	X	X	X	X	X	X		X		
	-2½				X	X	X	X		X				
	-5					X	X	X		X				
	-7½						X							

Table VI - Continued

(DYNAMIC PRESSURE, q = 30 psf)
X...INDICATES A TEST POINT

AZIMUTHAL POSITION (ψ) deg	SHAFT ANGLE (α_s) deg	BLADE ROOT ANGLE, θ, deg												
		-8	-5	-2	+1	+4	+7	+10	+12	+13	+16	+17	+19	+22
165	+5				X	X	X	X		X				
	+2½				X	X	X	X		X				
	0				X	X	X	X		X				
	-2½				X	X	X	X		X				
	-5				X	X	X	X		X				
	-7½			X	X	X	X							
180	+14						X							
	+12						X							
	+10						X							
	+7½						X							
	+5				X	X	X	X		X	X	X	X	
	+2½				X	X	X	X		X				
	0				X	X	X	X	X	X		X		
	-2½				X	X	X	X		X				
	-5				X	X	X	X		X				
	-7½						X							
	-10						X							
	-12						X							
	-14						X							
210	+5				X	X	X	X		X	X	X		
	+2½				X	X	X	X		X	X		X	
	0				X	X	X	X	X	X	X	X	X	
	-2½				X	X	X	X		X				
	-5				X	X	X	X		X				
225	+5			X		X	X	X		X	X		X	X
	+2½		X		X	X	X	X		X	X		X	
	0				X	X	X	X		X	X		X	
	-2½				X	X	X	X		X				
	-5				X	X	X	X			X			
240	+5						X	X		X	X	X	X	X
	+2½					X	X	X		X	X		X	
	0				X	X	X	X	X	X	X			
	-2½		X		X	X	X	X		X				
	-5				X	X	X	X						
255	+5					X	X	X		X			X	X
	+2½				X	X	X	X		X			X	
	0				X	X	X	X		X	X	X		
	-2½				X	X	X	X		X				
	-5				X	X	X	X		X				

Table VI – Continued

(DYNAMIC PRESSURE, q = 30 psf)
X...INDICATES A TEST POINT

AZIMUTHAL POSITION (ψ) deg	SHAFT ANGLE (α_s) deg	BLADE ROOT ANGLE, θ, deg												
		-8	-5	-2	+1	+4	+7	+10	+12	+13	+16	+17	+19	+22
270	+5				X	X	X	X		X				
	+2½				X	X	X	X		X	X		X	
	0				X	X	X	X	X	X	X			
	-2½				X	X	X	X		X	X		X	
	-5		X	X	X	X	X	X		X				
285	+5				X	X	X	X		X			X	
	+2½				X	X	X	X		X			X	
	0	X	X	X	X	X	X	X		X	X			
	-2½				X	X	X	X		X				
	-5				X	X	X	X		X			X	
300	+5				X	X	X	X		X				
	+2½				X	X	X	X		X				
	0				X	X	X	X		X				
	-2½				X	X	X	X		X				
	-5				X	X	X	X						
330	+5	X			X	X	X	X		X				
	+2½				X	X	X	X		X				
	0				X	X	X	X		X				
	-2½				X	X	X	X		X				
	-5				X	X	X	X		X				

Table VII

TABULATION OF NOMINAL TEST CONDITIONS

(DYNAMIC PRESSURE, q = 45 psf)

X...INDICATES A TEST POINT

AZIMUTHAL POSITION (ψ) deg	SHAFT ANGLE (α_s) deg	BLADE ROOT ANGLE, θ, deg		
		+4	+7	+10
30	$2\frac{1}{2}$	X	X	X
	0	X	X	X
60	$2\frac{1}{2}$	X	X	X
	0	X	X	X
90	$2\frac{1}{2}$	X	X	X
	0	X	X	X
105	$2\frac{1}{2}$	X	X	X
	0	X	X	X
120	$2\frac{1}{2}$	X	X	X
	0	X	X	X
135	$2\frac{1}{2}$		X	
	0			X
150	$2\frac{1}{2}$	X	X	X
	0	X	X	X
165	$2\frac{1}{2}$	X	X	X
	0	X	X	X
180	$2\frac{1}{2}$	X	X	X
	0	X	X	X
210	$2\frac{1}{2}$	X	X	X
	0	X	X	X
225	$2\frac{1}{2}$	X	X	X
	0	X	X	X
240	$2\frac{1}{2}$	X	X	X
	0	X	X	X
255	$2\frac{1}{2}$	X	X	
	0	X	X	X
270	$2\frac{1}{2}$	X	X	X
	0	X	X	X
300	$2\frac{1}{2}$	X	X	X
	0	X	X	X

that very low pressure levels were indicated in certain azimuthal positions. Consequently, great reliance was placed on the integrated loads measured by the balance system. Analyses of the pressure data were utilized primarily to assist in the interpretation of the other measurements wherever possible.

The spanwise distributions of the blade flatwise, edgewise, and torsional structural moments are presented immediately below the pressure matrix,as shown in Figure 37. As previously noted, these moments do not include the gravity moments due to blade weight ; thus, they are the true aerodynamic moments. Finally, the balance data are presented. The balance was fixed to the blade root, and the data presented here are in the balance frame of reference.

It was necessary to correct the balance readings for the tares due to blade weight. Consideration of these tares resulted in a modification of the balance error limits from those presented on page 11 (note particularly the root edgewise force and root edgewise moment). The balance data presented in the tabular listings and in the plots to be presented herein, therefore, have the following error limits:

root normal force	(*NFR*)	± 25 lbs
root edgewise force	(*EFR*)	± 15 lbs
root beamwise moments	(*BMR*)	± 175 ft-lbs
root edgewise moments	(*EMR*)	± 125 ft-lbs
root pitching moments	(*PMR*)	± 15 ft-lbs

Data obtained at azimuth angles of 90, 270,and 180 degrees will be discussed first. For azimuth angles of 90 and 266 degrees, the various forces and moments as measured by the balance system have been combined to yield the lift, drag, rolling moment, drag moment, and pitching moment. For the azimuth angle of 180 degrees, only the balance measurements are presented.

Figure 38 presents the variation of lift with blade root geometric angle of attack for the blade at azimuth angles of 90 and 266 degrees. The sign convention of the composite angle of attack which is made up of the blade root pitch angle, θ_R , and the shaft angle, α_s , for both azimuth positions is indicated on the respective plots. It should be remembered that this blade had 11 degrees of linear twist (washout) from root to tip. It is noted that the data presented on these plots were not obtained from a single run but were obtained from runs conducted throughout the entire series of wind tunnel tests for various combinations of shaft angle and blade pitch angle. It was gratifying to observe that all the data seemed to plot on fairly smooth curves with only the anticipated amount of scatter present.

In analyzing the results as presented in the data plotted in Figure 38, it is noted that the apparent integrated nonlinear stall effects, as measured by the balance, are much more pronounced at 90 degrees than at 266 degrees, in that, at 90 degrees, the lift drop-off is more severe. It is interesting also to note that apparent stall occurs at a lower root geometric angle of attack when the trailing edge is into the airstream than when the normal leading edge is in this orientation. This result is what might be expected based upon sectional data presented in Reference 8. The nonlinear stall effects, as indicated by the data presented in Figure 38 for both azimuth positions, are more like those of a "soft stall", in that a sharp break in the lift curve is not obtained. It is believed that this "soft stall" characteristic is due to the fact that the lift is the air load integrated over the whole span; thus, the blade is effectively slowly stalling with increasing angle of attack.

It is noted that, at 0 degrees geometric angle of attack, the blade is developing approximately twice the lift magnitude at an azimuth position of 266 degrees than it is at 90 degrees. It is believed that this difference is due, in part, to the blade twist resulting from the aerodynamic pitching moment. At 90 degrees azimuth, the aerodynamic pitching moment about the quarter chord at 0 degrees geometric angle of attack is very small; while at 266 degrees, the aerodynamic pitching moment is significant and in a direction so as to increase the effective blade angle of attack. Calculations based on the measured torsional strains indicated that the blade tip was twisted approximately 2 degrees, which would increase the total blade lift at ψ = 266 degrees by approximately 100 pounds. This increment in lift due to twist reduces the differential lift magnitude at 0 degrees angle of attack to 150 pounds between the 90- and 266-degree azimuth positions.

It was suspected that this remaining difference in lift might be due to an unknown tunnel flow misalignment. This suspicion was supported by the fact that the root geometric angles of zero lift differ by 3 degrees for the 90- and 266-degree azimuth positions. If the blade did not have any tip effects and was rigid, the root angle for zero lift for both azimuth positions would be one-half of the blade twist or approximately 5-1/2 degrees. This angle of zero lift is 1-1/2 degrees higher for the 90-degree orientation and 1-1/2 degrees less than that measured at an azimuth angle of 266 degrees. While flow angularity could explain the noted differences, a flow angularity of this magnitude could not be justified on the basis of flow calibrations conducted previously by NASA-Ames.

The total aerodynamic rolling moments measured by the balance at ψ = 90 and 266 degrees are shown in Figure 39. The interesting point to be made concerning these data is that the angle for zero rolling moment is almost the same as that for zero lift at ψ = 266 degrees, and only 1 degree different from that for zero lift at ψ = 90 degrees. The

difference in the angle of zero lift and zero rolling moment would be expected to be approximately 2 degrees for a rigid blade having a linear twist distribution of 11 degrees. It is suspected that the disagreements might be attributed to three-dimensional elastic effects.

The pitching moments about the quarter chord versus root geometric angle of attack are presented for azimuth angles of 90 and 266 degrees in Figure 40. It is noted that the pitching moments at ψ = 266 degrees are much larger than at ψ = 90 degrees. This is as expected because of the significant difference in the distance between the center of pressure and the quarter chord at ψ = 90 and 266 degrees. The difference in the variation of the pitching moment with root geometric angle of attack is also significant between ψ = 90 and 266 degrees. Sectional data presented in Reference 8, however, tend to confirm the differences in the characteristics that were measured. The large decrease in the pitching moment above 13 degrees at ψ = 90 degrees is possibly due to stall, which tends to move the integrated effective center of pressure aft of the quarter chord as stall progresses along the span of the blade. At ψ = 266 degrees, the variation of the pitching moment with angle of attack would be expected to be more linear. In this case, the chordwise shift of the center of pressure with angle of attack is a smaller percentage of the distance between the center of pressure and the quarter chord than it is at ψ = 90 degrees. Thus, a significant nonlinearity in the pitching moment about the quarter chord would not occur until a much larger portion of the blade has become stalled. In addition, it is noted that the pitching moment at ψ = 266 degrees would not change sign as it does at ψ = 90 degrees, as the blade stalls with increasing angle of attack since the center of pressure will move forward only to approximately the 50-percent chord station.

The variations of the drag force with blade root angle are shown in Figure 41 for ψ = 90 and 266 degrees. It is interesting to note that the root geometric angle of attack for minimum drag is approximately the same for both azimuth positions and that both curves are approximately symmetrical about the angle of minimum drag. It is somewhat surprising, based on sectional data presented in Reference 8, that the drag force at ψ = 266 degrees was not significantly larger than that at 90 degrees. On the basis of sectional data, it would be expected that the drag force would be at least twice as large at ψ = 266 degrees as it is at ψ = 90 degrees over the range of angle of attack for which results were obtained. A rational explanation for the approximate equivalence of the drag forces at the two azimuth positions could not be determined.

The variation of the drag moment with root geometric angle of attack is presented in Figure 42. It can be seen that the point of minimum drag moment is roughly the same for both azimuth positions, approximately 6 to 7 degrees, which is about 3 degrees less than the angle for minimum drag. The drag moment curves are again approximately symmetrical about the angle for minimum moment at both ψ = 266

and ψ = 90 degrees. The rate of moment increase with blade angle from the minimum is significantly larger for ψ = 266 degrees than it is for ψ = 90 degrees.

Figure 43 presents the variation of the ratio of lift to drag with root geometric angle of attack. It is noted that the maximum values of L/D occur at approximately 12 degrees and that the maximum value at ψ = 266 degrees is much less than it is at ψ = 90 degrees. The ratio of the maximum values at 90 and 266 degrees is approximately 3.5:1, which compares to a value of approximately 3.6:1 based on sectional data. The fact that the present measurement of this ratio is approximately the same as the value based on sectional data is coincidental. As was noted previously, the individual measured blade forces did not exhibit the same variations with angle of attack as the forces based on corresponding two-dimensional sectional data.

Figure 44 presents the variation of the root normal force and root beamwise moment with shaft angle for an azimuth angle of approximately 180 degrees. In this azimuthal orientation, the blade becomes a low-aspect-ratio wing with respect to the free-stream velocity, and the shaft angle becomes a measure of the geometric angle of attack for the wing. As a result, one might expect that the variation of the blade aerodynamic characteristics with shaft angle would be similar to that of a low-aspect-ratio wing. This appears to be the case, as evidenced by Figure 44. It is noted that the root normal force is small over the entire range of geometric angle of attack. Further, the variation of the normal force with geometric angle of attack is nonlinear, as might be expected for a low-aspect-ratio wing. The corresponding moment variation is also nonlinear. The magnitudes of the moments reflect the fact that the moments are taken about the blade root and the effective moment arm is large. The moment plot indicates that blade divergence might be reached at a smaller negative shaft angle (i.e., geometric angle of attack) than for positive shaft angles. It is believed that this is due to the effects of the blade spanwise flexibility. At zero shaft angle and wind off, the blade tip is bent down approximately 1 foot due to the blade weight. This spanwise distribution of blade deflections causes the geometric angle of attack of the blade with respect to the free-stream velocity to be different from the shaft angle. If the blade were rigid, the blade geometric angle of attack and the shaft angle would be identical. Thus, as the shaft angle is increased in the negative direction, the blade flexibility causes a more rapid increase in angle of attack due to the additive contribution of the blade weight and aerodynamic loading than indicated by the shaft angle. A similar effect occurs as the shaft angle is increased in the positive direction. However, at some positive shaft angle, the aerodynamic blade load and moment distribution is such as to just balance the weight load and moment and effectively remove the contribution due to blade deflection due to weight. Above this value of shaft angle, the blade bending due to aerodynamic loading, now in a positive direction, again begins to contribute in an additive manner to the angle of attack.

Thus, if divergence were to occur, it might be expected to occur at smaller negative shaft angle magnitudes than for positive shaft angles.

Note, also, that the effects of blade flexibility tend to emphasize the nonlinear behavior of the blade aerodynamics with geometric angle of attack over and above that which might be expected if the blade were rigid.

Figure 45 presents a plot of the spanwise moment distribution of the blade for various shaft angles. Note that the spanwise distributions of moments for negative shaft angles are very similar, while those for positive shaft angles differ in shape from one another. The shapes of the moment distributions for positive and negative shaft angles are also different. Not until $\alpha_s \approx 14$ degrees does the shape obtained for positive shaft angle begin to look like the shapes obtained for negative shaft angles. It is believed that this behavior is also due to the effects of blade spanwise flexibility. It is proposed that the change in shape of the moment distribution curves in the range $-2 < \alpha_s < 7$ degrees is attributable to the reduced effect of blade spanwise deformations which are minimized in this range due to the balancing of the aerodynamic and gravity loads.

The fact that increased dynamic pressure increases the aerodynamic loading and, hence, the blade deflections would lead to the expectation that increasing dynamic pressure would increase the nonlinear behavior of the blade aerodynamics. This seems to be substantiated in Figure 44 by the behavior of the normal force and moment at q = 45 psf as compared with their behavior at q = 28 psf.

Figure 46 presents the variations of the root edgewise force and moment and the root pitching moment with shaft angle. It is noted that all of these quantities are not much larger than the possible measurement errors ; hence, there is considerable scatter in the data.

Figures 47 through 51 present the azimuthal variations of the root normal force, root beamwise moment, root edgewise force, root edgewise moment, and root pitching moments, respectively, as measured by the balance system for three different shaft angles and for a number of different blade pitch angles. Steady values of the various forces and moments could not be obtained for certain combinations of azimuth and blade pitch angles because of either a dynamic instability or load limits. These areas have been noted on all the figures. The limit load was based upon a 30,000-psi beamwise stress limit that was arbitrarily imposed at the critical blade section. Because of the beamwise stress developed by the gravity load, larger positive values of aerodynamic beamwise moments could be obtained than the approximately 6,000 ft-lb negative aerodynamic beamwise moment limit.

No data are presented for azimuth angles of 0 ± 30 degrees because of interference effects introduced by the wake of the rotor head.

The variation of the root normal force with azimuth angle for zero shaft angle, shown in Figure 47, is what might be expected, in that, as the blade angle is increased, the normal force on the advancing side gets larger in the positive direction and larger values in the negative direction are obtained on the retreating side. It can also be seen that, as the root blade angle is decreased, negative values of the normal force can be obtained on the advancing side and positive ones on the retreating side. Regardless of the blade angle, the normal force is approximately zero at the 180-degree azimuth position. The change in the azimuthal variation of the normal force that is obtained with the blade pitch angle suggests the possibility of developing a constant normal force around the azimuth if the proper blade pitch-control schedule can be provided. Since, at zero shaft angle, the normal force is zero for any blade pitch angle at ψ = 180 degrees, the only possible constant normal force is zero. Figure 48 presents the approximate blade pitch-control schedule that would be required at zero shaft angle to obtain a zero normal force around the azimuth. This curve was constructed by cross plotting the data presented in Figure 47 to determine the blade angles which would result in a zero normal force at various azimuth positions. While the variation presented in Figure 48 must be considered as approximate, these results demonstrate that the pitch-control schedule required to obtain zero normal force at the blade root around the azimuth would be rather complicated.

The results presented in Figure 47 for other shaft angles show that changes in the shaft angle have a large effect on the azimuthal variation of the normal force. The exception to this is at ψ = 180 degrees where the normal force has only a small variation with shaft angle and the effect of blade pitch angle is, as previously noted, nonexistent. For a positive shaft angle of 5.18 degrees, it appears from the results presented that, in the range of azimuth angle $30 < \psi < 180$ degrees, the blade may have been stalled over much of its span as the blade angle was increased from 10.19 to 13.21 degrees. The normal force does not increase significantly for this increase in blade root pitch angle.

The variations of the root beamwise moment with azimuth position for three shaft angles and several blade pitch angles are presented in Figure 49. The variation of the root beamwise moments with azimuth angle is as what might be expected on the basis of the variation of the root normal force for the same test conditions. It is noted that, at ψ = 180 degrees, the change in the root beamwise moment with shaft angle is larger for negative shaft angles than it is for positive shaft angles, although the change in the normal force was about the same. This could be the effect of blade beamwise bending, which probably shifts the load outboard. It is apparent, when the variations of the root normal force and root beamwise moments with azimuth angle are compared, that the pitch control schedule required to make the beamwise moment constant around the azimuth would be different from that required to accomplish the same objective with the normal force.

The variations of the root edgewise force with azimuth angle are presented in Figure 50 for three different shaft angles and for a number of different blade root pitch angles. In viewing these curves, it must be remembered that this force is oriented parallel to the blade root chord. Since the blade root chord is at an angle of attack with respect to the airstream, the root edgewise force is not the same as the drag force which is in the windstream axis system. It is interesting to note that, generally, the root edgewise force is larger on the advancing side, $30 < \psi < 180$ degrees, than it is on the retreating side, $180 < \psi < 330$ degrees, for the range of blade angles tested, and that the minimum variation in the force with azimuth angle was obtained for a shaft angle of -4.77 degrees. The edgewise force is not generally in the direction one would expect, in that, with the leading edge facing the airstream, the edgewise force is such as to put the leading edge in compression. The strain-gage data verify this result, as the edgewise strain indicates leading-edge compression along the entire blade span for positive pitch angles at $\psi = 120$ degrees. It is noted, however, that, when the root normal force and edgewise force are resolved to obtain lift and drag, positive values of drag (with respect to the airstream reference system) are obtained on the advancing side of the rotor disc.

The variations of the root edgewise moments produced by the root edgewise forces with azimuth angle are shown in Figure 51. It is noted that, as with the root edgewise force, the variation of the root edgewise moment is generally larger on the advancing side of the disc than it is on the retreating side and that the minimum variation was again obtained for all blade angles at a shaft angle of -4.77 degrees.

At a shaft angle of 0.01 degree, the root edgewise moment for for a root pitch angle of + 1.11 degrees abruptly reverses in direction between $\psi = 100$ and 130 degrees. No explanation for this anomalous behavior was found.

The variation of the root pitching moment about the blade quarter chord with azimuth (Figure 52) is what one would expect -- small over the advancing quadrant of the disc and large over the retreating quadrant of the disc, where the moment arm is relatively large because of the shift in the center of pressure from the quarter-chord to the three-quarter-chord position. It is apparent from the data presented that relatively high control loads can be expected over the retreating quadrants of the disc as a rotor system is being slowed to a stop during the conversion cycle from a helicopter to a fixed-wing aircraft.

While other data of the type obtained during the present tests are not generally available, some data obtained for a three-bladed folding rotor system in the nonrotating mode are available for comparison (Reference 9). The blades that were tested had a diameter of 33 feet, a 14-inch chord, and -9.43 degrees of linear blade twist, and were cantilevered at the root. That rotor system had 2-1/4 degrees of coning, whereas the present rotor system had none. Except for the coning of the rotor system, the

two rotor blades had similar geometric characteristics. The relative stiffness of the blade reported in Reference 9, however, was higher than that for which data have been presented herein.

Figure 53 compares the azimuthal variation of the root beamwise moment as measured by the balance system during the present tests with that obtained by means of strain gages at the root of the blade that was reported in Reference 9. It is noted that the azimuthal variations of the moments are very similar. It is somewhat surprising, however, that larger beamwise bending moments were obtained with the smaller diameter, smaller chord blade of Reference 9 than with the blade used to obtain the data reported herein. While the coning angle would be expected to have this effect, such a large change in the moment for only 2-1/2 degrees of coning would not be expected.

As previously noted in Figures 47 through 52, data could not be obtained for various combinations of blade pitch angles and shaft tilt angles in the azimuth angle range $225 < \psi < 300$ degrees because of dynamic instabilities.

Figure 54 presents basic stability boundaries that were determined from the data obtained during the tests at various shaft angles. The data presented, unless otherwise noted, were obtained at a dynamic pressure of 28.95 psf, which corresponds to a Reynolds number of approximately 10^6 per foot. As indicated in Figure 54, the stable region was between the two boundaries, and the unstable regions were above the upper boundaries and below the lower ones.

At azimuth angles of less than 220 degrees, instability boundaries were not obtained for values of the independent parameters within reasonable bounds. At ψ = 224 degrees, blade stress limits were reached before the lower instability boundaries could be determined for shaft angles $\alpha_s \leq 2.5$ degrees. When the instability was encountered, a low-frequency blade beam-bending oscillation could be seen to start and increase in amplitude. As the amplitude of the low-frequency oscillation built up, a much higher frequency blade beam-bending oscillation would also become visible. While the oscillatory characteristics were approximately the same on both sets of boundaries, the low-frequency bending amplitudes would become larger when the blade was at negative angles of attack (lower set of boundaries) than when the blade was at positive angles of attack (upper set of boundaries). For example, the low-frequency oscillatory amplitudes associated with the lower boundaries would sometimes be allowed to reach + 3 to 4 feet by visual estimation before the blade angle was changed to stop the oscillatory motion, while $\pm$ 2 feet was about the maximum for the upper boundary.

The solid points shown in Figure 54 denote data points that were obtained for q = 43.7 psf, and the arrow that is associated with each point is the direction in which the blade angle was being changed when the instability was encountered. The symbol shape indicates

the q = 28.95 psf curve with which each data point is associated. The point at ψ = 224 degrees and q = 43.7 psf was obtained at a shaft angle which was different from any of the q = 28.95 psf data. From the results that are plotted, however, it can be seen that there is a reasonably large effect of q, particularly at ψ = 224 degrees.

Analysis of the oscillograph records showed that the higher-frequency oscillations involved chordwise and torsional motions at a frequency approximately equal to the first cantilever torsion mode of the blade (Table VIII), and the low-frequency oscillations were at the first-coupled flapwise bending mode of the blade (Table IX).

The results shown in Figure 54 indicate that shaft tilt angle, azimuth angle, and blade pitch angle were all independent parameters. While the shaft tilt angle is a significant parameter, it is noted that its effect is approximately independent of the azimuth angle. In an attempt to determine if, in fact, the shaft angle and blade pitch angles were independent parameters as indicated in Figure 54, the total angle of the blade root with respect to the airstream direction was computed as a function of azimuth. The results of combining these angles are shown in Figure 55. As can be seen, all the data points for each stability boundary at a given azimuth fall within a band of approximately ± 1 degree. Since all the boundaries for different shaft angles become essentially a single boundary, the shaft angle and blade root pitch angle are not independent parameters, and the primary parameter of the instability at a given azimuth location is just the root geometric angle of attack with respect to the airstream. It is felt that the scatter at each of the azimuth locations at which data were obtained could be reduced somewhat if the small amounts of the steady elastic torsional deflections of the blade were taken into account. This has not been done, as it is believed that such a small correction would not change the basic conclusion that was reached from the results presented in Figure 55.

While the combination of the shaft and blade pitch angles into an equivalent blade root angle relative to the airstream indicated that these two angles were not independent parameters, the plot of the data indicated that the composite blade angle at which the instability occurred was still significantly dependent upon the azimuth angle. It is believed that this apparent dependence upon azimuth angle is associated with the bending deflections experienced by the blade in the vicinity of the stability boundaries. Unfortunately, no information is currently available which defines the effect on aeroelastic stability boundaries of lifting surfaces when large loads or deformations are present. However, an intuitive argument (similar to the one presented on page 26) for the case in hand would imply that, if large blade deflections existed, they contributed to the effective angle of attack of the blade. Further, since the blade loadings and, hence, the blade deflections are strong functions of the azimuth angle, it might be expected that the instability boundaries would also exhibit a similar dependence.

Table VIII
UNCOUPLED BLADE CANTILEVER FREQUENCIES

MODE	FREQUENCY cps	MODE	FREQUENCY cps
1st BEAM BENDING	1.18	5th BEAM BENDING	72.03
2nd BEAM BENDING	8.03	1st TORSION	26.00
3rd BEAM BENDING	22.46	2nd TORSION	69.27
4th BEAM BENDING	43.17	3rd TORSION	113.56

Table IX
COUPLED BLADE CANTILEVER BENDING FREQUENCIES

MODE	FREQUENCY cps	GENERALIZED COORDINATES & CHARACTERISTIC SHAPE			
		BEAM BENDING	SHAPE	CHORD BENDING	SHAPE
1st COUPLED BENDING	1.23	1.00	1st CANTILEVER	-0.15	1st CANTILEVER
2nd COUPLED BENDING	7.08	1.00	2nd CANTILEVER	+1.60	1st CANTILEVER
3rd COUPLED BENDING	8.76	1.00	2nd CANTILEVER	-0.62	1st CANTILEVER
4th COUPLED BENDING	23.22	1.00	3rd CANTILEVER	+0.58	2nd CANTILEVER
5th COUPLED BENDING	44.42	1.00	4th CANTILEVER	-0.18	2nd CANTILEVER
6th COUPLED BENDING	47.24	1.00	4th CANTILEVER	+5.10	2nd CANTILEVER
7th COUPLED BENDING	72.44	1.00	5th CANTILEVER	-0.04	3rd CANTILEVER

In order to illustrate the sensitivity of the boundary to blade pitch angle, Figure 58 presents the oscillatory strain data for the blade at a pitch angle 2 degrees less than that for which the results were presented in Figure 57. As can be seen from the traces presented in Figure 57, the torsional oscillations are fairly persistent while the chordwise-bending traces do not show much indication of oscillations at the torsional frequency. It is also noted that there is not much low-frequency beam bending for these conditions. A prominent characteristic of both of the instability boundaries was that high-frequency oscillatory motions did not become apparent visually until after the low-frequency beamwise-bending oscillations became fairly large. This was a very beneficial feature during the tests, as the stability boundaries were determined by visual observation using the beamwise-bending oscillations as an indicator.

The characteristic frequency of the instabilities was nearly equal to the uncoupled torsional frequency of the blade. Also, the local geometric angles of attack of the blade sections were large. These factors led to a suspicion that the instabilities were associated with stall flutter. Evidence that supports this contention is presented below.

Figure 56 presents an oscillograph record showing the beamwise, chordwise, and torsion strain signals at a noted instability condition. Although the traces are somewhat weak because of the reproduction, the following characteristic features can be determined from the strain traces:

1. The torsional oscillations are approximately at the uncoupled torsion frequency of the blade (Table VIII).

2. The chordwise-bending oscillations are at the uncoupled torsional frequency.

3. Large beamwise oscillatory bending occurs at the first-coupled bending mode frequency of the blade.

4. There is almost no high-frequency response at the uncoupled torsional frequency in the beamwise strain signals.

5. The high-frequency torsional and chordwise oscillations are modulated at the first-coupled flapwise-bending frequency (Table IX).

Not all of these features were distinctive in all of the oscillograph records taken at the stability boundary points. However, the particular records discussed herein are representative of those in which these characteristics prevailed.

The strain signals presented in Figure 56 are for a point on the upper stability boundary. For this point, note that, in addition to the above features, the modulated amplitudes of chordwise bending and torsion reached maximums just after the maximum upswing of the beamwise-bending signal occurred, and the chordwise-bending oscillations are in phase with the torsional oscillations.

Figure 57 presents the oscillatory strain signals for a point on the lower instability boundary as plotted in Figures 54 and 55. It is noted that the same basic characteristics as listed for the oscillatory strain traces shown in Figure 56 are present, except that the chordwise-bending signals are out of phase with the torsion, and the peak amplitude of the modulated oscillation occurs just after the maximum downswing of the low-frequency beam bending.

To relate the motions of the blade to the signals presented in Figures 56 and 57, it is noted that the positive directions of beam bending, chord bending, and torsion are up on the oscillograph record. Positive beam bending creates compression on the top surface, positive chord bending creates compression at the geometric trailing edge of the blade, and positive torsion twists the blade in a nose-up direction.

Thus, if Figure 56 is considered, it appears that the blade beamwise-bending oscillations are such as to contribute a plunging velocity, which increases the absolute magnitude of the local angle of attack (remember that the free-stream direction is from the trailing edge to the leading edge) while the blade is moving up, and decreases the local angle of attack as it moves down. Thus, if the blade were close to the stall range due only to the steady angle of attack, the beamwise-bending oscillations would carry the blade into the stall range during part of the cycle and then out again during the remainder of the cycle. Thus, the bending oscillations could precipitate the stall which would now take on dynamic stall characteristics rather than static stall characteristics, and it might be expected that the torsional oscillations would grow and decay in phase (nearly) with the beamwise-bending oscillation frequency.

On the lower boundary where the geometric angles of attack are in the opposite direction, it would be expected that the maximum amplitude of the torsional oscillations would occur just after the maximum downward oscillation of the beamwise bending. This appears to be substantiated in Figure 57.

Other experiments precisely like those reported herein have not been conducted previously. However, there have been a number of investigations conducted to determine regions of negative pitch damping associated with airfoils oscillating about the stall angle of attack. These can be referred to, at least in a qualitative manner, to determine if, for the conditions of the present tests, one might expect a stall-associated instability. It should be noted, however, that for the present tests, the airfoil trailing edge was into the airstream, and the aerodynamic characteristics of the airfoil would be expected to be somewhat different from those for an airfoil having a normal orientation with respect to the airstream. It is believed that the effect of the "sharp leading edge" would be a difference in the static aerodynamic characteristics around stall, and the difference in the dynamic characteristics of stall would be primarily due to the effect of having the pitch axis at the three-quarter chord. Halfman (Reference 10) showed that the primary effect of leading-edge sharpness is a reduction in the static stall angle. Ham (Reference 11) indicates that the primary effect of the aft pitch axis is to reduce the dynamic stall angle. For the reduced frequency of 0.70 at which the instabilities were obtained in the present study, the data that Rainey presented in Reference 12 indicates that negative aerodynamic damping can be obtained for the blade angles at which the present instabilities were encountered. This fact is believed to further substantiate the thesis that the present instabilities could have been stall flutter.

E. DEVELOPMENT OF A LINEARIZED AERODYNAMIC PREDICTION TECHNIQUE

A technique of predicting the aerodynamic characteristics of a rotor blade at arbitrary azimuthal position has been developed using conventional lifting surface theory tailored for this specific application. The detailed development of the theoretical prediction technique and the method for solving the resulting equations are presented in the Appendix. The wing was represented by a distribution of bound vorticity and the wake by trailing vorticity, whose strength distribution is related to the bound vorticity by the Helmholtz laws. Application of the Biot-Savart law to calculate the velocity field associated with a distribution of vorticity results in the following integral equation relating the local wing loading and the local wing slope (i. e., the angle between the local tangent to the mean camber line and the wind reference in the plane of the wind vector).

$$\alpha(x,y) = -\frac{1}{8\pi}\iint_S \frac{\mathcal{L}(x_o,y_o)}{(y-y_o)^2}\left\{1+\frac{(x-x_o)}{[(x-x_o)^2+(y-y_o)^2]^{1/2}}\right\}dx_o\,dy_o \qquad (1)$$

where $\alpha(x,y)$ is the local wing slope and $\mathcal{L}(x_o,y_o)$ is the local wing loading (difference between upper and lower surface pressures). Here the Kutta-Joukowski relation relating loading to the bound vorticity has been used; i. e., $\mathcal{L}(x_o,y_o) = \rho V\gamma(x_o,y_o)$ where $\gamma(x_o,y_o)$ is the bound vorticity distribution. The derivation of the integral equation (Equation 1) is given

in References 3 and 4. In this equation, $\alpha(x,y)$ is the known quantity and $\mathcal{L}(x_o,y_o)$ is the unknown. The method of solution employed is that of assumed loading modes. That is, the functional form of $\mathcal{L}(x_o,y_o)$ is assumed, this form being linear in certain undetermined constants. These constants are later evaluated by requiring exact tangency at a specified number of points on the wing. However, before this was accomplished, it was advantageous to perform a transformation of variables on Equation (1). This was done by choosing a coordinate system fixed to the blade with origin at the geometric center of the blade. The spanwise dimension was nondimensionalized by one-half of the span and the chordwise dimension by one-half of the chord. This transformation deforms the wing to a yawed square and is depicted in the following sketch.

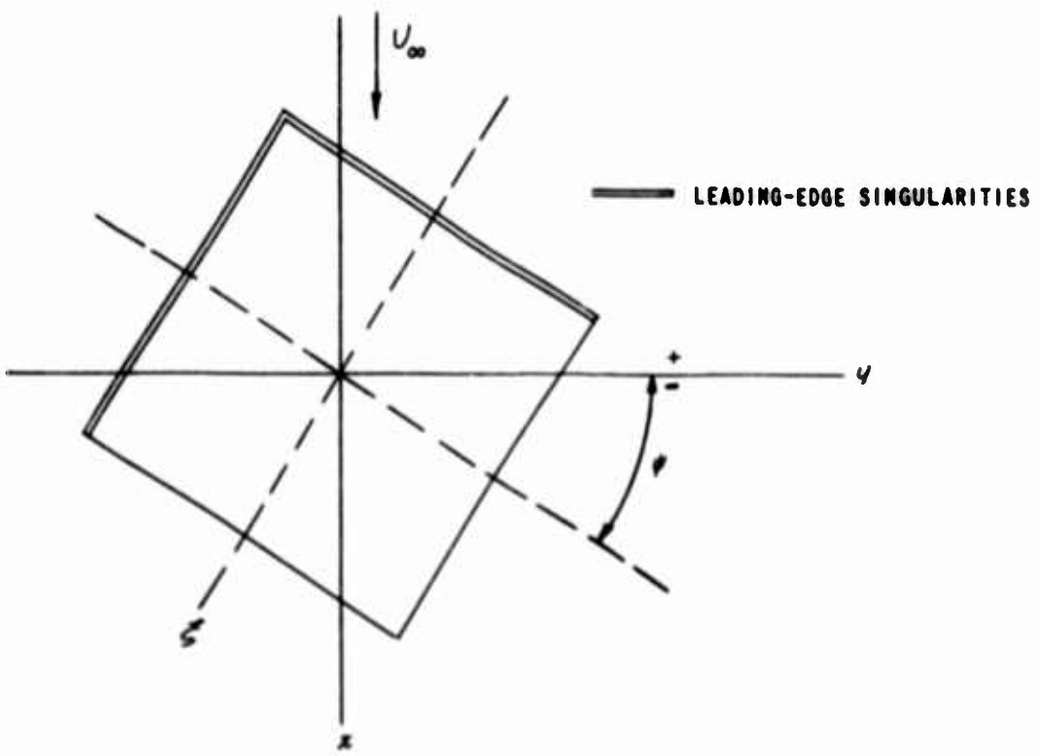

Equation (1) is then transformed to

$$\alpha(\xi,\eta) = -\frac{1}{8\pi}\int_{-1}^{1}\int_{-1}^{1} \frac{bc\mathcal{L}'(\xi_o,\eta_o)}{[c\sin\phi(\xi-\xi_o)+\cos\phi(\eta-\eta_o)]^2}\left\{1-\frac{c\cos\phi(\xi-\xi_o)-b\sin\phi(\eta-\eta_o)}{[c^2(\xi-\xi_o)^2+b^2(\eta-\eta_o)^2]^{\frac{1}{2}}}\right\}d\eta_o d\xi_o \quad (2)$$

where $\mathcal{L}_o'(\xi_o, \eta_o)$ is assumed to be of the following form:

$$\mathcal{L}_o' = \frac{P_1}{(1-\xi_o^2)^{\frac{1}{2}}} + \frac{P_2}{(1-\eta_o^2)^{\frac{1}{2}}} \tag{3}$$

where

$$\begin{aligned} P_1 = (1-\eta_o^2)\Big\{&\left[a_{00}+a_{01}\eta_o+a_{02}\eta_o^2+a_{03}\eta_o^3+a_{04}\eta_o^4\right](1-\xi_o) \\ &+\left[a_{10}+a_{11}\eta_o+a_{12}\eta_o^2+a_{13}\eta_o^3+a_{14}\eta_o^4\right](1-\xi_o^2) \\ &+\left[a_{20}+a_{21}\eta_o+a_{22}\eta_o^2+a_{23}\eta_o^3+a_{24}\eta_o^4\right](1-\xi_o^2)\xi_o\Big\} \\ &+\left(\tfrac{3}{4}-\tfrac{1}{2}\eta_o-\tfrac{1}{4}\eta_o^2\right)\Big\{a_{30}(1-\xi_o)+a_{31}(1-\xi_o^2)+a_{32}(1-\xi_o^2)\xi_o\Big\} \end{aligned} \tag{4}$$

$$\begin{aligned} P_2 = (1-\xi_o^2)\Big\{&\left[b_{00}+b_{01}\xi_o+b_{02}\xi_o^2+b_{03}\xi_o^3+b_{04}\xi_o^4\right](1-\eta_o) \\ &+\left[b_{10}+b_{11}\xi_o+b_{12}\xi_o^2+b_{13}\xi_o^3+b_{14}\xi_o^4\right](1-\eta_o^2) \\ &+\left[b_{20}+b_{21}\xi_o+b_{22}\xi_o^2+b_{23}\xi_o^3+b_{24}\xi_o^4\right](1-\eta_o^2)\eta_o\Big\} \\ &+\left(\tfrac{3}{4}-\tfrac{1}{2}\xi_o-\tfrac{1}{4}\xi_o^2\right)\Big\{b_{30}(1-\eta_o)+b_{31}(1-\eta_o^2)+b_{32}(1-\eta_o^2)\eta_o\Big\} \end{aligned} \tag{5}$$

where the a's and b's are the undetermined constants to be evaluated. It is noted that the first bracketed expression in P_1 and P_2 gives the type of loading that would be expected if one could formally split the spanwise and chordwise flow over the wing. These were chosen in this form so that the loading would approach the proper limits for Φ equal to zero or 90 degrees. The last bracketed term in P_1 and P_2 was added to prevent the loading at the apex from dropping to zero for intermediate values of Φ. It will be noted that the loadings were formed by multiplying the first three terms of a Birnbaum chordwise series by an appropriate spanwise function. The composite loading then possesses an appropriate airfoil-type singularity at the leading edges and has no loading at the trailing edges to conform to the Kutta condition. The expression for the loading contains 36 undetermined constants.

The expression for $\mathcal{L}_o'$ is then substituted in Equation (2), which can then be integrated to give an expression of the form

$$\alpha(\xi,\eta) = \sum_f \sum_g \left(A(\xi,\eta)_{f,g}\, a_{f,g} + L(\xi,\eta)_{f,g}\, \ell_{f,g} \right) \qquad (6)$$

which is linear in the a's and ℓ's. The a's and ℓ's are now found by selecting j values of ξ and i values of η such that $i \times j = 36$. In this fashion, a system of 36 linear algebraic equations is obtained from Equation (6). This system of equations is then solved for the a's and ℓ's. The integration required to obtain Equation (6) must be performed numerically. Since the kernel of Equation (2) contains a strong singularity, this involves considerable work in isolating the singularities before numerical integration can be performed. The integration is considerably eased by making use of Chebyshev-Gauss quadrature. The theory for this quadrature scheme is given in Reference 5. The application of this quadrature to lifting surface problems was evidently first made by Hsu (Reference 6). To a large extent, the present analysis is an adaptation of Hsu's technique to the yawed wing case. However, since the wing planform for the present application was not symmetrical for arbitrary yaw, many of the computational economics available for the symmetrical case could not be employed.

The loading modes used in the present analysis, as can be seen from Equations (4) and (5), were essentially parabolic in the spanwise direction. The conventional choice for the functional variation in the spanwise direction is elliptic. However, this choice is excluded from the present analysis because certain integrations to be performed require a finite spanwise slope of the wing tip.

For symmetrical planforms and elliptic spanwise mode shape, Hsu (Reference 6) was able to use the theory of Gaussian quadrature to develop explicit expressions for selection of the spanwise and chordwise collocation points such that the error in lift is minimized for a given number of points. Unfortunately, the same analysis cannot be employed for the yawed case.

Since the combined loading on the wing is of the form given by Equation (3), it was thought to be desirable to use the same expression to obtain the chordwise and spanwise collocation points and that these points should be symmetrically located about the midchord and midspan line of the wing. The selections were

$$\left.\begin{aligned} \xi_j &= \cos\left(\frac{2j-1}{2j_{max}}\right)\pi \\ \eta_i &= \cos\left(\frac{2i-1}{2i_{max}}\right)\pi \end{aligned}\right\} \qquad (7)$$

Location of the collocation points at these chordwise coordinates results in a minimum error (for a given number of chordwise collocation points) in the chordwise integration for sectional lift. The selected spanwise collocation-point locations provide the minimum error in the determination of the moment of a parabolic spanwise loading.

Since the present analysis involves several departures from conventional lifting surface developments, it was felt desirable to analyze the zero sweep or yaw case using the same techniques used in the yawed case and to compare the results with References 6 and 7. In particular, it was desired to assess the influence of using parabolic rather than elliptic spanwise loading modes and alternative selections of collocation points. This has been done for an aspect-ratio-one, rectangular wing and the results are summarized in Table X. The present program duplicates Hsu's results (Reference 6) when elliptic spanwise loading modes are used with Hsu's choice for the locations of collocation points. With the symmetrical distribution of Equation (7) as the choice of collocation-point locations, the elliptic loading modes give results which compare very favorably with those of References 6 and 7. With the same choice of locations for the collocation points, the parabolic spanwise loading modes give a total lift that is only slightly high. However, the resulting spanwise distribution of integrated chordwise loading, in this case, peaks near the wing tips. Therefore, the representation using parabolic loading modes in combination with 15 collocation points located according to Equation (7) is considered unsatisfactory. In an attempt to improve the results with parabolic loading modes, a minimum-square-error procedure was used with 30 collocation points and 15 undetermined constants. This did not result in significant improvement. It appears then that more modes and/or an alternate location scheme for the collocation points will have to be considered to achieve a satisfactory representation employing parabolic spanwise loading modes.

Although there was some question of the adequacy of the parabolic loading modes and the collocation-point locations in the unyawed case, the computer program for the arbitrarily yawed wing was, nevertheless, developed using this representation. However, its application to the case of an aspect-ratio-one wing yawed at 45 degrees did not predict the symmetries in the loading which are inherent in the problem. This failure cannot be attributed to the use of parabolic modes or particular collocation-point locations, but whether it is due to an error in the theoretical formulation or in the computer program remains an unanswered question until further study can be made.

F. CORRELATION OF THEORETICAL AND EXPERIMENTAL RESULTS

In view of the difficulties discussed above, theoretical calculations for comparison with measurements were limited to the special cases for the unyawed wing corresponding to the rotor blade at ψ = 90, 180, and 270 degrees. Elliptic spanwise loading modes were used with

Table X

COMPARISON OF VARIOUS THEORETICAL RESULTS FOR LIFT ON AN ASPECT RATIO = 1.0 RECTANGULAR WING

METHOD	C_{L_α}	COLLOCATION POINTS
CAL PARABOLIC LOADING MODES $M_N = 0$	1.5806	$\zeta_j = \cos\frac{(2j-1)\pi}{2j_{max}}$; $j_{max} = 3$ $\eta_i = \cos\frac{(2i-1)\pi}{2i_{max}}$; $i_{max} = 5$
CAL ELLIPTIC LOADING MODES $M_N = 0$	1.4535	$\zeta_j = \cos\frac{(2j-1)\pi}{2j_{max}}$; $j_{max} = 3$ $\eta_i = \cos\frac{(2i-1)\pi}{2i_{max}}$; $i_{max} = 6$
HSU (REF. 6) $M_N = 0.2$ $M_N = 0$	1.51 1.48	$\zeta_j = -\cos\frac{2j\pi}{2j_{max}+1}$; $j_{max} = 3$ $\eta_i = -\cos\frac{i\pi}{i_{max}+1}$; $i_{max} = 3$
HSU (REF. 6) $M_N = 0.2$ $M_N = 0$	1.497 1.47	$\zeta_j = -\cos\frac{2j\pi}{2j_{max}+1}$; $j_{max} = 5$ $\eta_i = -\cos\frac{i\pi}{i_{max}+1}$; $i_{max} = 5$
NASA KERNEL FUNCTION (REF. 7)	1.455	(FOR SELECTION OF COLLOCATION POINTS SEE REF. 7)
JONES	1.57	SLENDER-WING THEORY

18 collocation points located in accordance with Equation (7). The computed results and the corresponding measured values are presented in Table XI for the three azimuth positions when the shaft tilt angle, α_s , = 0 degrees, the blade root pitch angle, θ_R , = + 13 degrees, and the dynamic pressure, q , = 28.85 psf. In general, the agreement between the theoretical and experimental results is not satisfactory. However, as discussed below, some of the discrepancies can be explained.

Table XI

COMPARISON OF MEASURED AND PREDICTED RESULTS

$\alpha_s = 0°$, $\theta_R = +13°$, $q = 28.85$ psf

	ψ = 90 DEGREES		ψ = 180 DEGREES		ψ = 270 DEGREES	
	MEASURED	COMPUTED	MEASURED	COMPUTED	MEASURED	COMPUTED
LIFT (lb)	700	520.11	3	5.44	-333	-529.2
ROLLING MOMENT (ft-lb)	6074	4248.7	-61	-104.74	-3536	-4402.5
PITCHING MOMENT (ft-lb)	91	-2.705	-1	-1.651	238	339.26
DRAG (lb)	22	11.44		0	-34	-13.17
DRAG MOMENT (ft-lb)	331	64.88		0	-518	-25.57

In comparing the results obtained at ψ = 90 degrees, it is noted that the lift, rolling moment, drag force, and drag moment are underpredicted. It is believed that a reason that the drag force and moment are less than measured is the fact that the profile drag and friction drag were not considered in the calculations.

The difference in the predicted and measured lift and rolling moment corresponds to the incremental lift and rolling moment that would be obtained from a 2-1/2-degree change in the angle of attack. As previously noted in this report, the experimental results that were obtained indicated that the root geometric angle of attack for zero lift was approximately 1-1/2 degrees different from that expected for a rigid blade having no tip effects. Flow angularity, however, is not believed to be the cause of the discrepancy between theory and experiment, as a flow angularity of anywhere near the magnitude required could not be justified on the basis of calibration results obtained for the NASA-Ames 40-by-80-foot wind tunnel.

For ψ = 270 degrees, the same general comments concerning the correlation of the theoretical and experimental results apply.

CONCLUSIONS

It is concluded that the primary objective of the research program was realized, in that a set of blade strain and aerodynamic loading data were obtained simultaneously for a nonrotating helicopter blade arbitrarily oriented with respect to the free stream. In addition to this general conclusion, the following specific observations are made as regards the aerodynamic characteristics of a rotor blade fixed with respect to the free stream:

1. At azimuth angles of approximately 90 and 270 degrees, the variations of the lift, rolling moment, and pitching moment about the quarter chord with angle of attack are as expected, based on sectional data.

2. The minimum drag forces at azimuth angles of 90 and 270 degrees are about equal, which is not what would be expected, based on sectional data.

3. The normal force and rolling moment tend to zero at an azimuth angle of 180 degrees for all shaft tilt and blade angles tested.

4. The data appear to be consistent with the expectation that blade beamwise flexibility would reduce either the dynamic pressure or the rotor shaft tilt angle at which blade bending divergence occurs at an azimuth angle of 180 degrees.

5. The blade pitch angle is an ineffective control parameter at an azimuth angle of 180 degrees.

6. For all azimuth angles except those at 180 $\pm$ 10 degrees and 360 $\pm$ 10 degrees, the rotor shaft angle and blade pitch angle are significant control parameters.

7. The azimuthal variations of the drag and drag moment for any blade pitch setting decrease as the shaft tilt angle is varied from + 5 degrees to - 5 degrees.

8. The root normal force or root beamwise bending moment can be made zero at each azimuthal position by proper choice of blade angle.

9. The magnitude and azimuthal variation of the blade root pitching moment about the blade root quarter chord tend to be small for the blade on the advancing side but large for the retreating side.

10. In the azimuth angle range of $225 \leq \psi \leq 330$ degrees, a dynamic instability is encountered for both positive and negative blade root geometric angles. There is some evidence in the records presented that the instabilities have the characteristics of stall flutter.

11. The contribution of the flexible blade bending slope to the effective angle of attack is significant in the establishment of the instability boundary.

RECOMMENDATIONS

On the basis of the results obtained during this program, it is recommended that the following additional research efforts be undertaken in support of the successful development of stoppable rotor configurations:

1. Obtain aerodynamic and strain data for a stoppable rotor configuration in the stopping and starting operational modes.

2. Conduct additional tests with rotor blades having different stiffnesses, twist distributions, and planforms to determine the effects of these parameters on the instabilities that were encountered.

3. Continue the development of a suitable theory for predicting the aerodynamic characteristics of stoppable rotor configurations.

4. Develop a theory for predicting the stall flutter characteristics of stoppable rotor configurations.

REFERENCES

1. Bell Helicopter Company, MEASUREMENT OF DYNAMIC AIR LOADS ON A FULL-SCALE SEMIRIGID ROTOR, TCREC TR 62-42, U. S. Army Transportation Research Command, Fort Eustis, Virginia, December 1962.

2. Golub, R., and McLachlan, W., IN-FLIGHT MEASUREMENT OF ROTOR BLADE AIRLOADS, BENDING MOMENTS, AND MOTIONS, TOGETHER WITH ROTOR SHAFT LOADS AND FUSELAGE VIBRATION, ON A TANDEM ROTOR HELICOPTER, Volume I - Instrumentation and In-Flight Recording System, USAAVLABS Technical Report 67-9A, May 1967.

3. Multhopp, H., METHODS FOR CALCULATING THE LIFT DISTRIBUTION OF WINGS (SUBSONIC LIFTING SURFACE THEORY), Aeronautical Research Council Technical Report R&M No. 2884, 1955.

4. Ashley, H. and Landahl, M., AERODYNAMICS OF WINGS AND BODIES, Reading, Massachusetts, Addison-Wesley Publishing Co., Inc., 1965, p. 132.

5. Hildebrand, F. B., INTRODUCTION TO NUMERICAL ANALYSIS, New York, McGraw-Hill Book Co., Inc. 1956.

6. Hsu, P. T., SOME RECENT DEVELOPMENTS IN THE FLUTTER ANALYSIS OF LOW ASPECT RATIO WINGS, Proceedings of National Specialists' Meeting on Dynamics and Elasticity, IAS, Fort Worth, Texas, 1958.

7. Watkins, C. E., Woolston, D. S., and Cunningham, H. J., A SYSTEMATIC KERNEL FUNCTION PROCEDURE FOR DETERMINING AERODYNAMIC FORCES ON OSCILLATING OR STEADY FINITE WINGS AT SUBSONIC SPEEDS, NASA TR R-48, 1959.

8. Critzos, C. C., Heyson, H. H., and Boswinkle, R. W., AERODYNAMIC CHARACTERISTICS OF NACA 0012 AIRFOIL SECTION AT ANGLES OF ATTACK FROM 0° TO 180°, NACA TN 3361, January 1955.

9. Cotton, R. H., FULL SCALE WIND TUNNEL TESTS OF THE LOCKHEED CL-870 IN FLIGHT STOPPING AND FOLDING ROTOR SYSTEM - DYNAMIC RESPONSE RESULTS, Lockheed Report No. 19652, Lockheed Aircraft Corporation, 25 June 1966.

10. Halfman, R. L., Johnson, H. C., and Haley, S. M., EVALUATION OF HIGH-ANGLE-OF-ATTACK AERODYNAMIC-DERIVATIVE DATA AND STALL-FLUTTER PREDICTION TECHNIQUES, NACA TN 2533, November 1951.

11. Ham, N. D., and Garelick, M. S., DYNAMIC STALL CONSIDERATIONS IN HELICOPTER ROTORS, Journal of the American Helicopter Society, Vol. 13, No. 2, April 1968, pp. 49 - 55.

12. Rainey, A. G., MEASUREMENT OF AERODYNAMIC FORCES FOR VARIOUS MEAN ANGLES OF ATTACK ON AN AIRFOIL OSCILLATING IN PITCH AND ON TWO FINITE-SPAN WINGS OSCILLATING IN BENDING WITH EMPHASIS ON DAMPING IN THE STALL, NACA Report No. 1305, 1957.

13. Ham, N. D., and Young, M. I., TORSIONAL OSCILLATION of HELICOPTER BLADES DUE TO STALL, Journal of Aircraft, Vol. 3, No. 3, May - June 1966, pp. 218 - 224.

14. Lindsey, W. F., Daley, B. M., and Humphreys, M. D., THE FLOW AND FORCE CHARACTERISTICS OF SUPERSONIC AIRFOILS AT HIGH SUBSONIC SPEEDS, NACA TN 1211, March 1947.

15. Lizak, A. A., TWO-DIMENSIONAL WIND-TUNNEL TESTS OF AN H-34 MAIN ROTOR AIRFOIL SECTION, TREC Tech Report 60-53, U. S. Army Transportation Research Command, Fort Eustis, Virginia, September 1960.

16. Pope, A., THE FORCES AND MOMENTS OVER AN NACA 0015 AIRFOIL THROUGH 180° ANGLE OF ATTACK, Aero Digest, April 1949, pp. 76, 78 and 100.

17. Milne, W. E., NUMERICAL CALCULUS, Princeton, Princeton University Press, 1949.

18. Langefors, B., ILL-CONDITIONED MATRICES, SAAB TN 22, Saab Aircraft Company, Linkoping, Sweden, 1953.

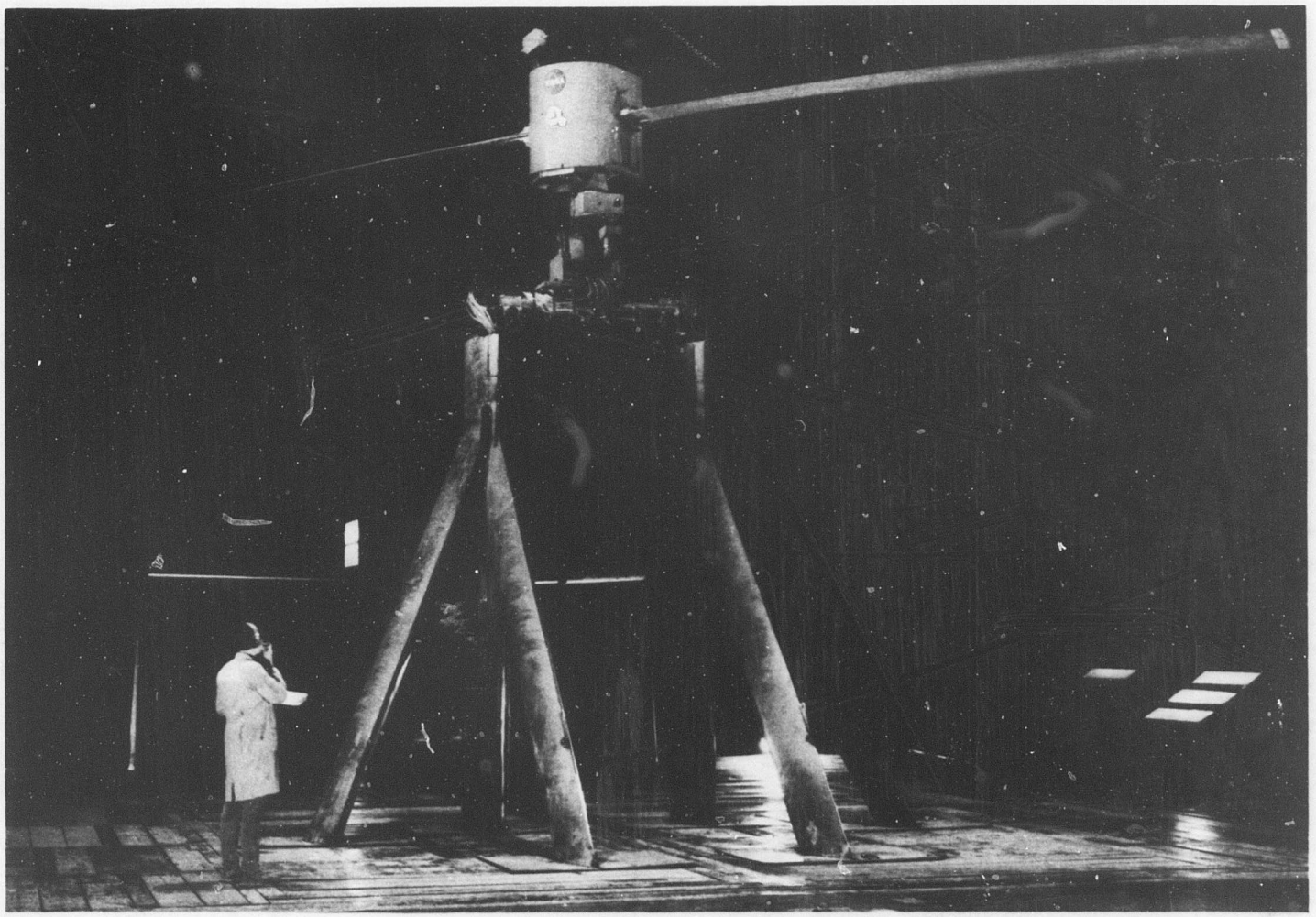

Figure 1. TEST INSTALLATION IN WIND TUNNEL

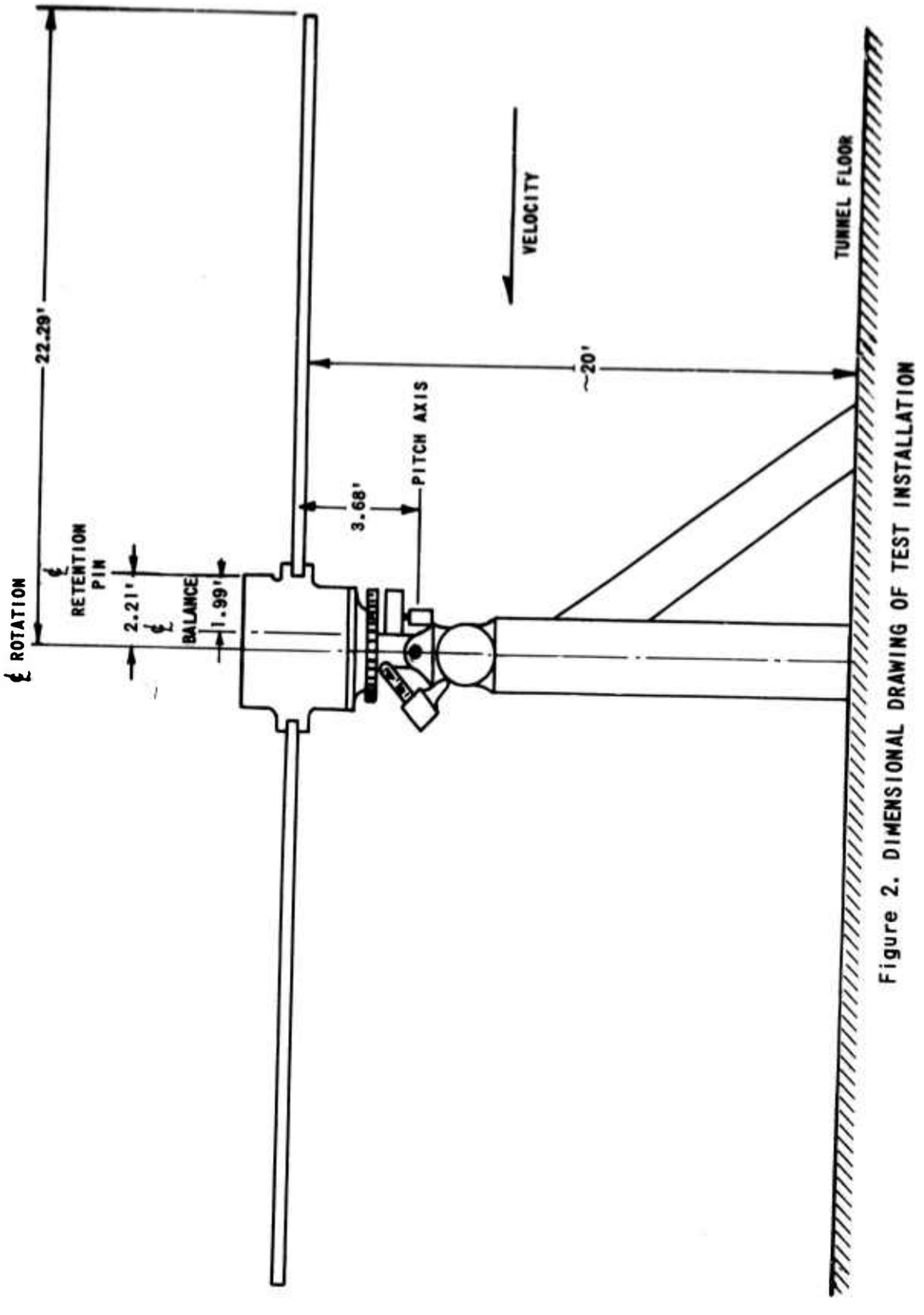

Figure 2. DIMENSIONAL DRAWING OF TEST INSTALLATION

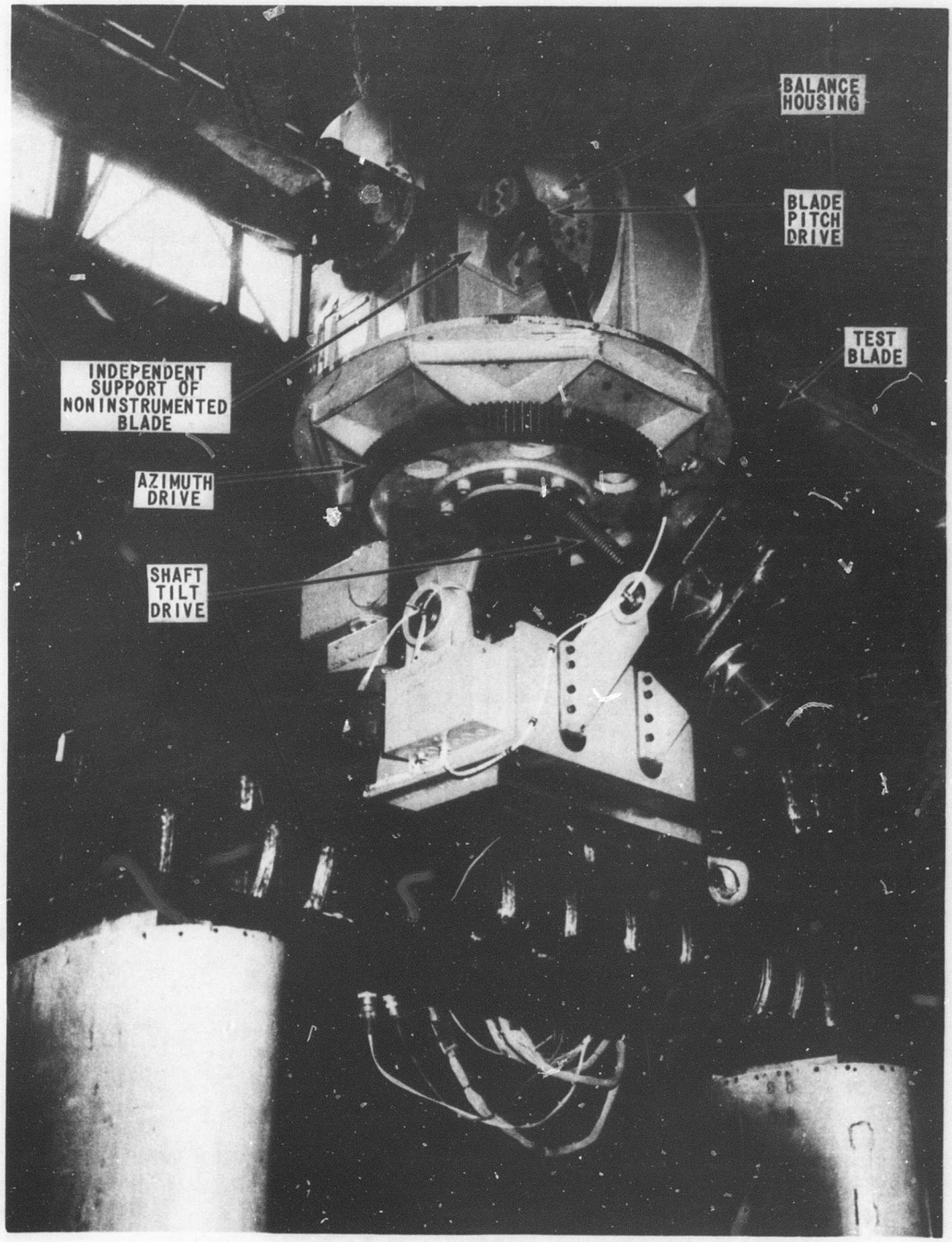

Figure 3. INSTALLATION SHOWING ACTUATOR DRIVE SYSTEMS

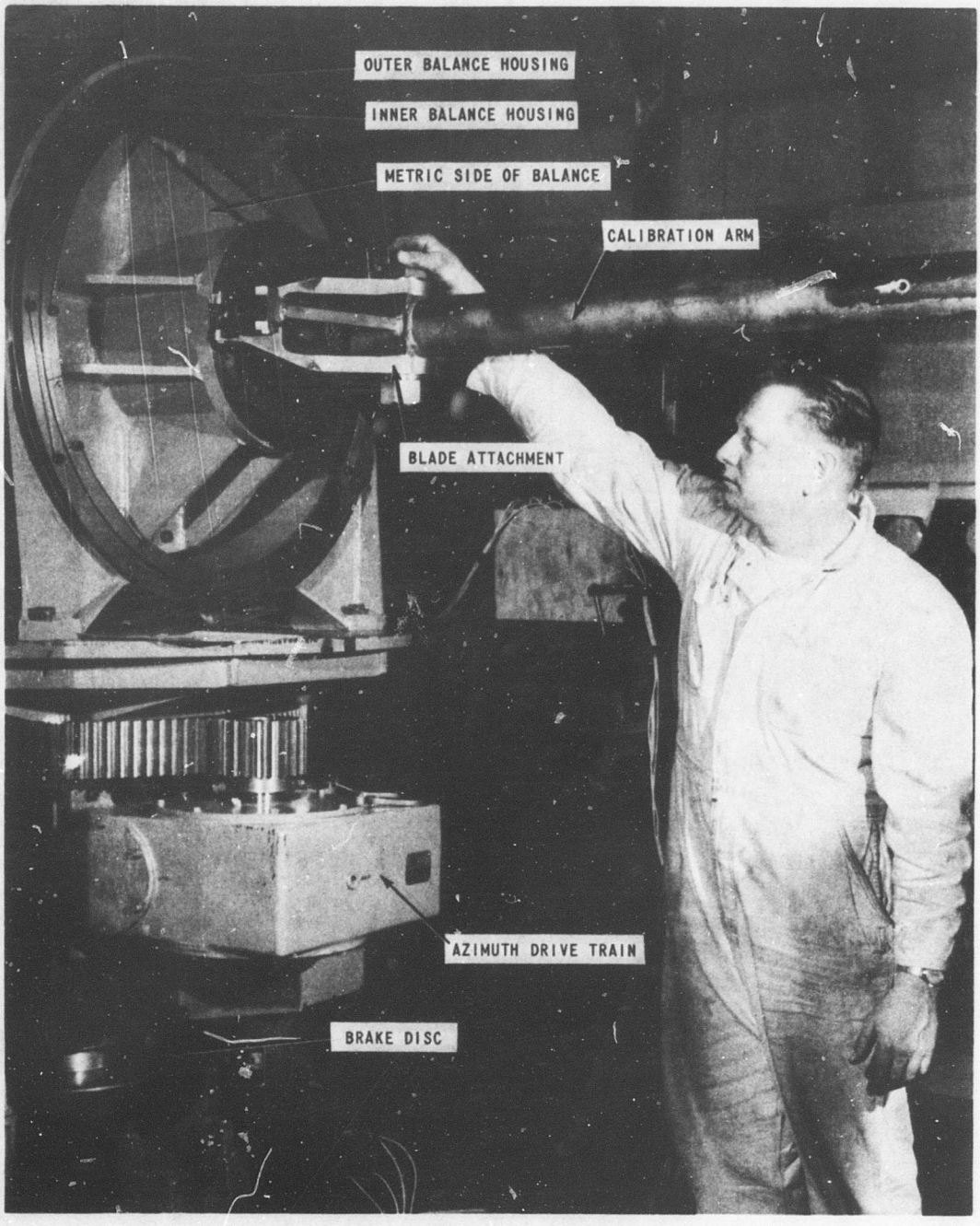

Figure 4. BALANCE ASSEMBLY ON SUPPORT STRUCTURE

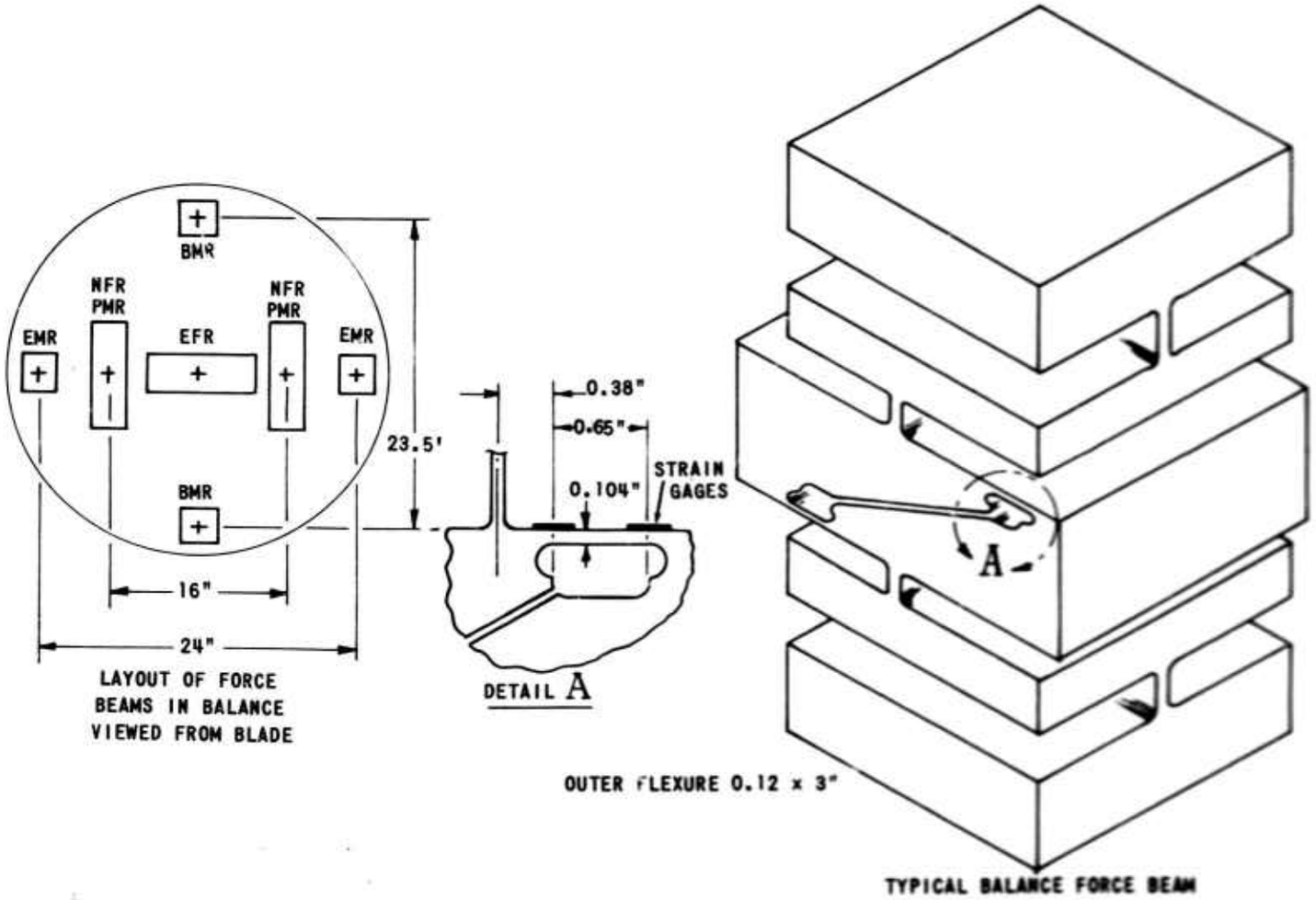

Figure 5. DIMENSIONAL DRAWING OF FORCE BALANCE SYSTEM

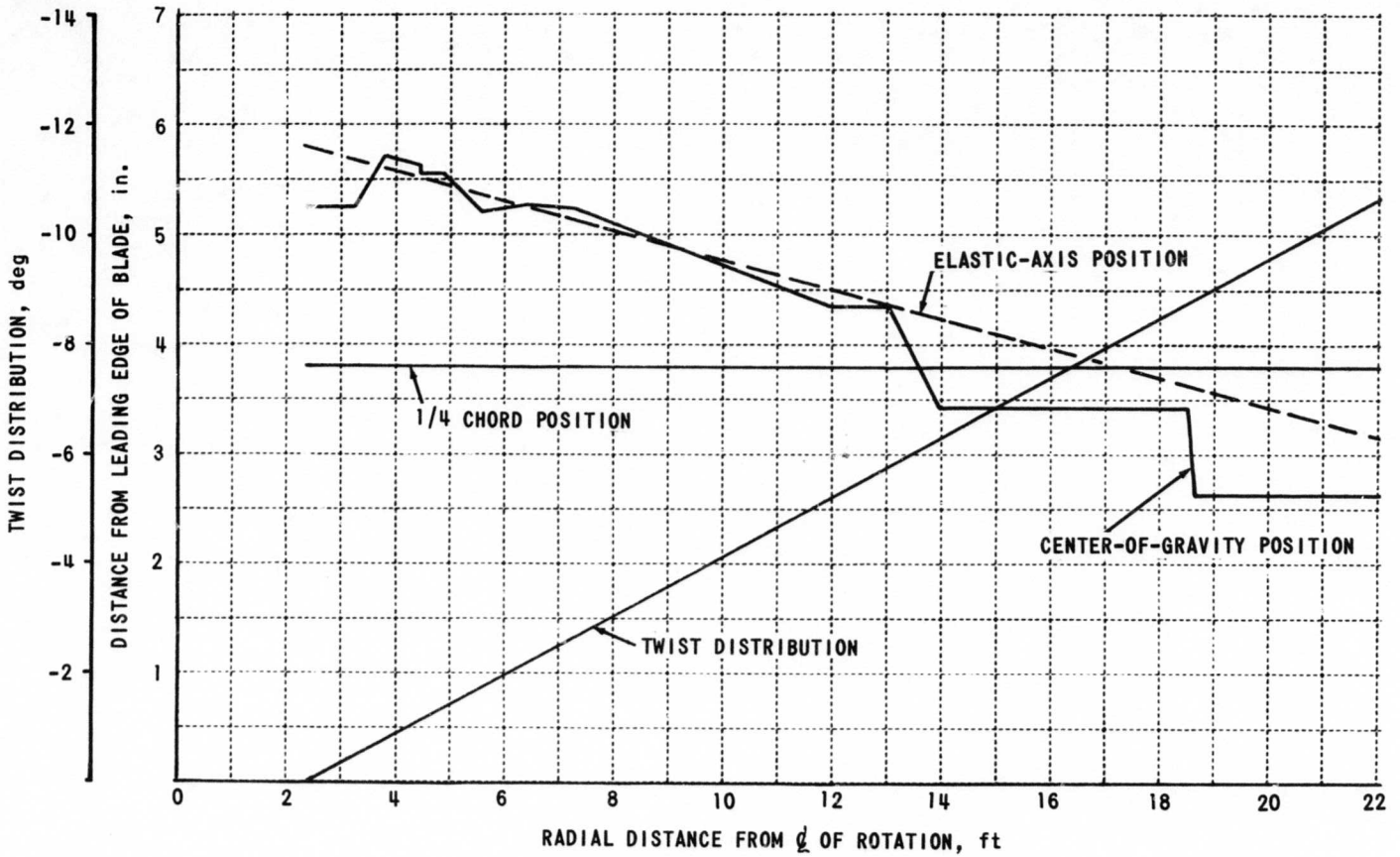

Figure 6. GEOMETRIC PROPERTIES OF THE TEST BLADE

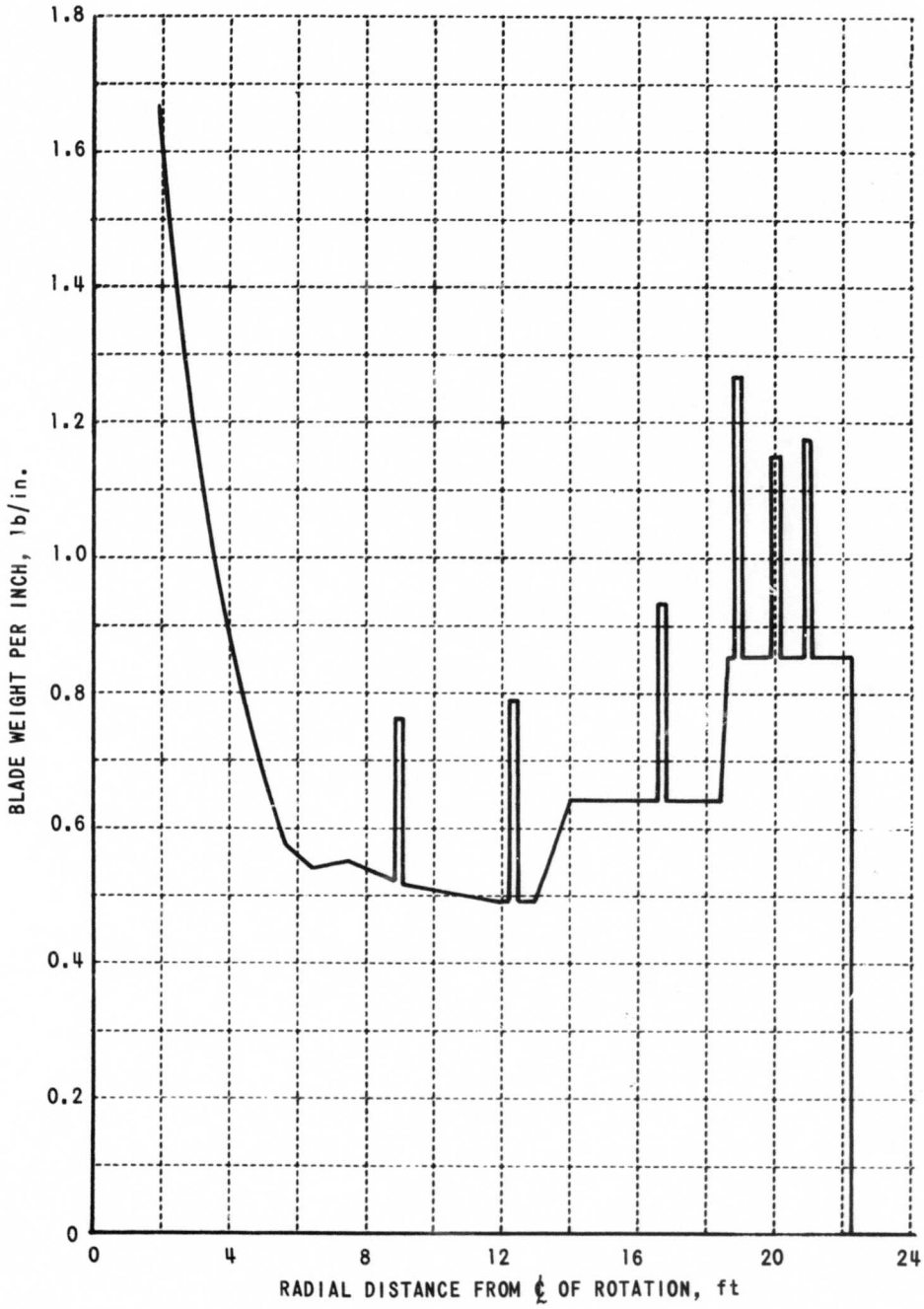

Figure 7. BLADE WEIGHT DISTRIBUTION

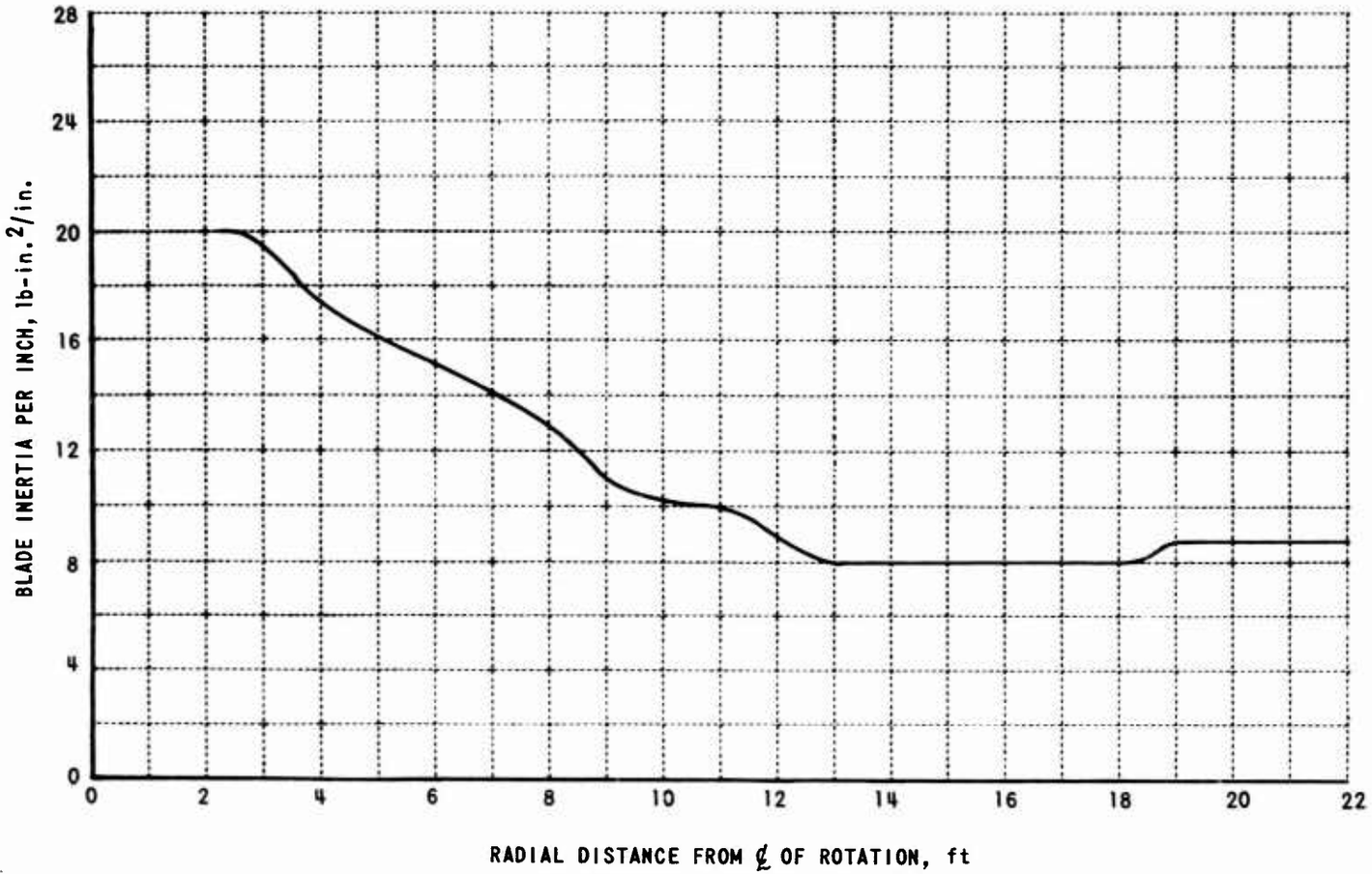

Figure 8. BLADE INERTIA DISTRIBUTION

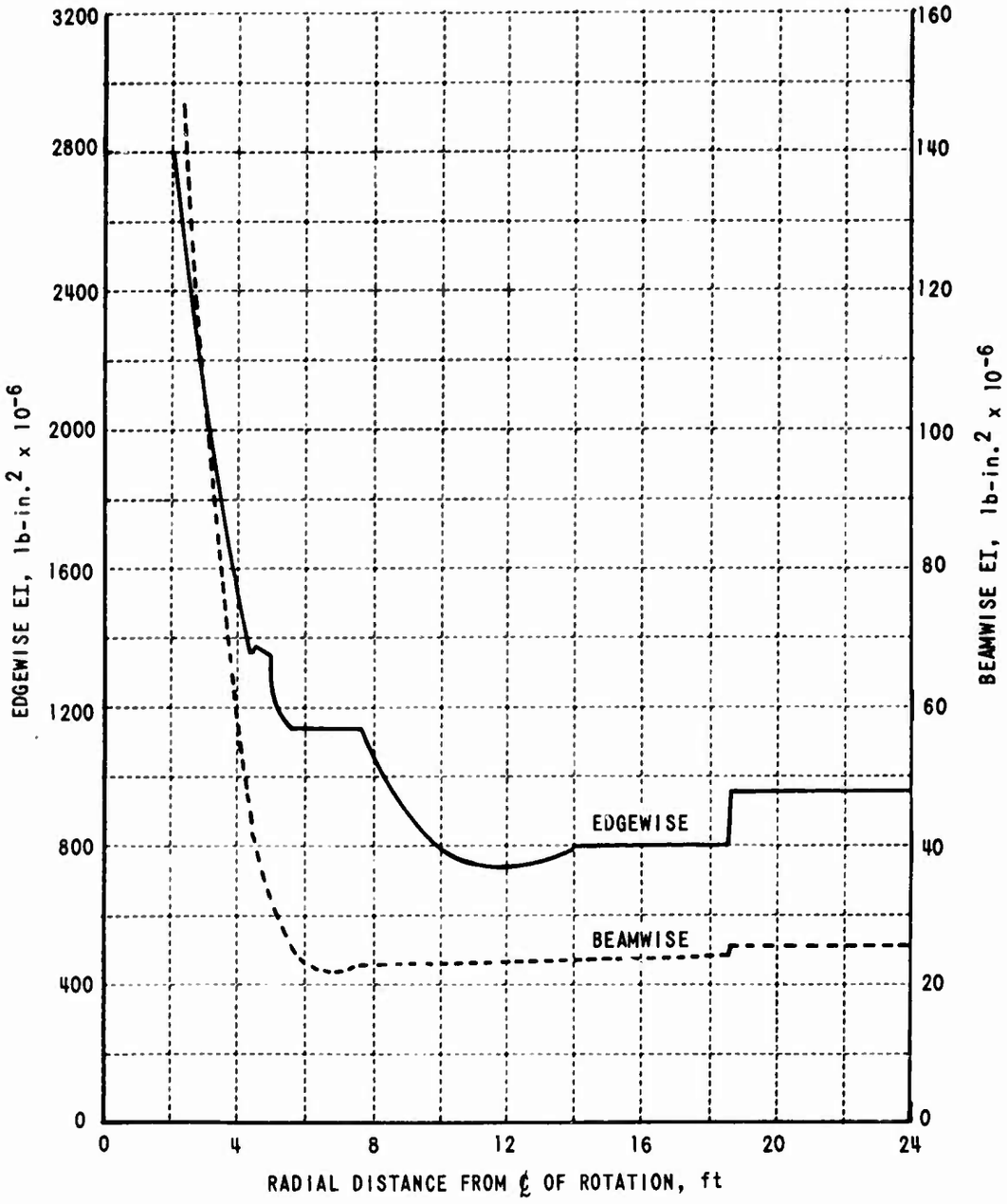

Figure 9. BLADE BENDING STIFFNESS DISTRIBUTION

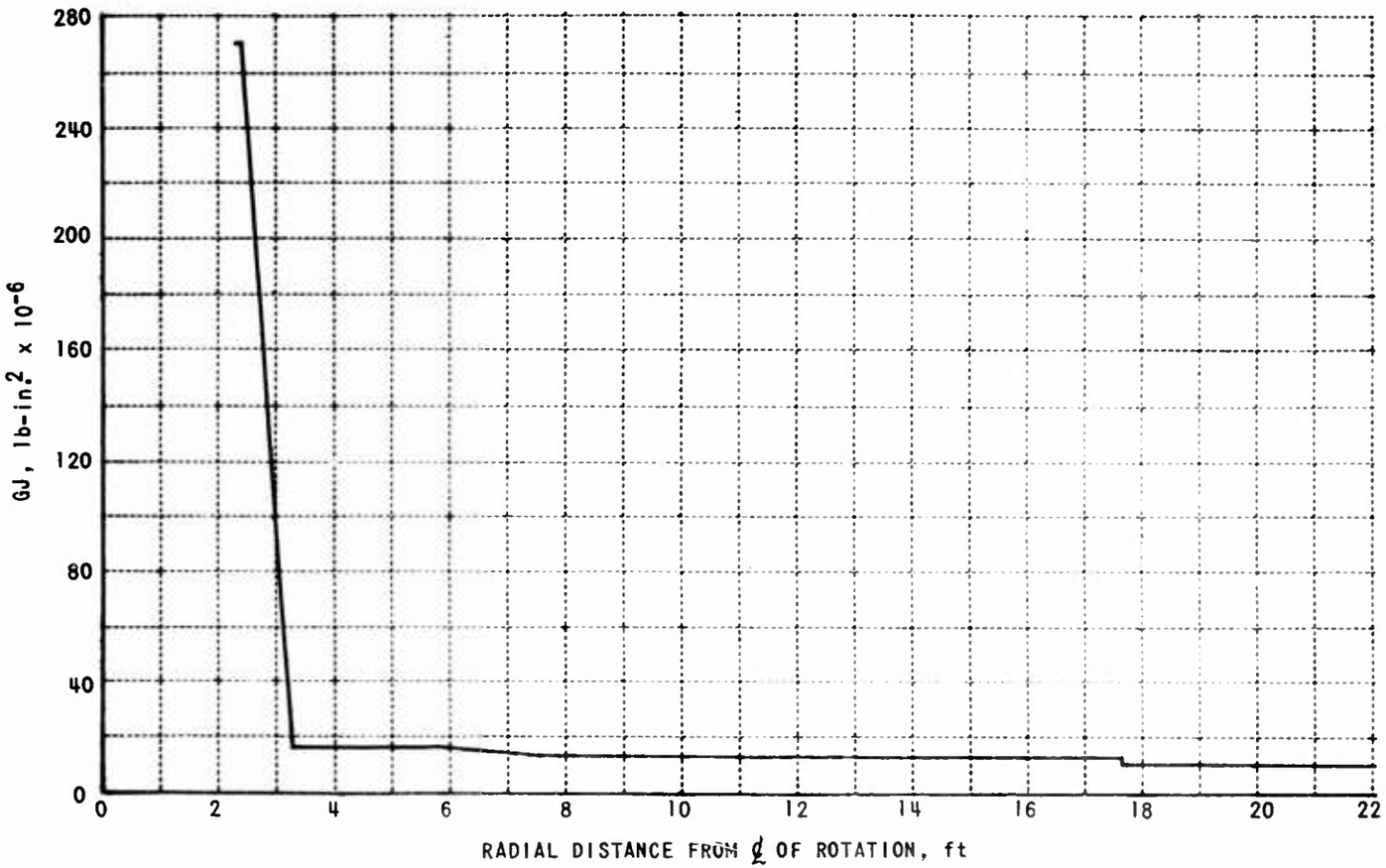

Figure 10. BLADE TORSIONAL STIFFNESS DISTRIBUTION

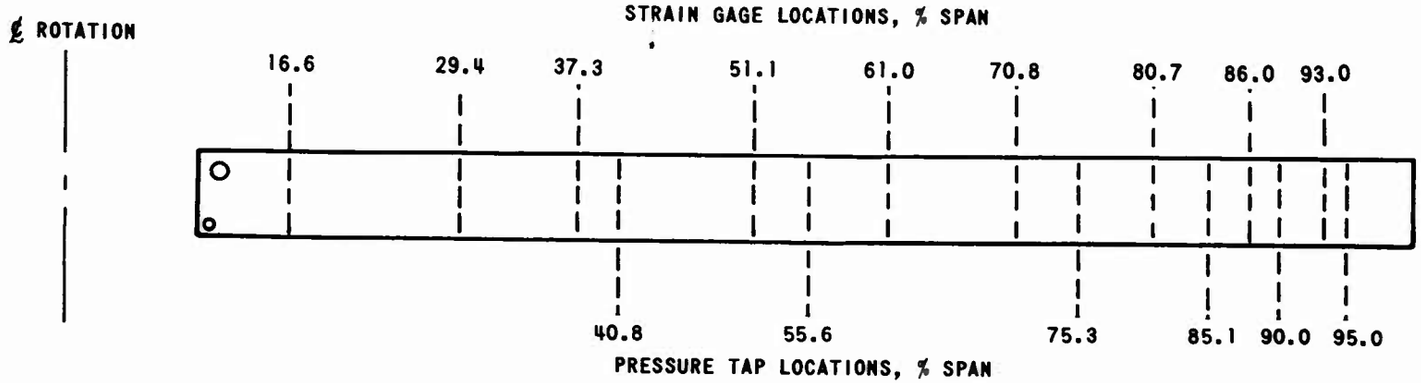

Figure 11. DIMENSIONAL DRAWING SHOWING SPANWISE LOCATIONS OF STRAIN GAGES AND PRESSURE TAPS

Figure 12. PRESSURE TAP AND STRAIN GAGE INSTALLATION AT 85-PERCENT SPAN

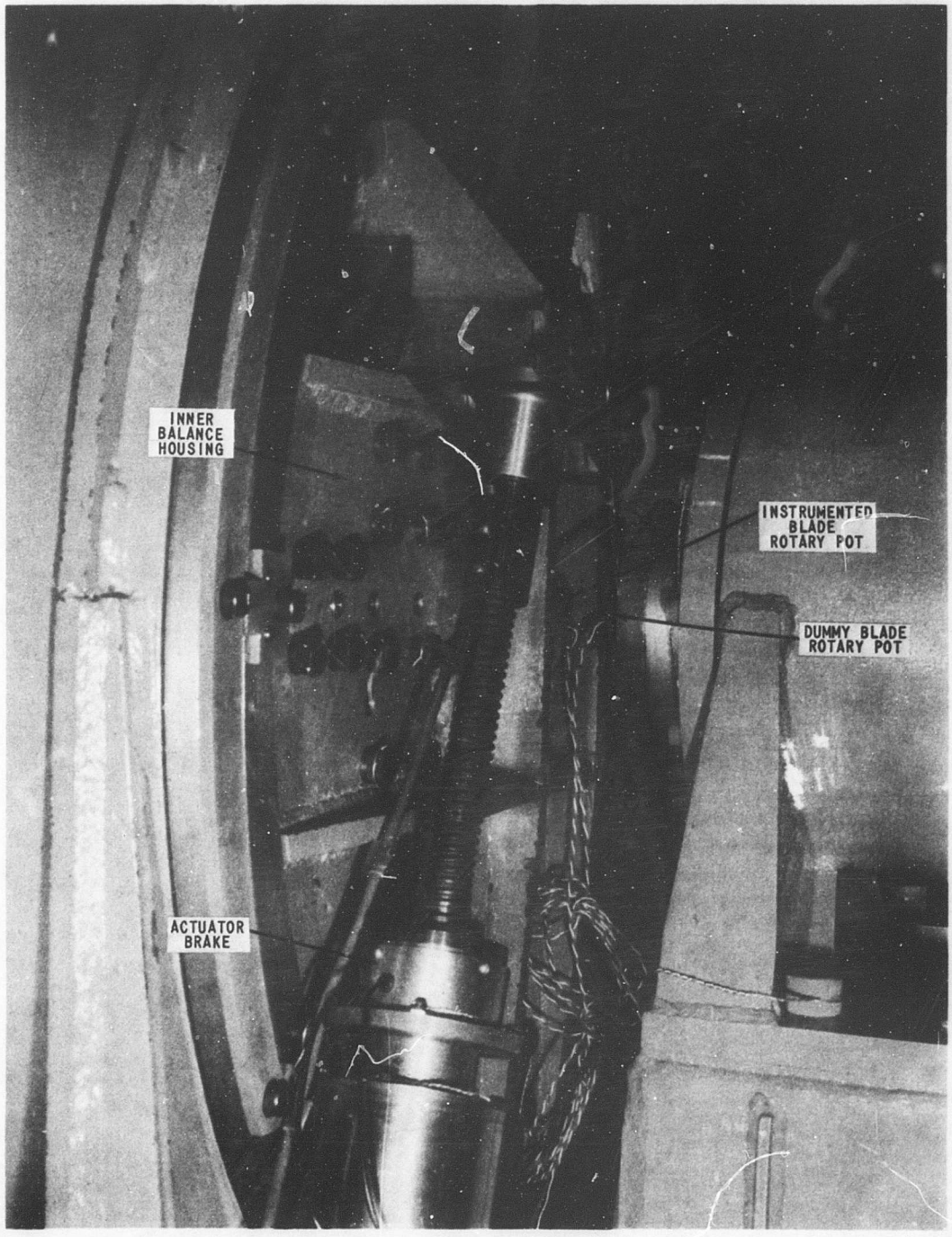

Figure 13. BLADE PITCH ANGLE TRANSDUCERS

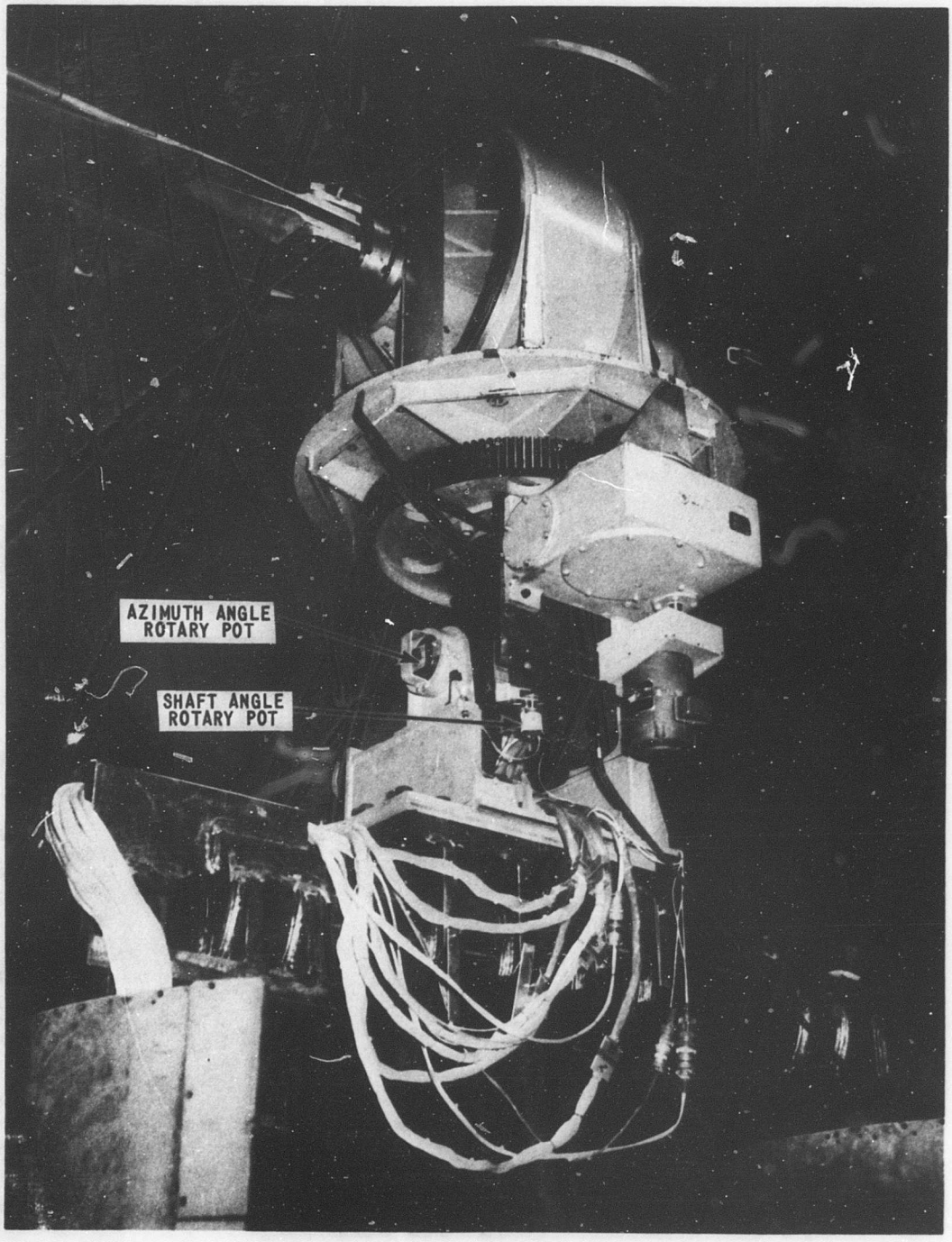

Figure 14. AZIMUTH AND SHAFT ANGLE TRANSDUCERS

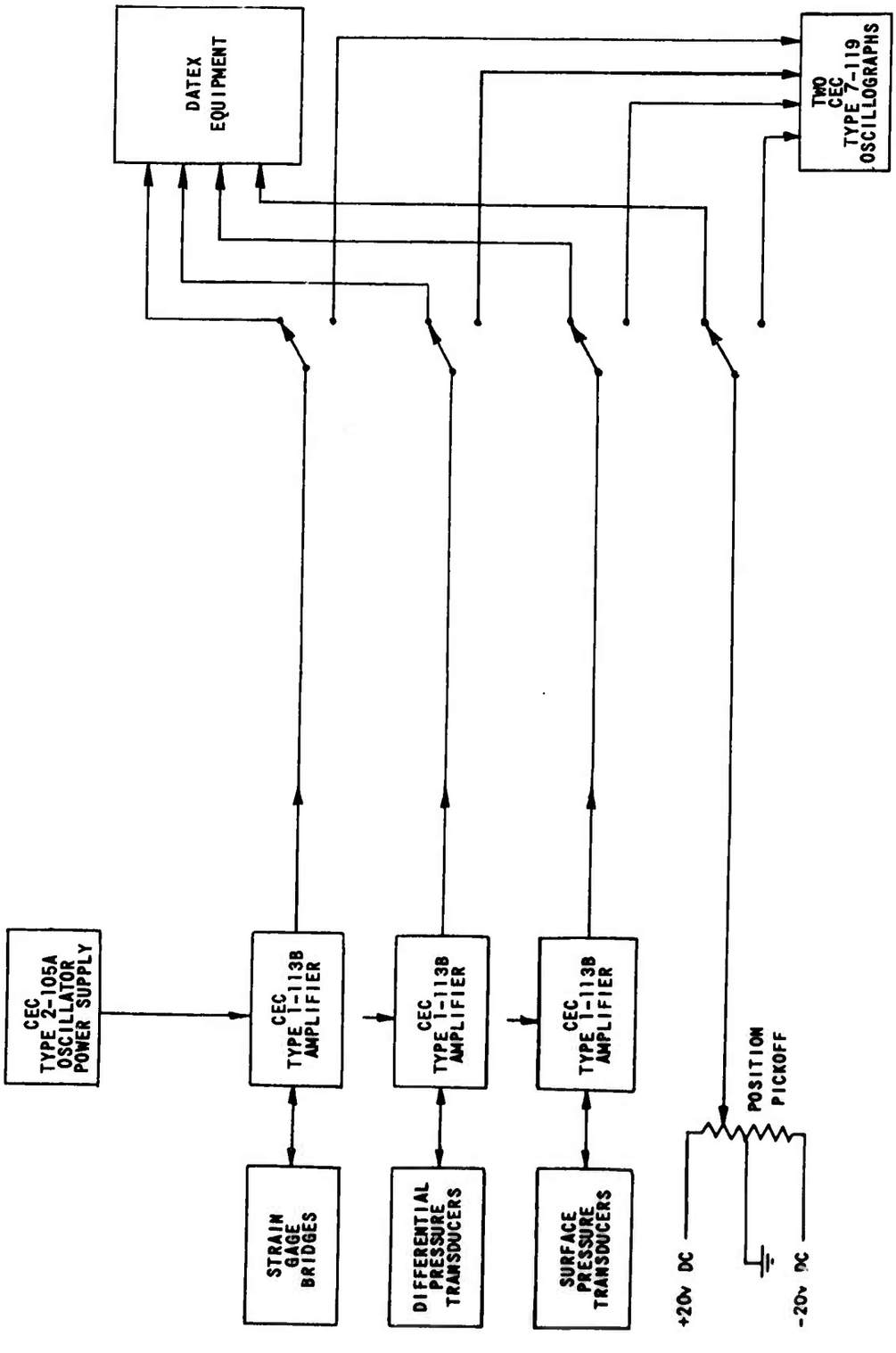

Figure 15. INSTRUMENTATION BLOCK DIAGRAM

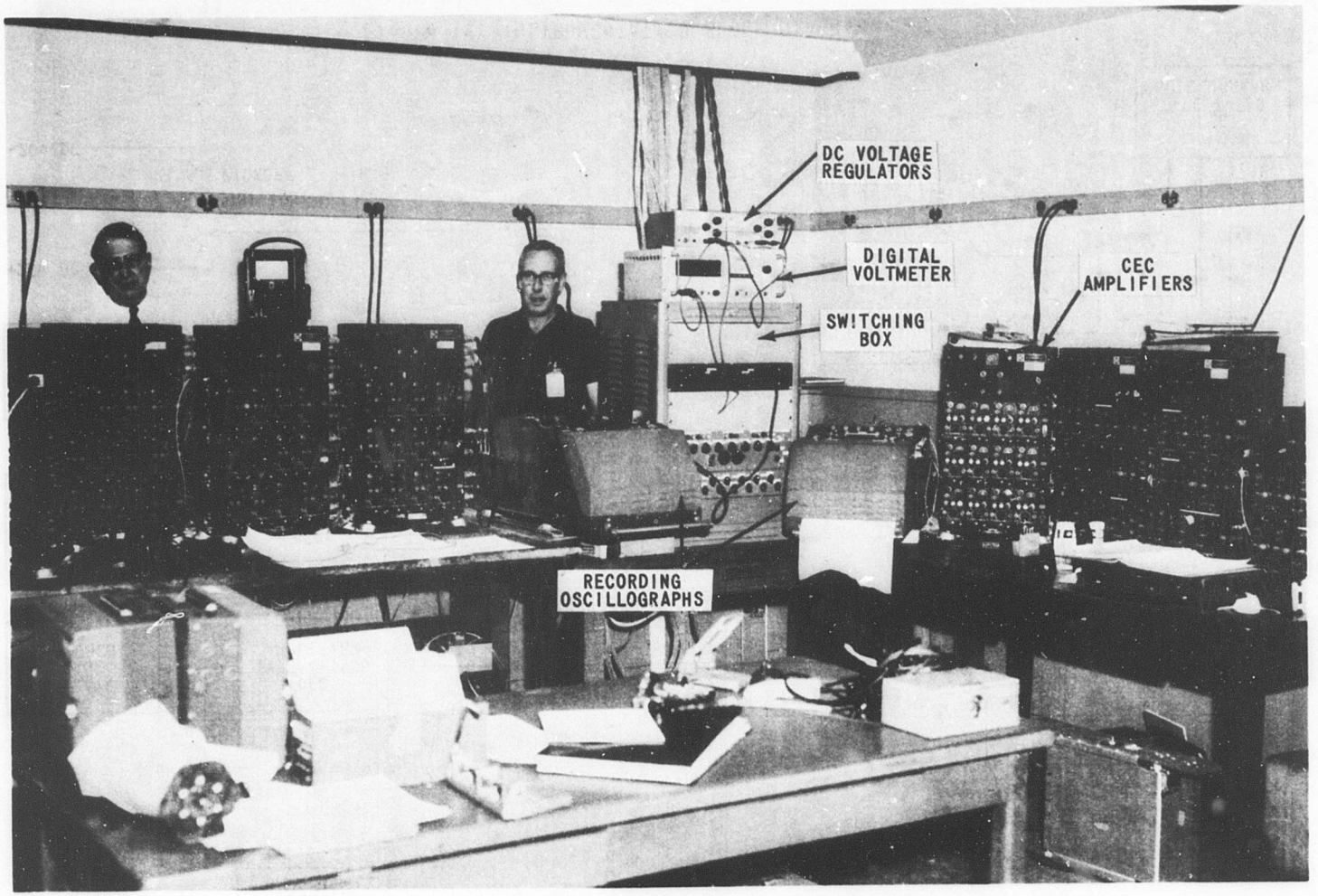

Figure 16. INSTRUMENTATION SETUP IN CONTROL ROOM

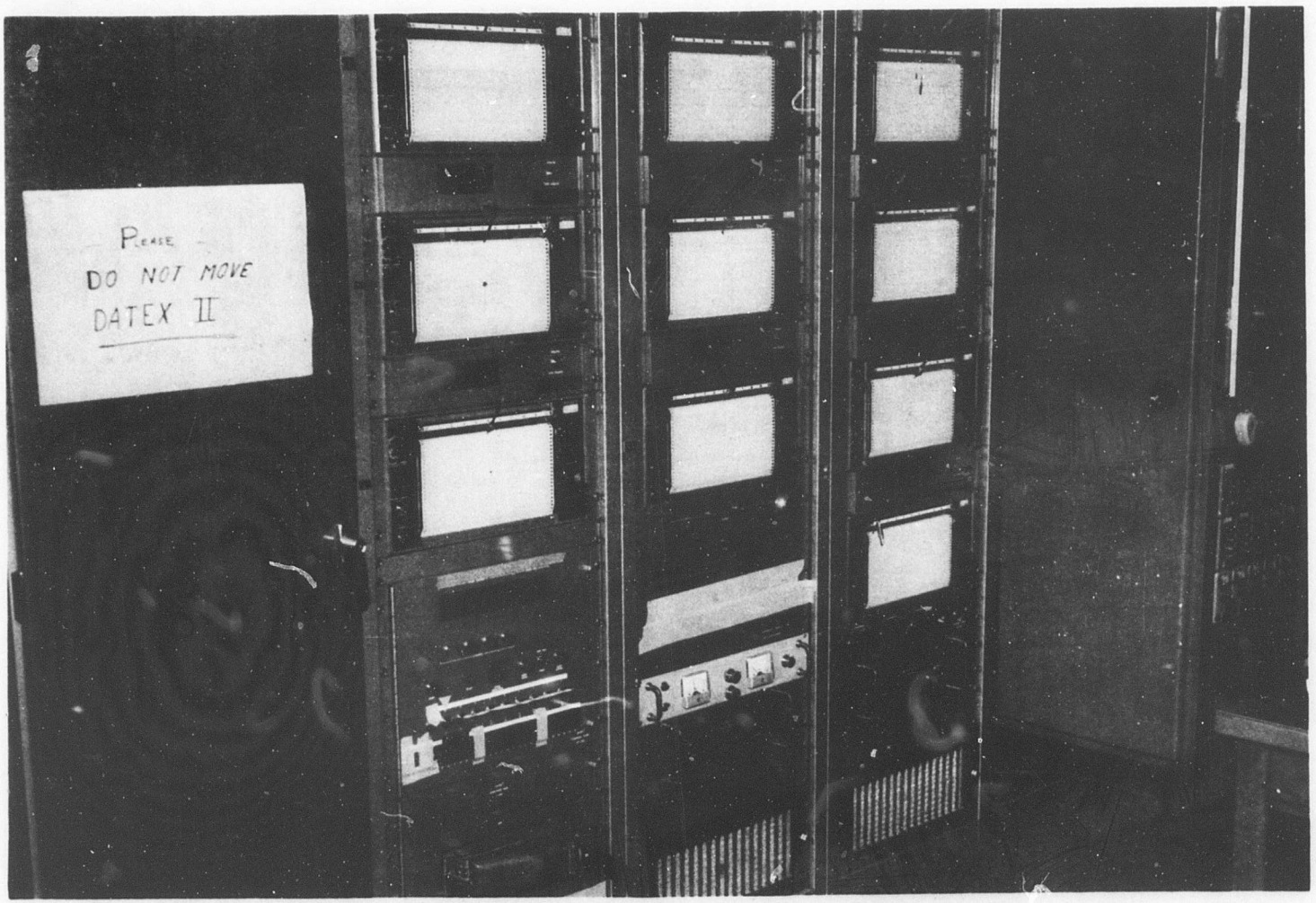

Figure 17. DATEX II STRIP CHART READOUT

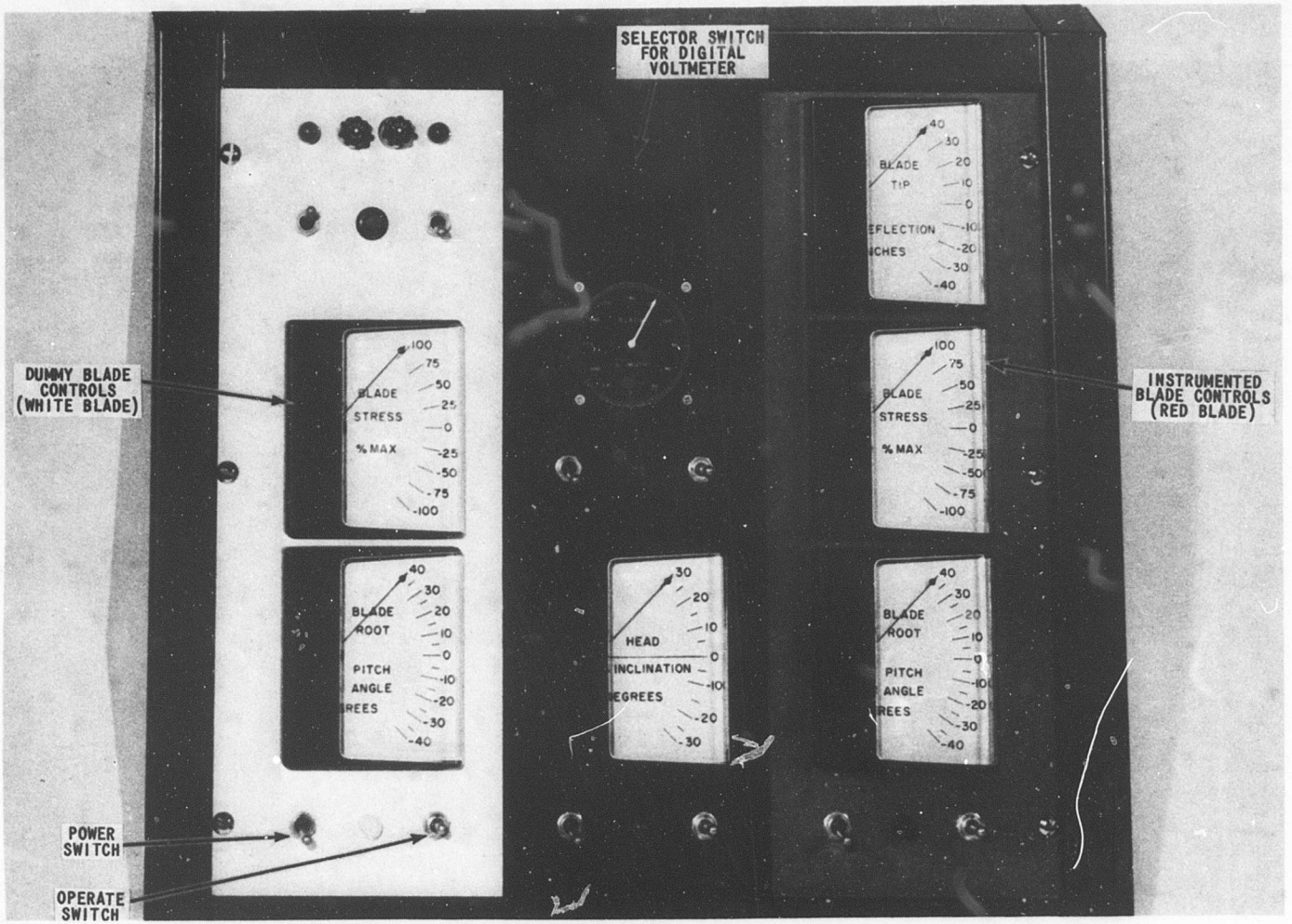

Figure 18. OPERATOR'S CONTROL PANEL

$$
\begin{bmatrix} PMR \\ NFR \\ BMR \\ EMR \\ EFR \end{bmatrix}
=
\begin{bmatrix}
+ & 634.7149 & -588.8668 & -334.6934 & 388.5589 & -1.507101 & 3.099517 \\
- & 640.8061 & -582.7954 & 32.61325 & -30.23853 & 13.83756 & -6.210736 \\
+ & 945.2300 & 868.4112 & -467.7179 & 540.5893 & 4.931594 & 0.5879168 \\
- & 953.4598 & 875.2118 & 39.48748 & -37.53034 & -3.317540 & 2.044534 \\
+ & -3.731666 & -2.015897 & 2782.766 & 4831.021 & -8.682843 & 4.869818 \\
- & 71.38457 & 96.72740 & 1122.670 & 5962.433 & 70.60197 & -9.371341 \\
+ & -20.82749 & 7.968296 & 593.5458 & -453.2496 & 4754.464 & 37.47499 \\
- & -0.7657846 & 30.62313 & 306.5189 & -518.1761 & 4896.665 & -8.536496 \\
+ & 13.02278 & 5.707138 & 152.0892 & -182.6319 & 11.31958 & 345.8053 \\
- & 19.95805 & 13.42255 & 216.3754 & -223.9616 & 37.37880 & 337.1821
\end{bmatrix}
\begin{bmatrix} X_1 \\ X_2 \\ X_3 \\ X_4 \\ X_5 \\ X_6 \end{bmatrix}
$$

Figure 19. BALANCE CONVERSION MATRIX

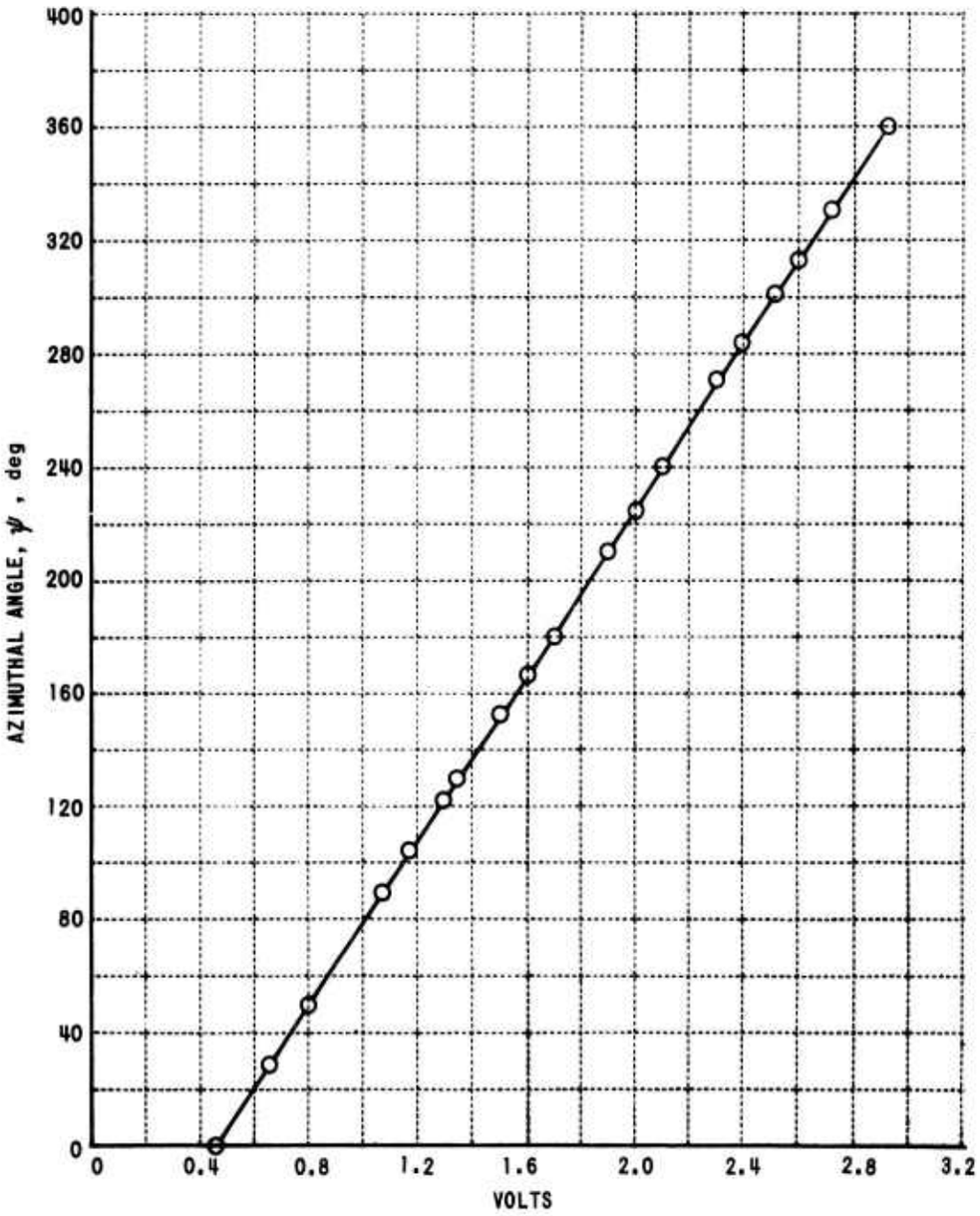

Figure 20. AZIMUTH ANGLE CALIBRATION CURVE

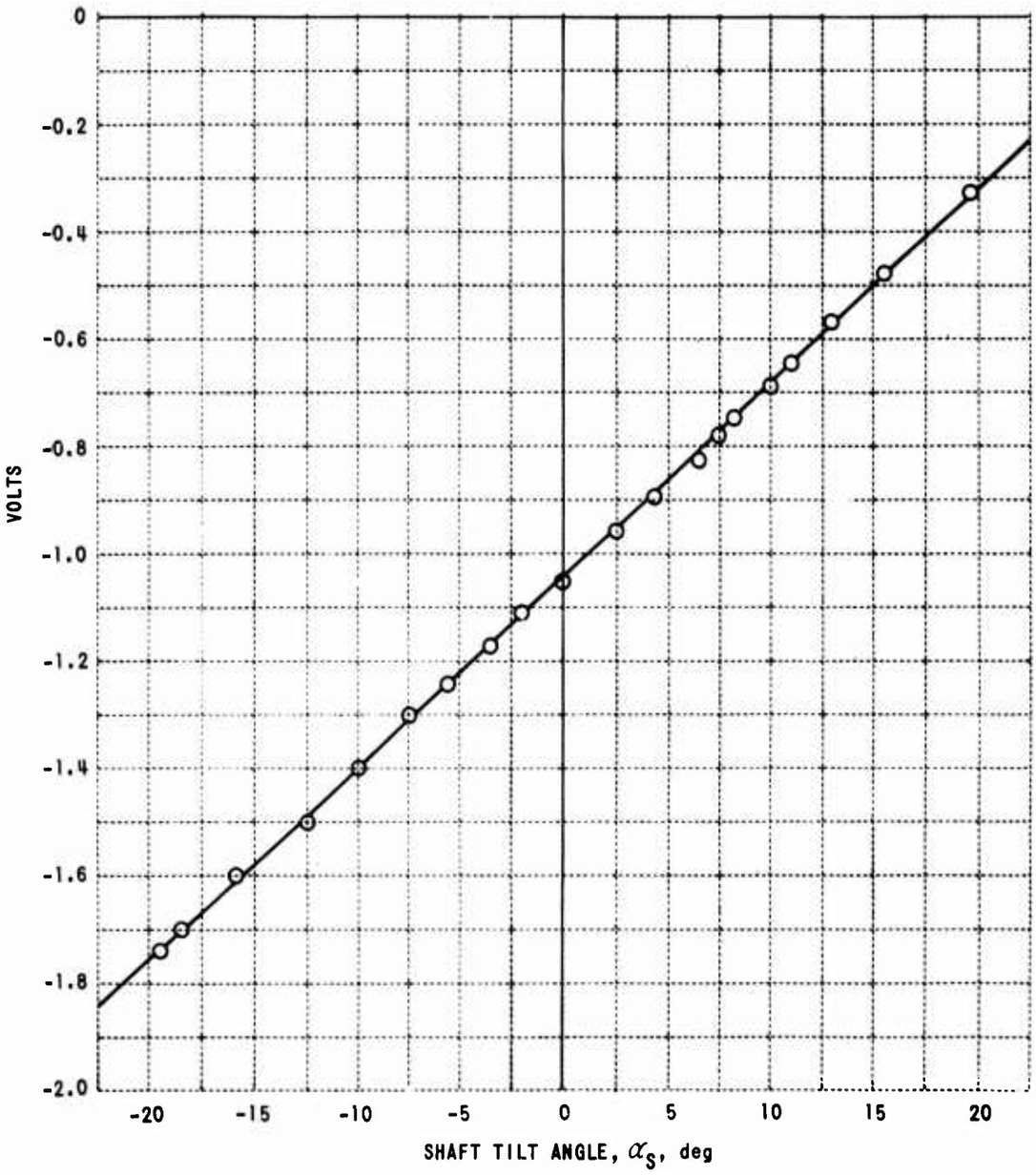

Figure 21. SHAFT TILT ANGLE CALIBRATION CURVE

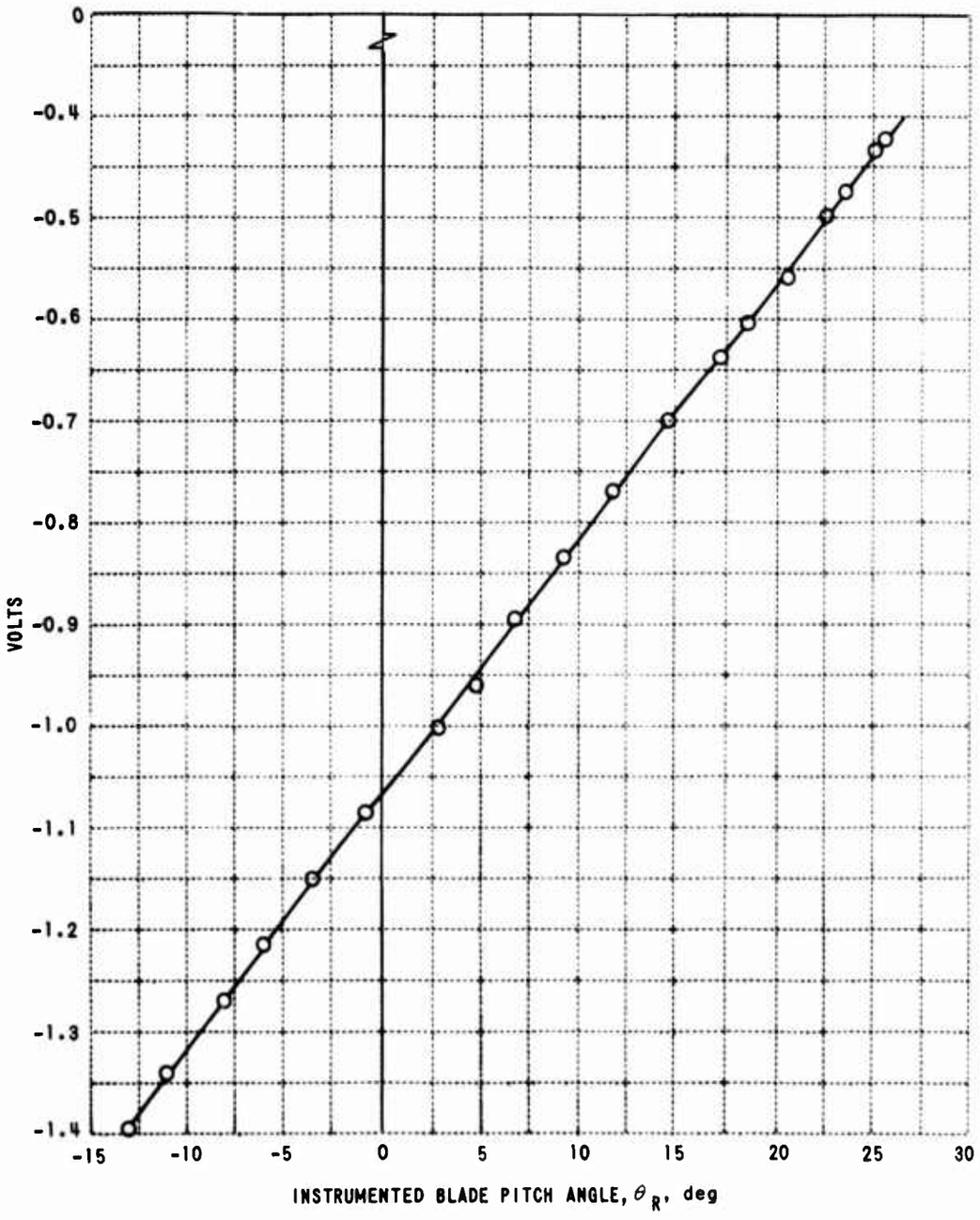

Figure 22. PITCH ANGLE CALIBRATION CURVE - INSTRUMENTED BLADE

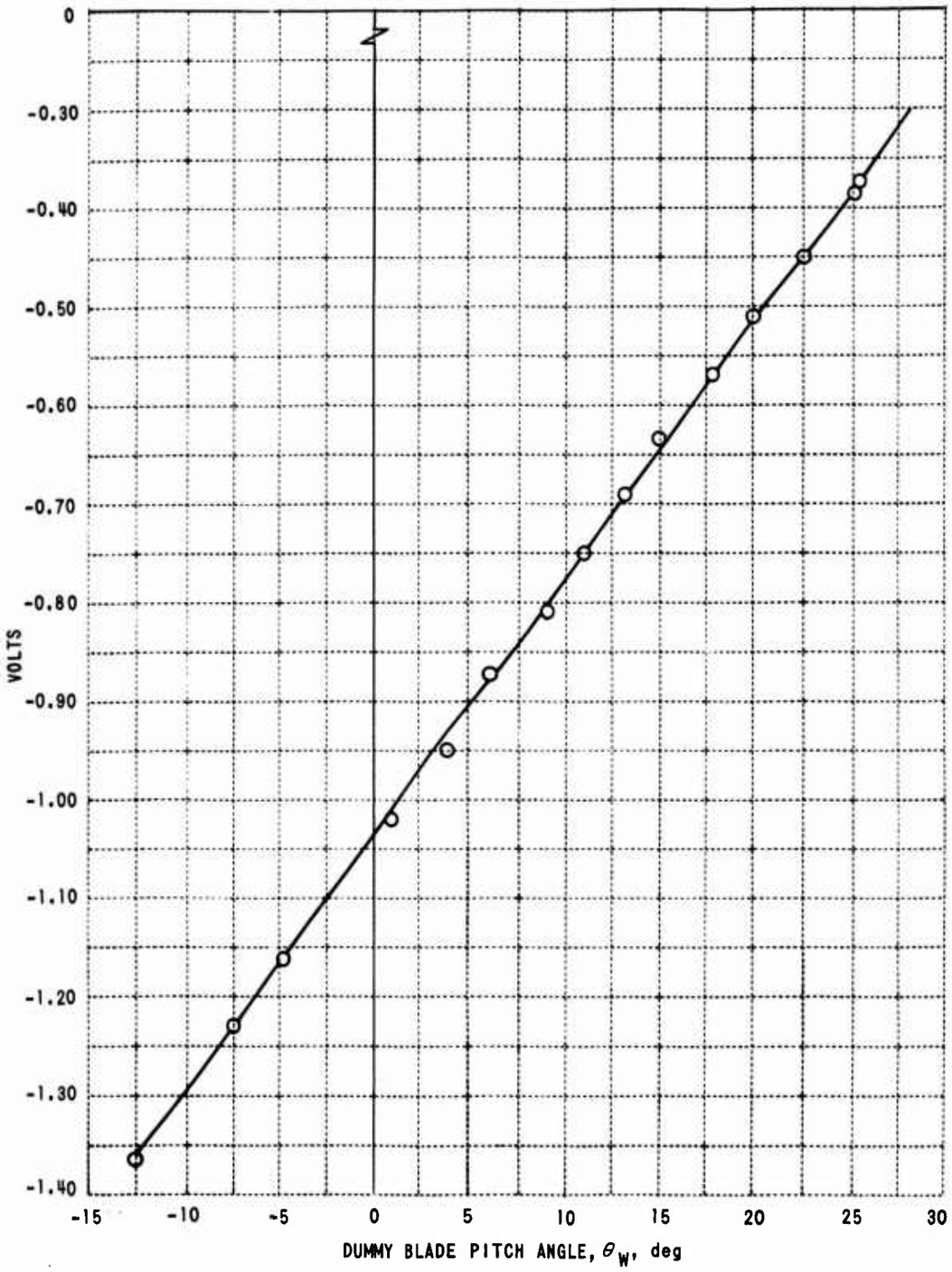

Figure 23. PITCH ANGLE CALIBRATION CURVE - DUMMY BLADE

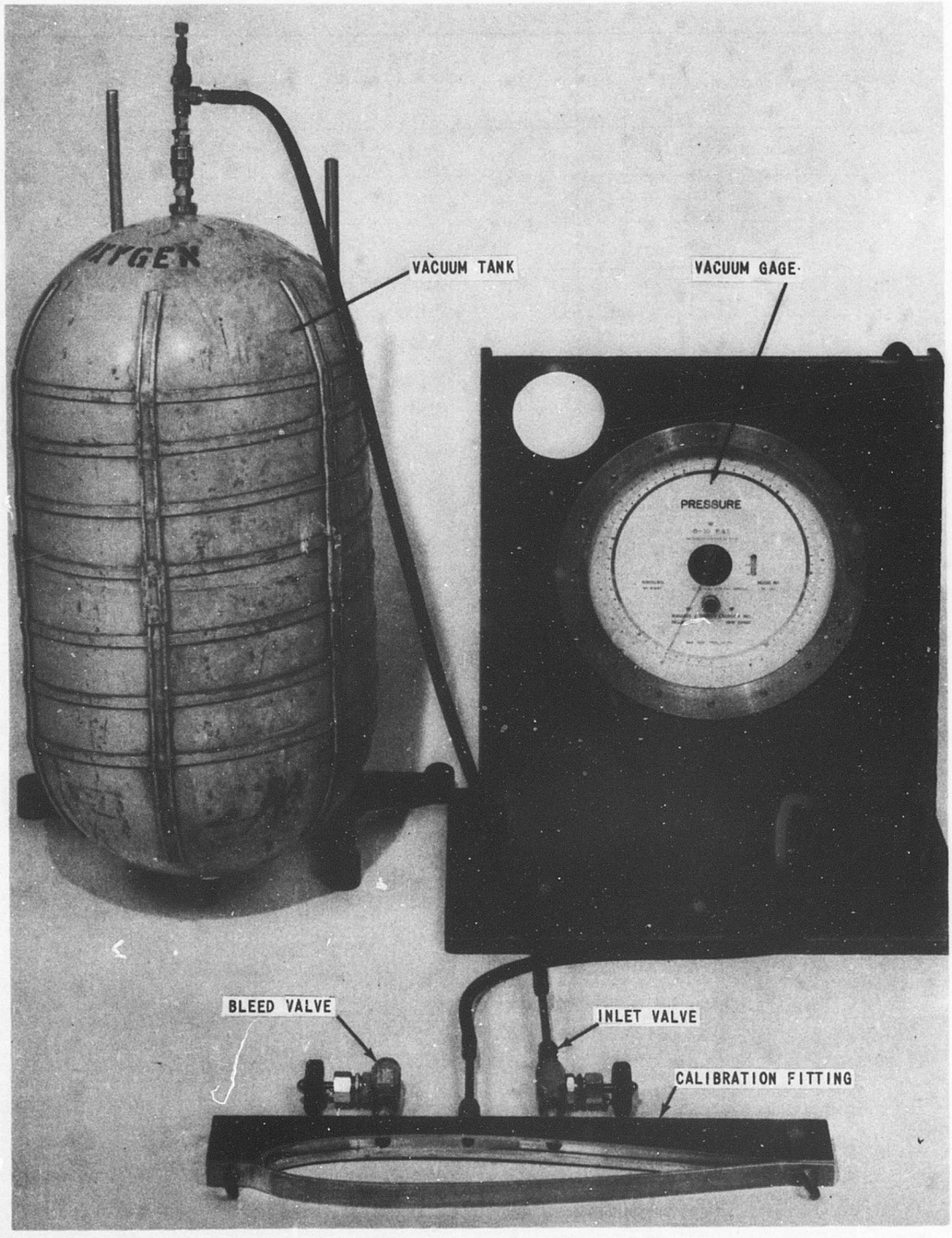

Figure 24. PRESSURE GAGE CALIBRATION EQUIPMENT

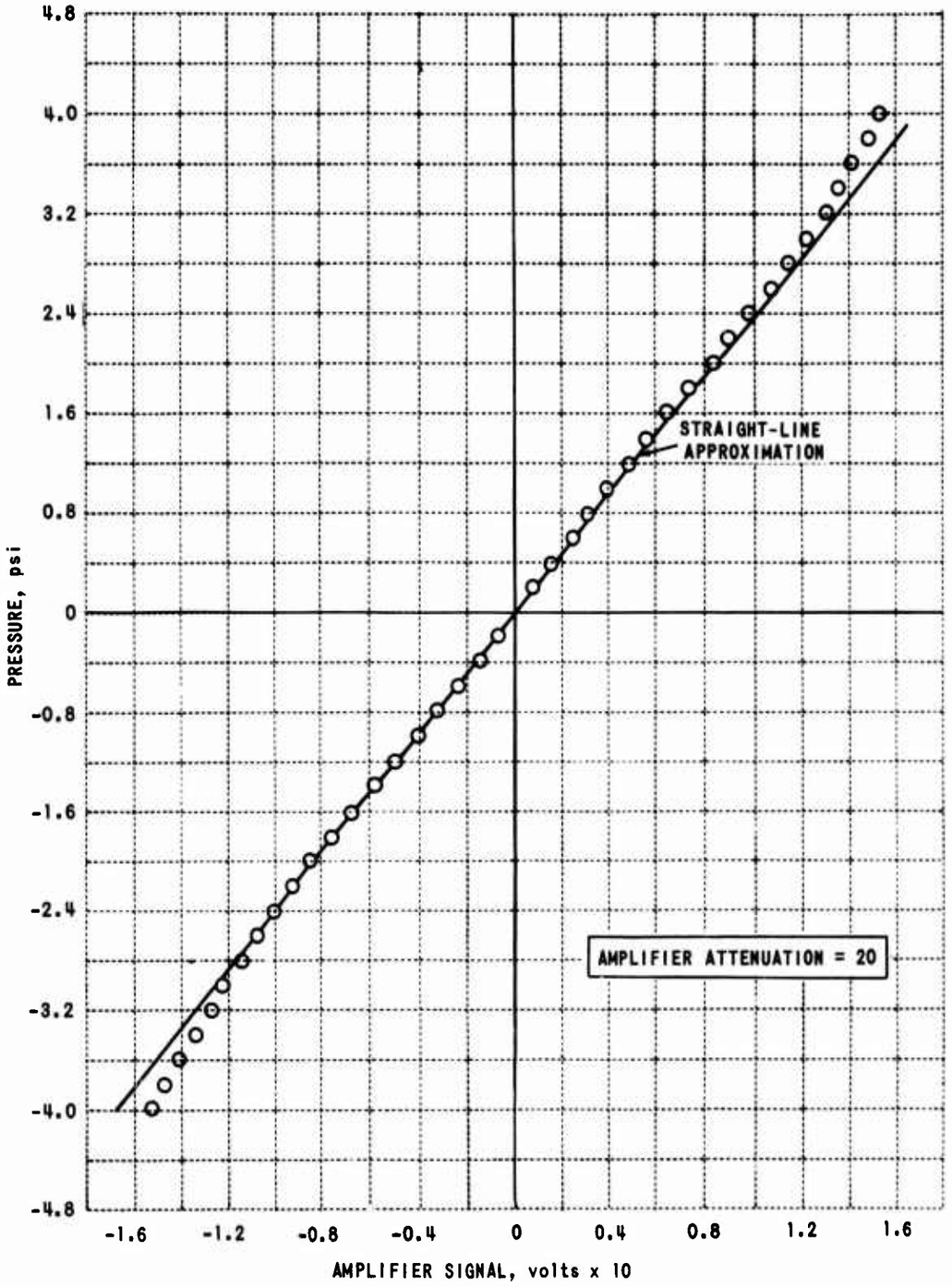

Figure 25. TYPICAL CALIBRATION CURVE FOR 1-PSI DIFFERENTIAL GAGE

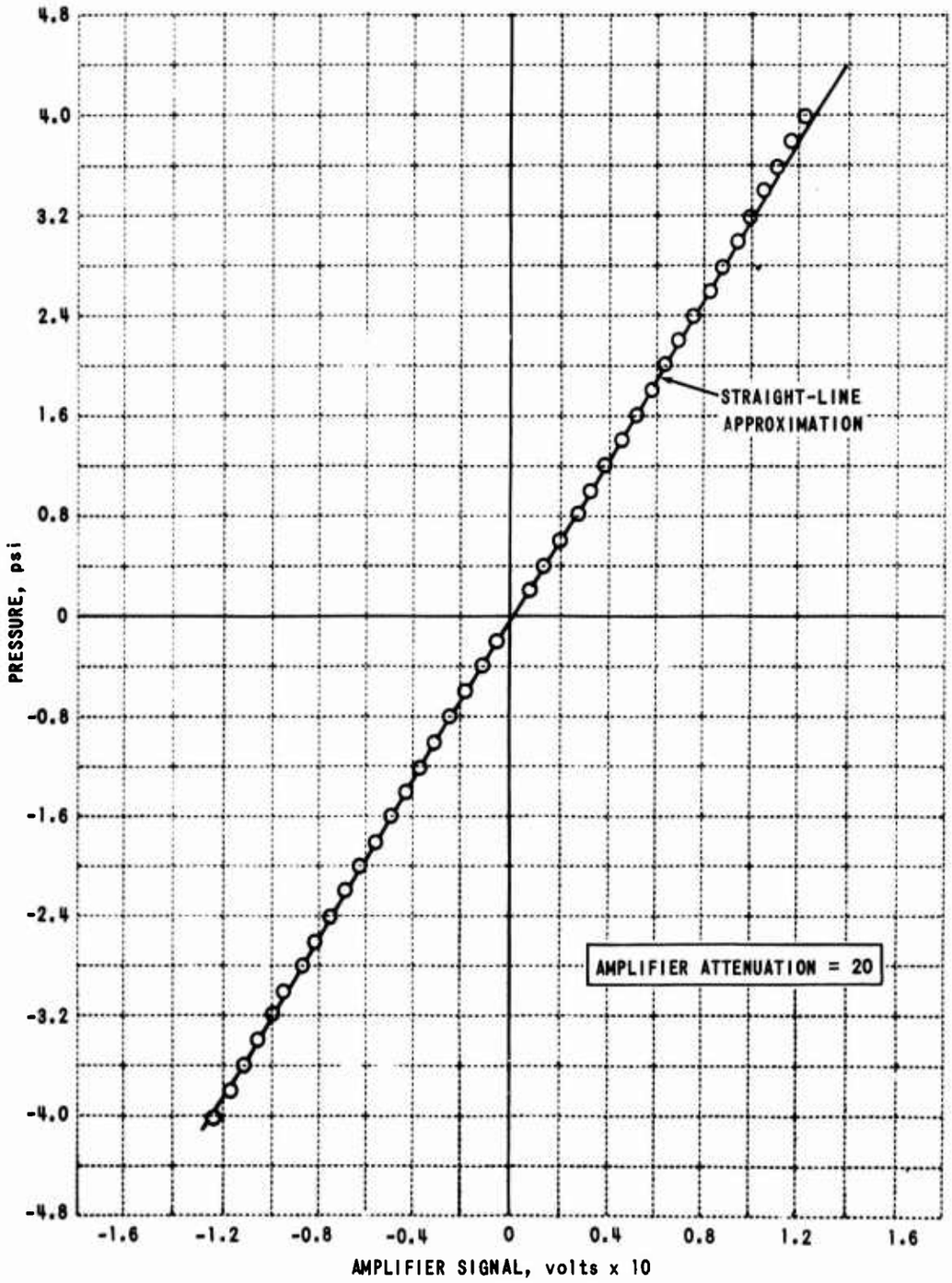

Figure 26. TYPICAL CALIBRATION CURVE FOR 2-PSI DIFFERENTIAL GAGE

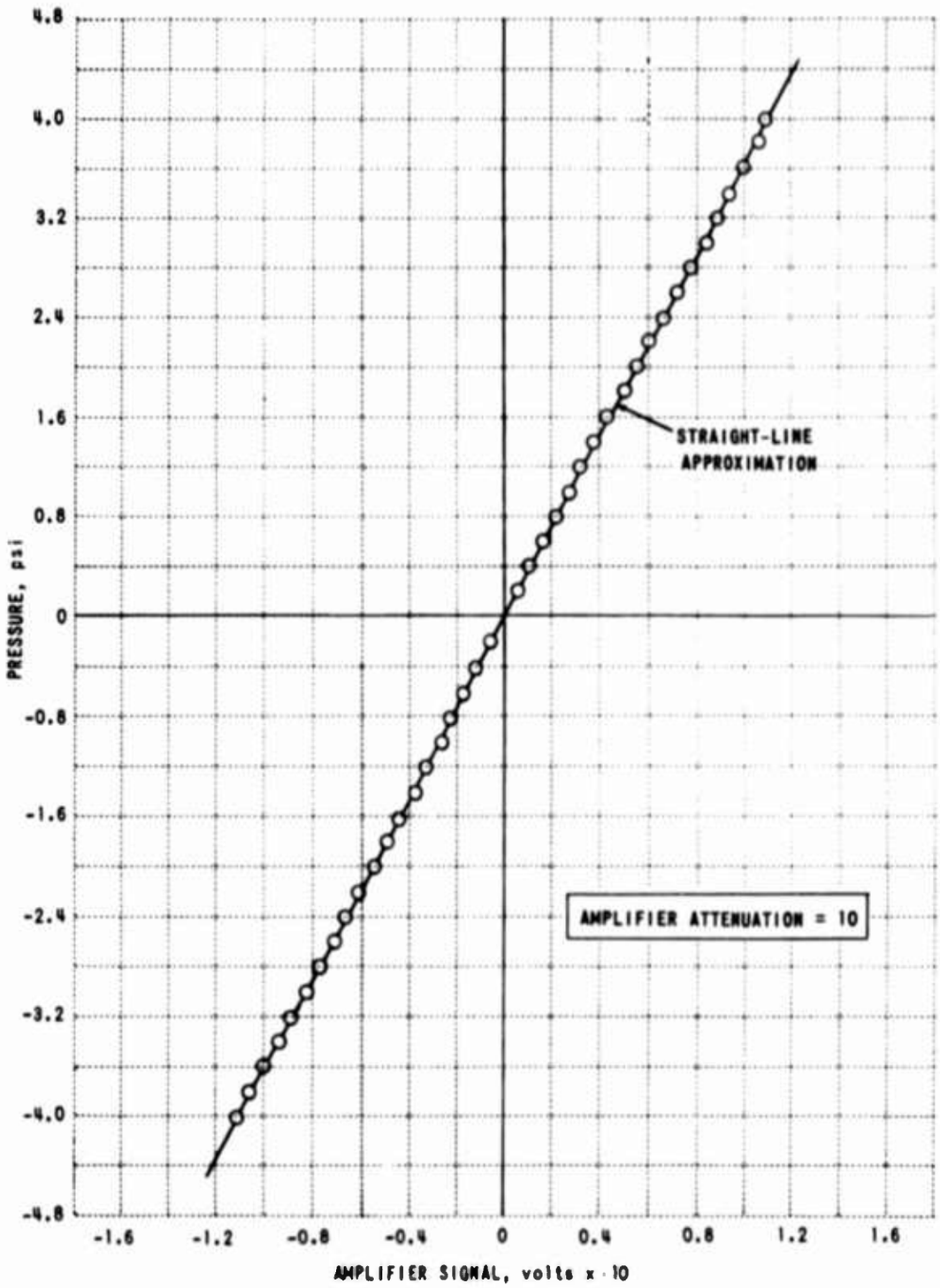

Figure 27. TYPICAL CALIBRATION CURVE FOR 4-PSI DIFFERENTIAL GAGE

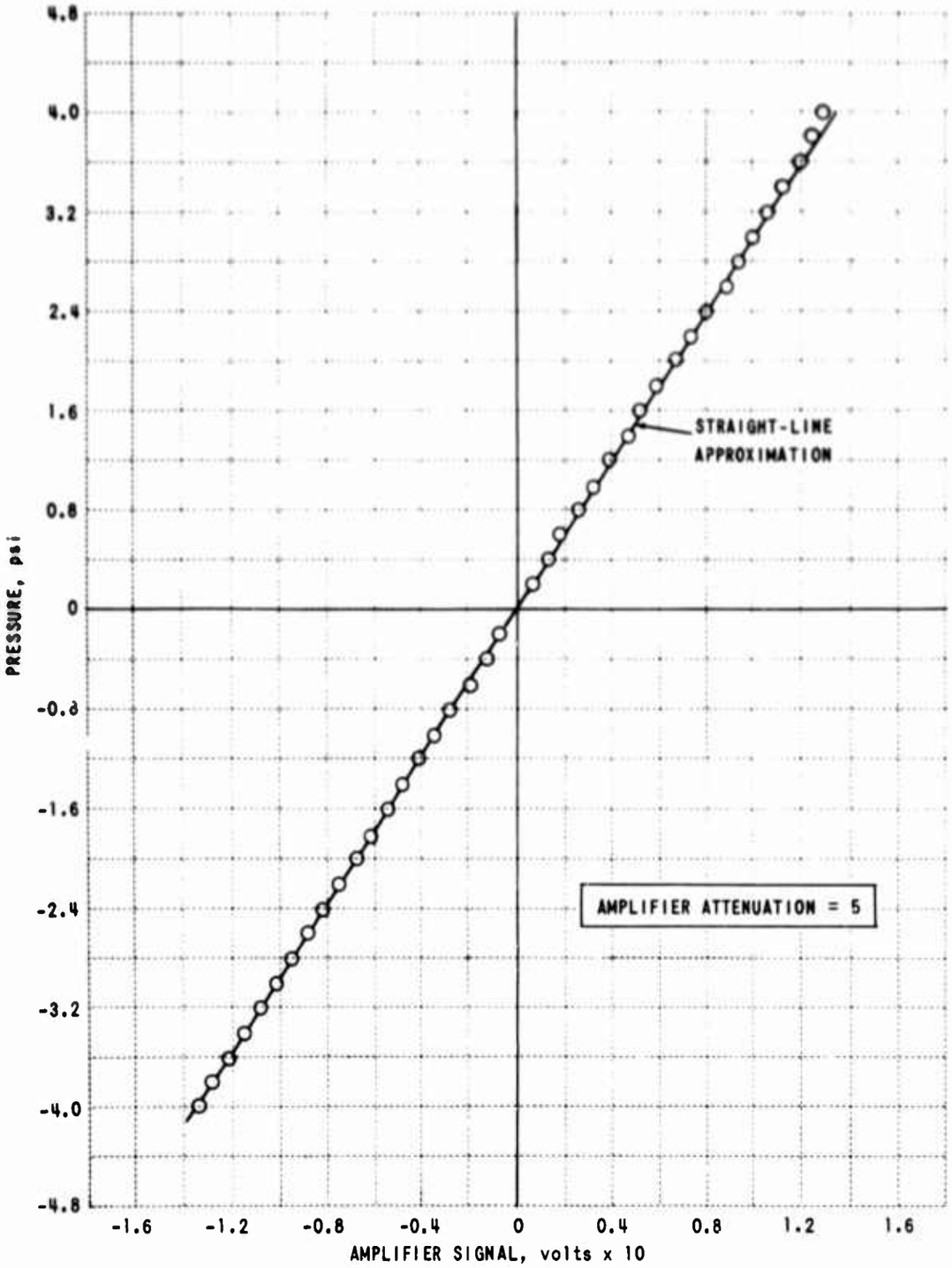

Figure 28. TYPICAL CALIBRATION CURVE FOR 8-PSI DIFFERENTIAL GAGE

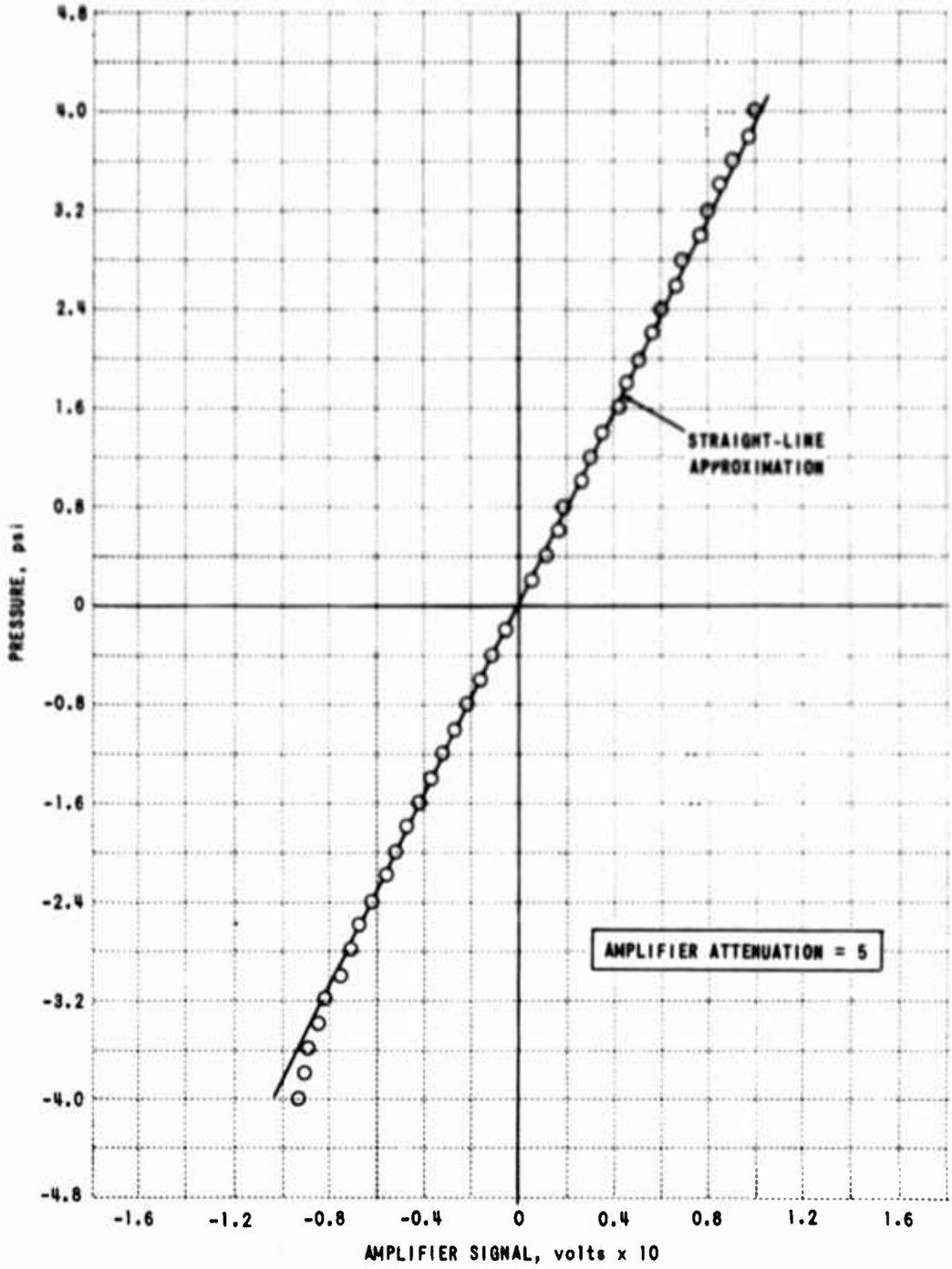

Figure 29. TYPICAL CALIBRATION CURVE FOR 15-PSI DIFFERENTIAL GAGE

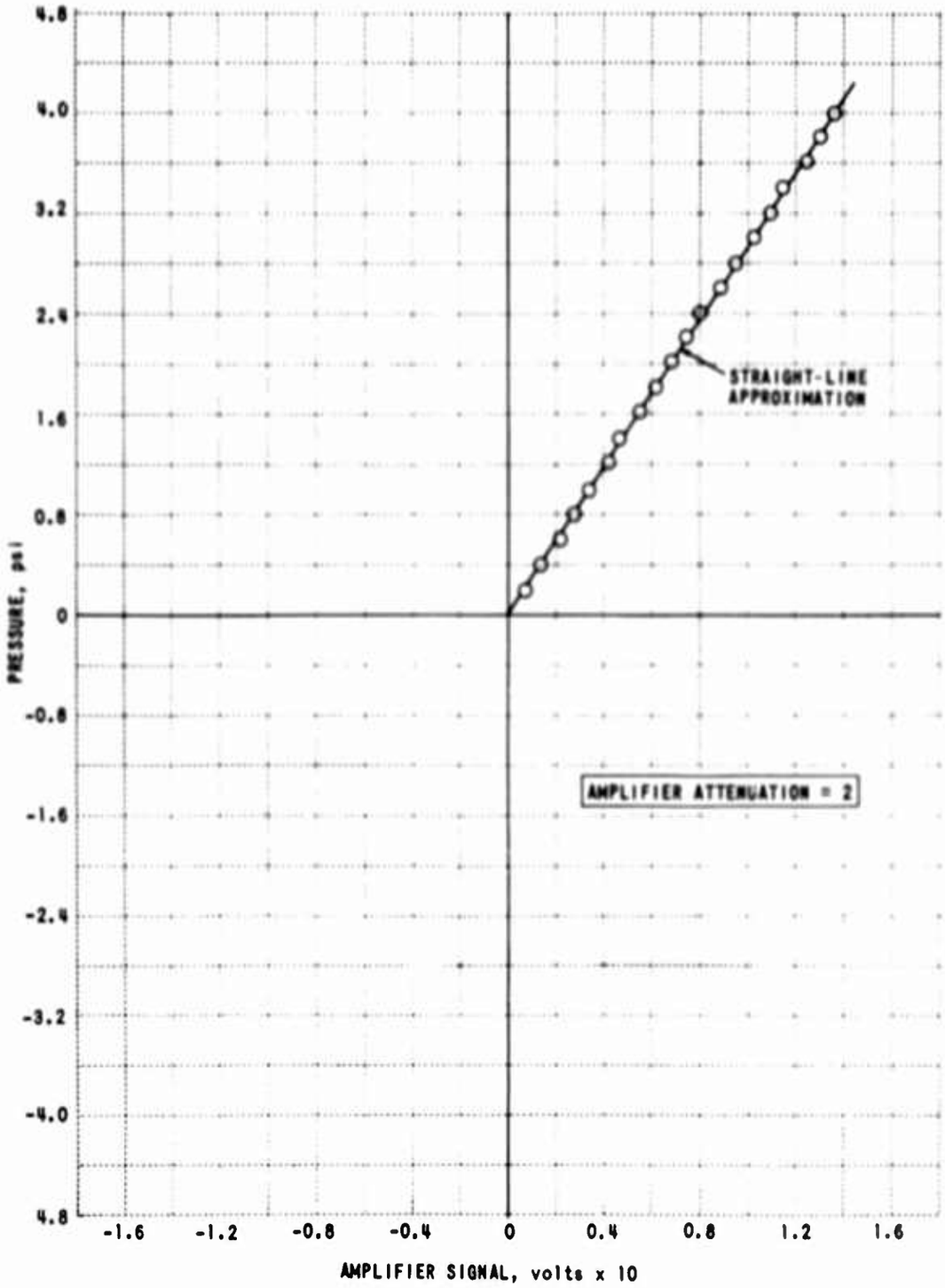

Figure 30. TYPICAL CALIBRATION CURVE FOR 5- TO 20-PSI ABSOLUTE GAGE

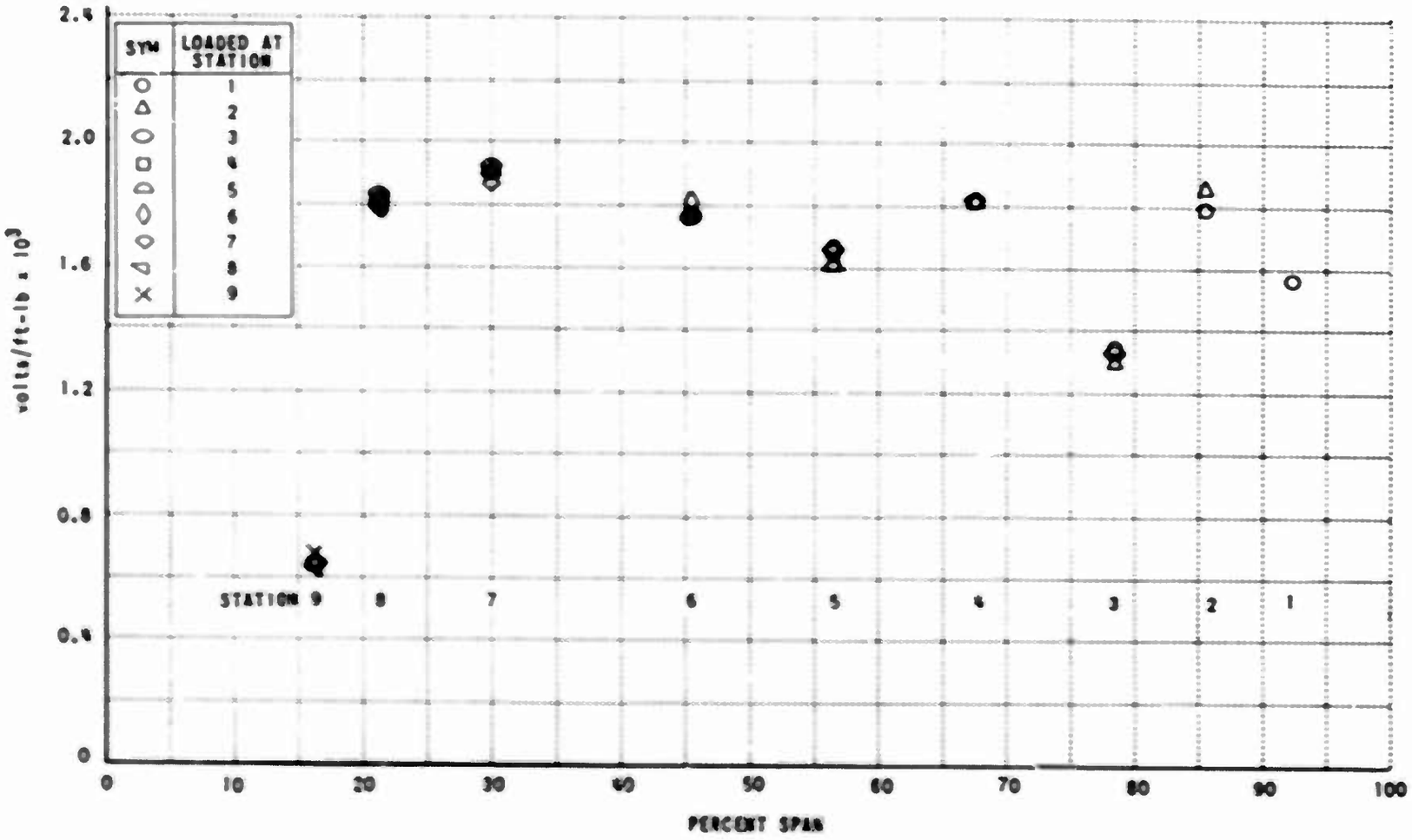

Figure 31. BEAMWISE STRAIN GAGE CALIBRATION CONSTANTS

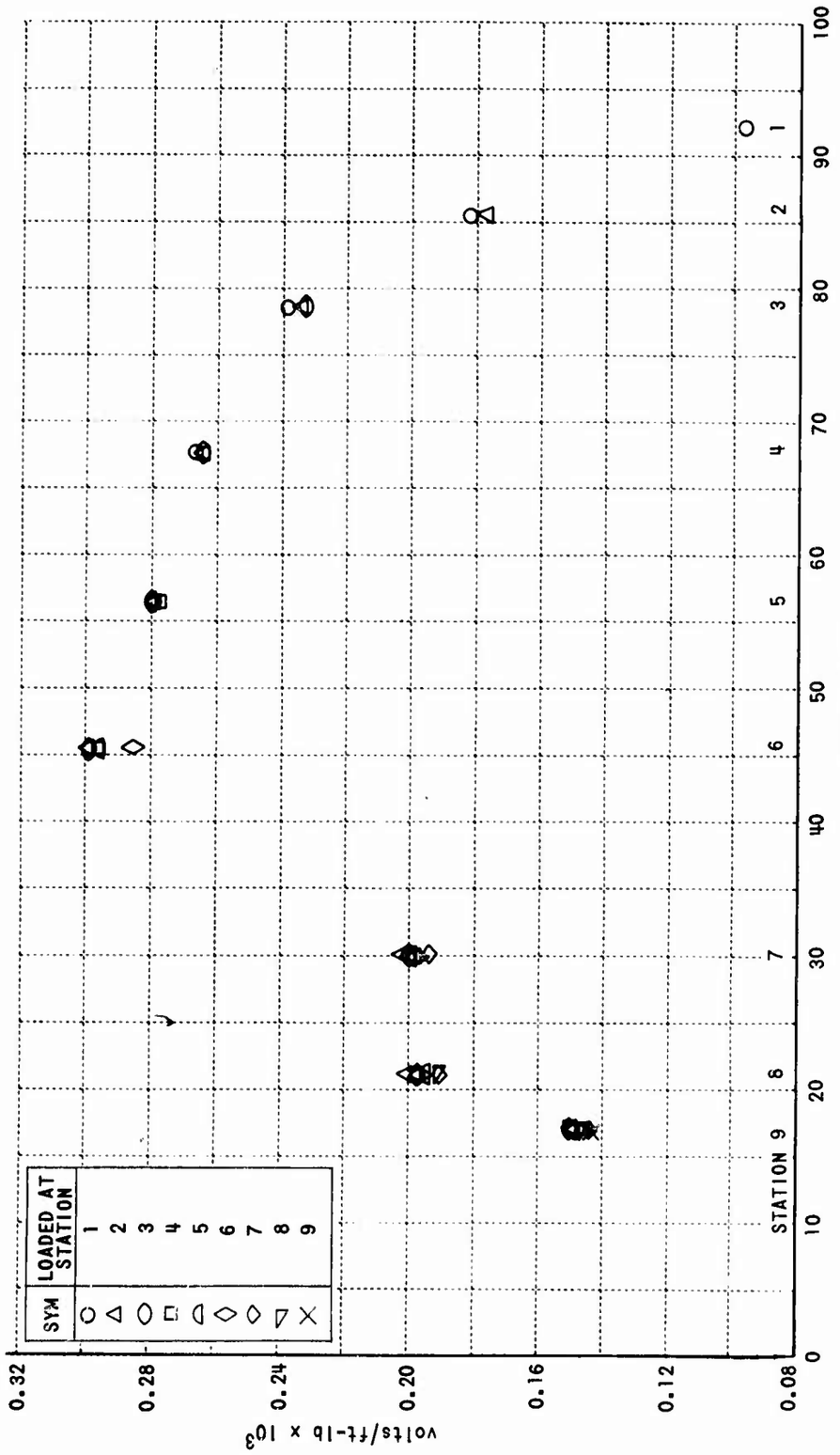

Figure 32. EDGEWISE STRAIN GAGE CALIBRATION CONSTANTS

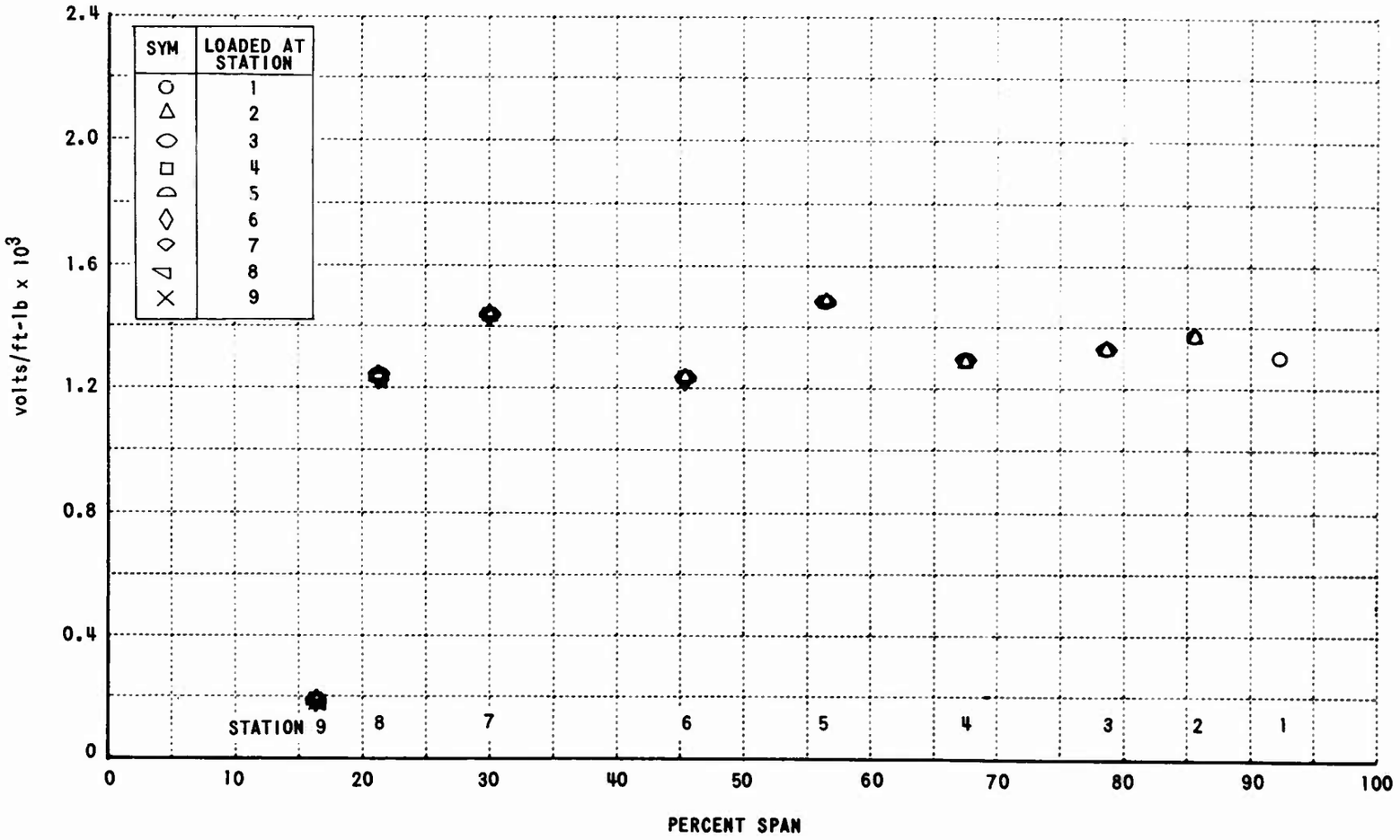

Figure 33. TORSIONAL STRAIN GAGE CALIBRATION CONSTANTS

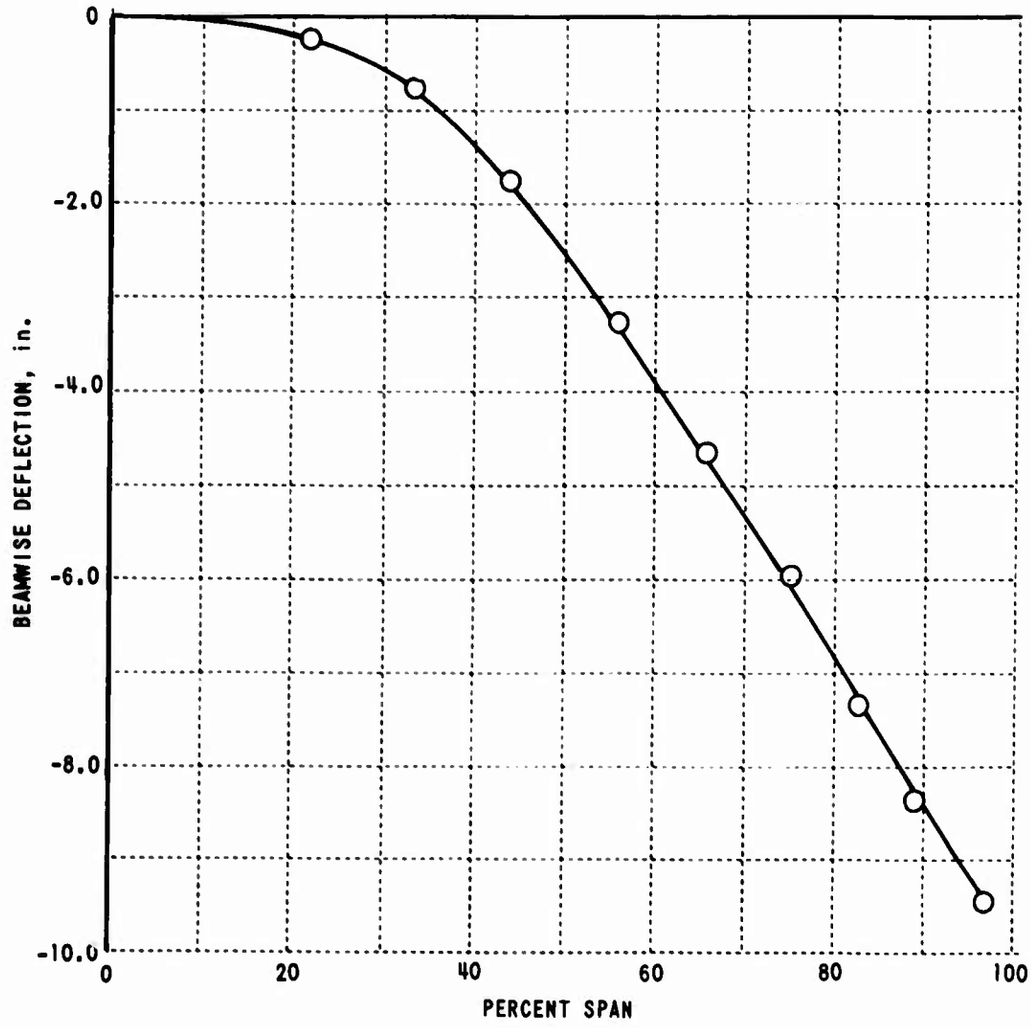

Figure 34. BLADE BEAMWISE DEFLECTION UNDER ITS OWN WEIGHT

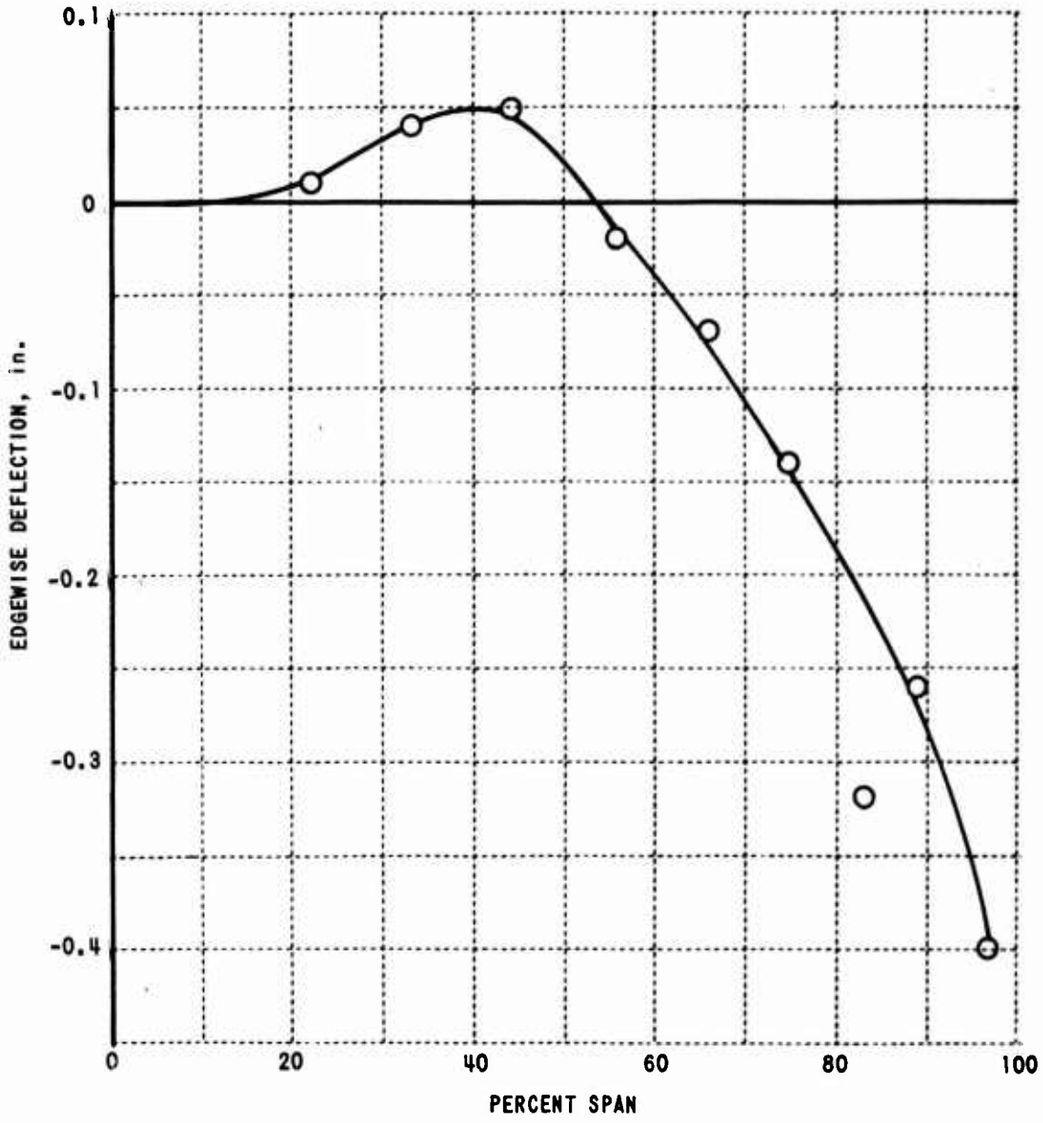

Figure 35. BLADE EDGEWISE DEFLECTION UNDER ITS OWN WEIGHT

Figure 36. TEST OPERATOR'S STATION IN WIND TUNNEL CONTROL ROOM

--RUN NO. 4-- --POINT NO. 4--

DYN. PRESS. = 28.95
AZIMUTH = 90.5
SHAFT TILT = 5.47
ROOT PITCH = 10.29
RUN 4 POINT 4

BLADE PRESSURE DISTRIBUTIONS (LB/IN.SQ)

CHORDWISE LOCATIONS PERCENT CHORD	SPANWISE LOCATIONS PERCENT SPAN					
	41.1	55.7	75.4	85.2	90.1	95.0
2.1		0.970	0.818	0.618	0.600	0.385
3.7	1.120			0.566		
9.0		0.708	0.467	0.470	0.385	0.264
12.9				0.302		
16.9	0.536	0.399		0.467	0.233	0.201
22.6		0.311		0.183	0.096	
33.5	0.220					
47.8				0.094		
62.0	0.110	0.093	0.094	0.043	0.055	
68.9 TS				-0.174		
LS				0.029		
75.4				-0.184		
82.0 TS				0.045		
85.9	0.059					
88.0		0.048	0.013	-0.159	0.023	0.018
94.1 TS				-0.270		
LS				-0.238		
97.0 TS				-0.257		
LS				-0.047		

BLADE STRUCTURAL MOMENT DISTRIBUTIONS (FT-LB)

PERCENT SPAN	FLATWISE	CHORDWISE	TORSION
16.6	4.368E 03	-1.635E 03	
29.4	3.382E 03	-3.125E 02	2.054E 01
37.3	2.643E 03	-4.040E 02	4.847E 01
51.1	1.820E 03	-3.040E 02	3.899E 01
61.0	7.964E 02	-6.702E 01	4.294E 01
70.8	4.077E 02	9.925E 01	1.339E 01
80.7	1.978E 02	8.178E 00	1.067E 01
86.9	6.010E 01		8.224E 00
93.0	1.360E 01		1.742E 00

BALANCE DATA

PMR(FT-LB)	NFR(LB)	BMR(FT-LB)	EMR(FT-LB)	EFR(LB)
7.882E 01	8.454E 02	7.648E 03	-1.602E 03	-1.972E 02

Figure 37. TYPICAL PRINTOUT FOR EACH DATA POINT

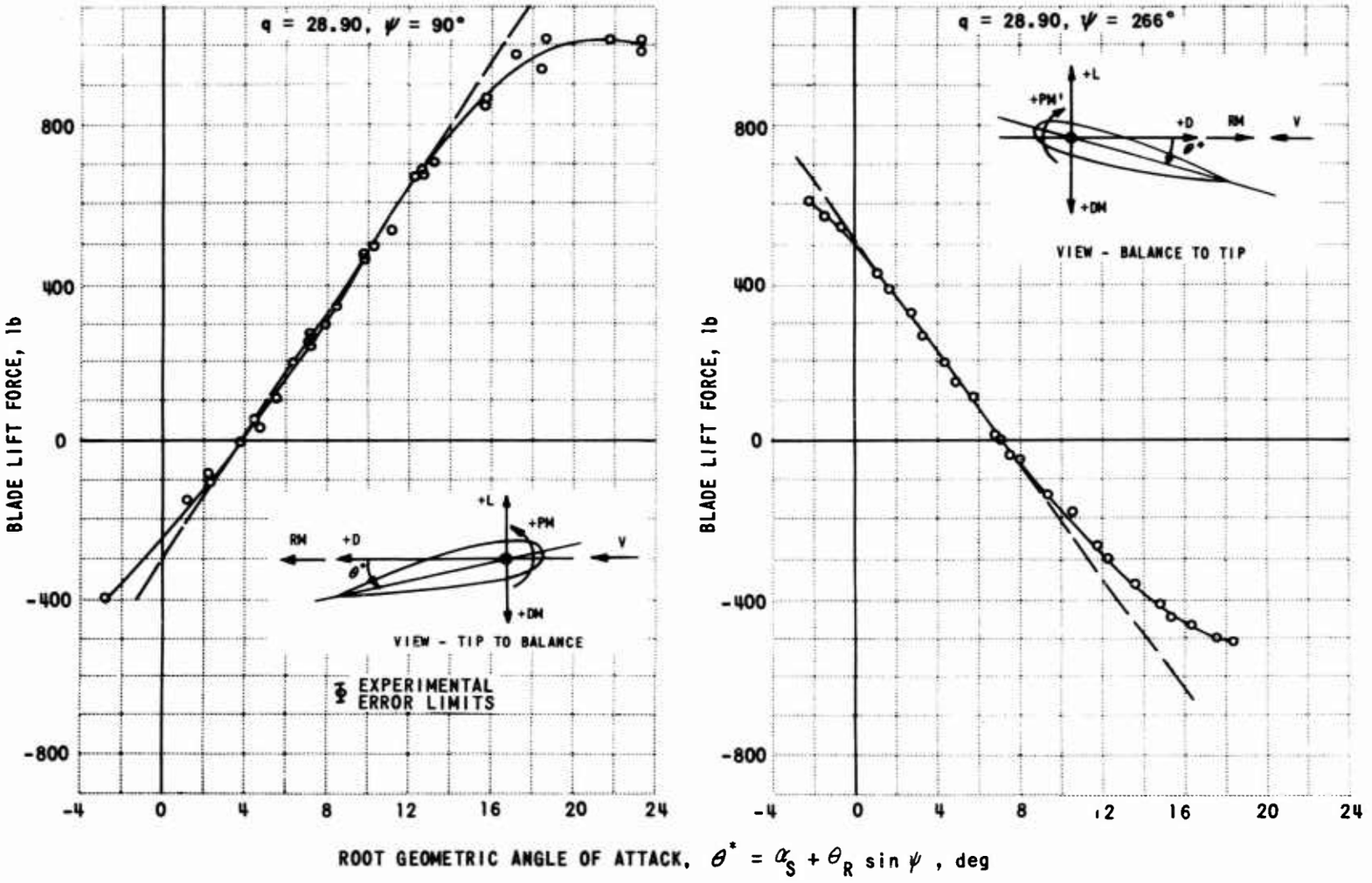

Figure 38. BLADE LIFT VS ROOT GEOMETRIC ANGLE OF ATTACK AT ψ = 90 AND 266 DEGREES

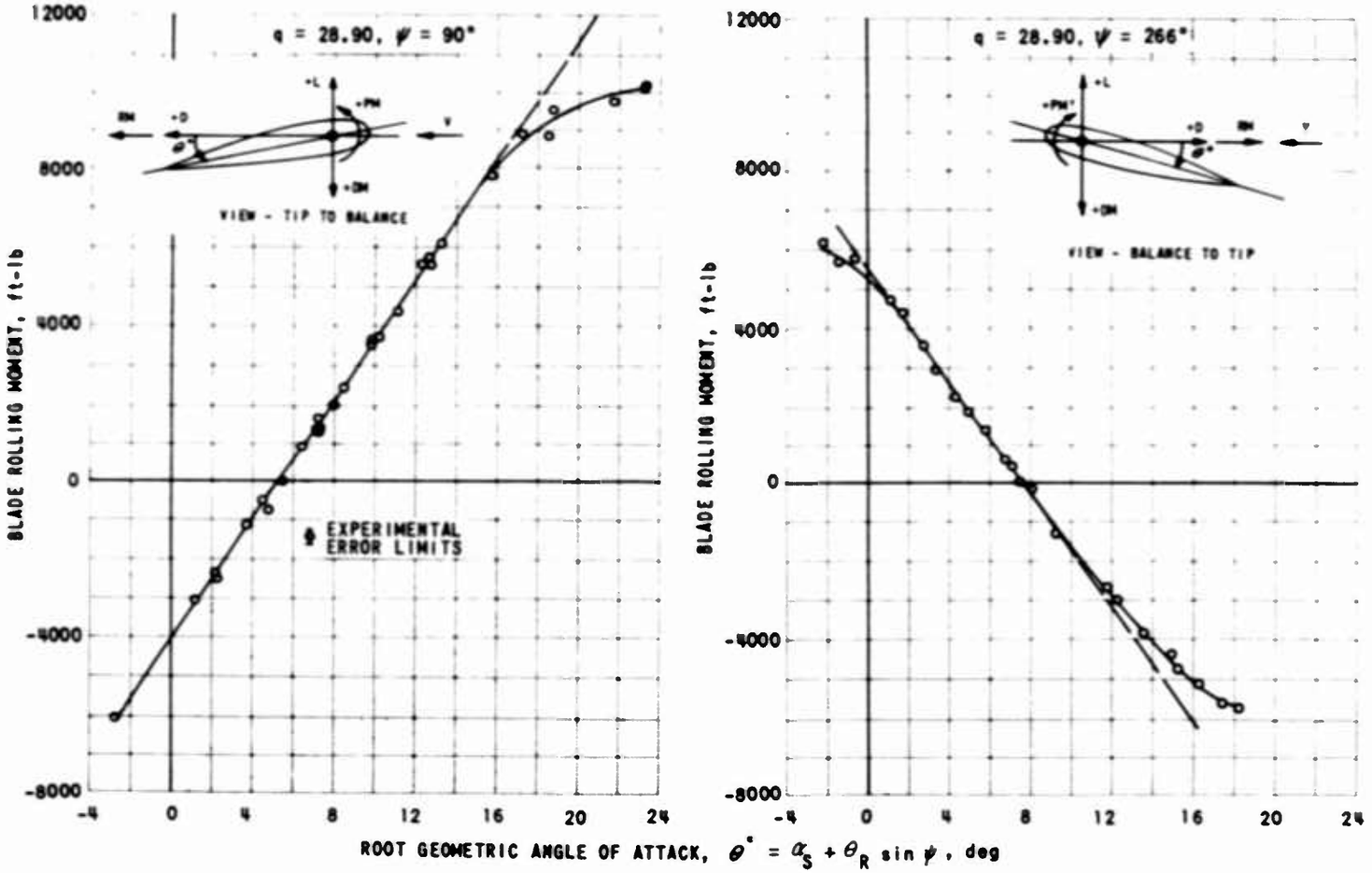

Figure 39. BLADE ROLLING MOMENT VS ROOT GEOMETRIC ANGLE OF ATTACK VS ψ = 90 AND 266 DEGREES

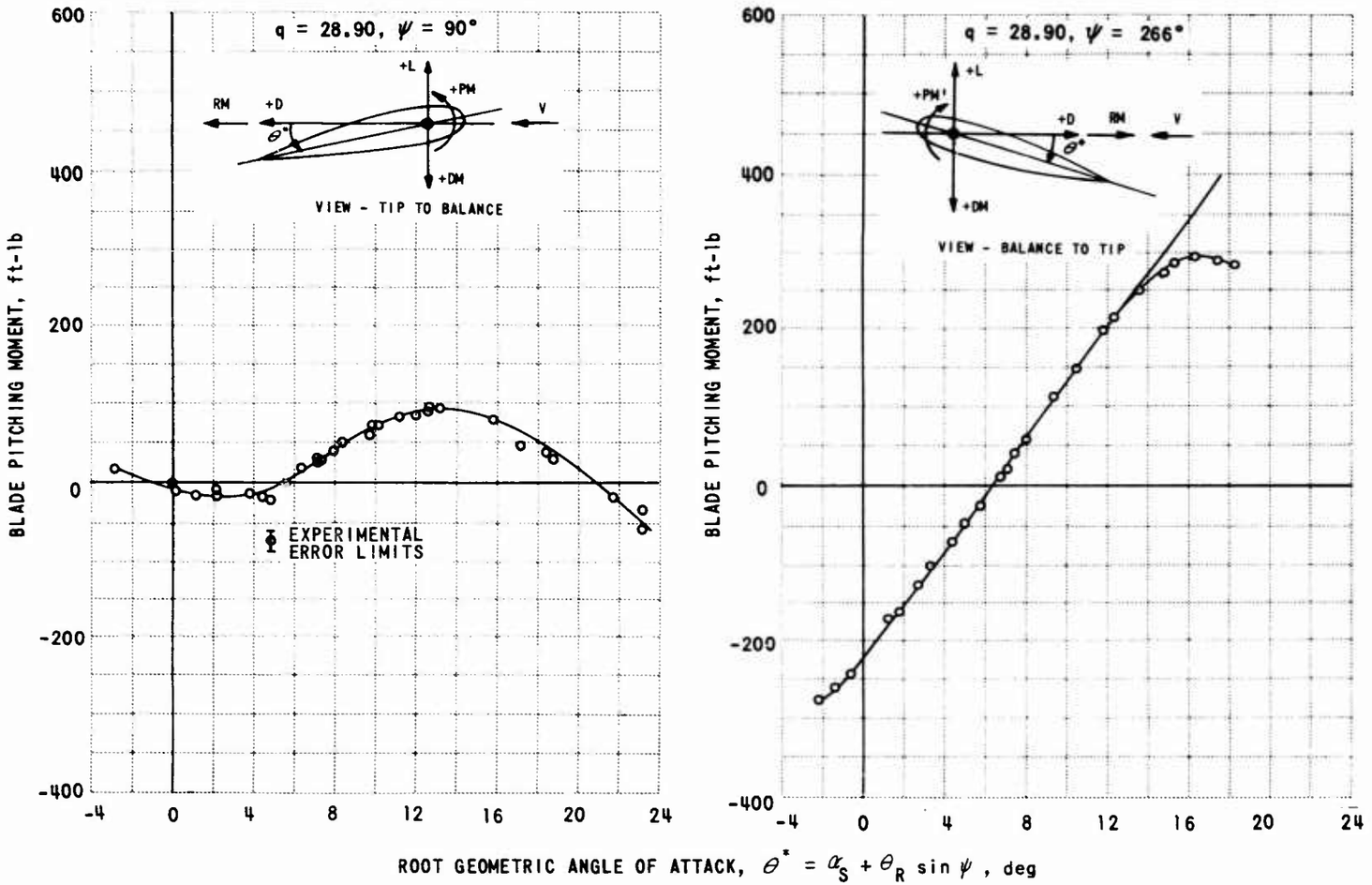

Figure 40. BLADE PITCHING MOMENT VS ROOT GEOMETRIC ANGLE OF ATTACK FOR ψ = 90 AND 266 DEGREES

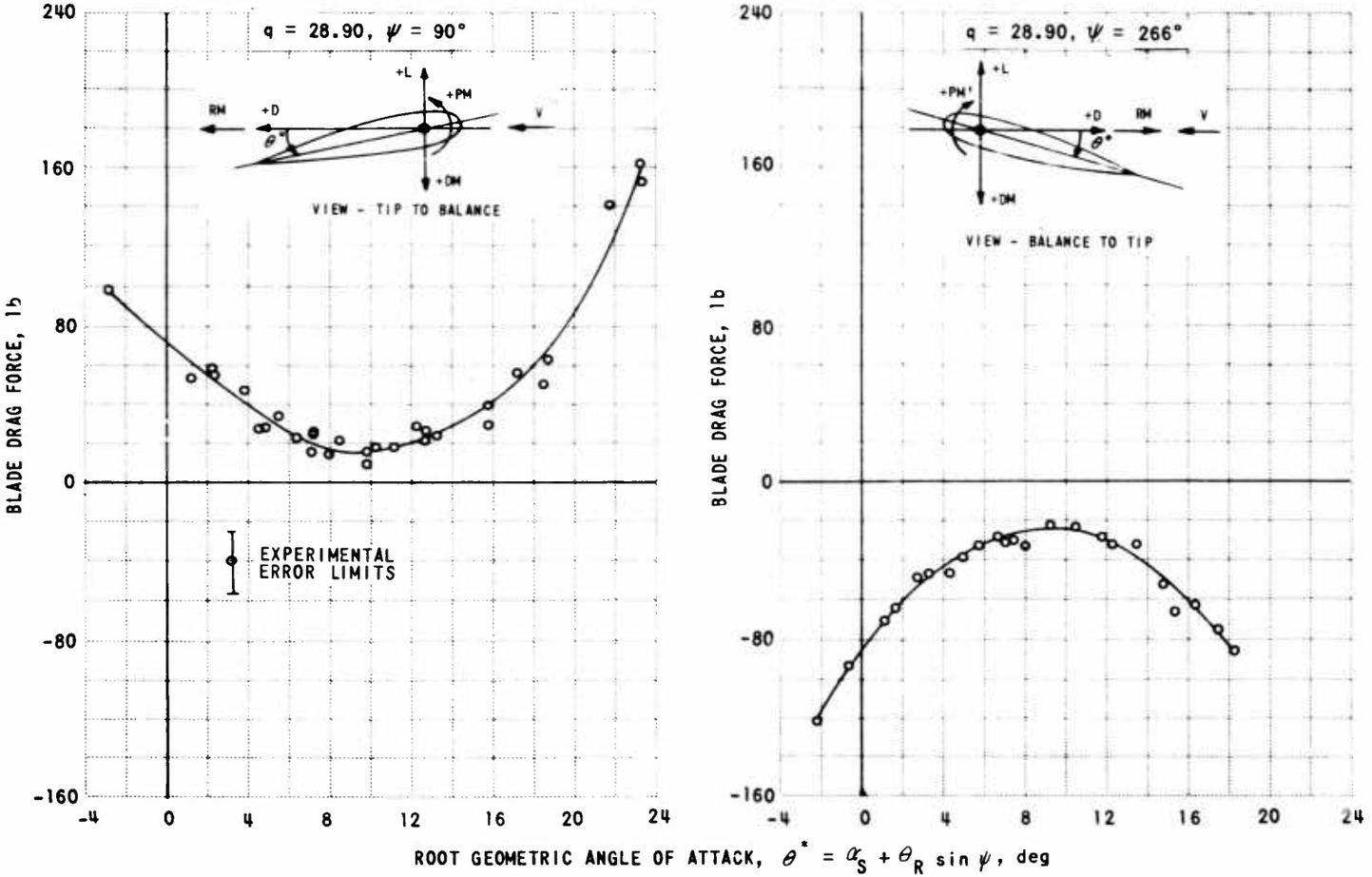

Figure 41. BLADE DRAG FORCE VS ROOT GEOMETRIC ANGLE OF ATTACK FOR ψ = 90 AND 266 DEGREES

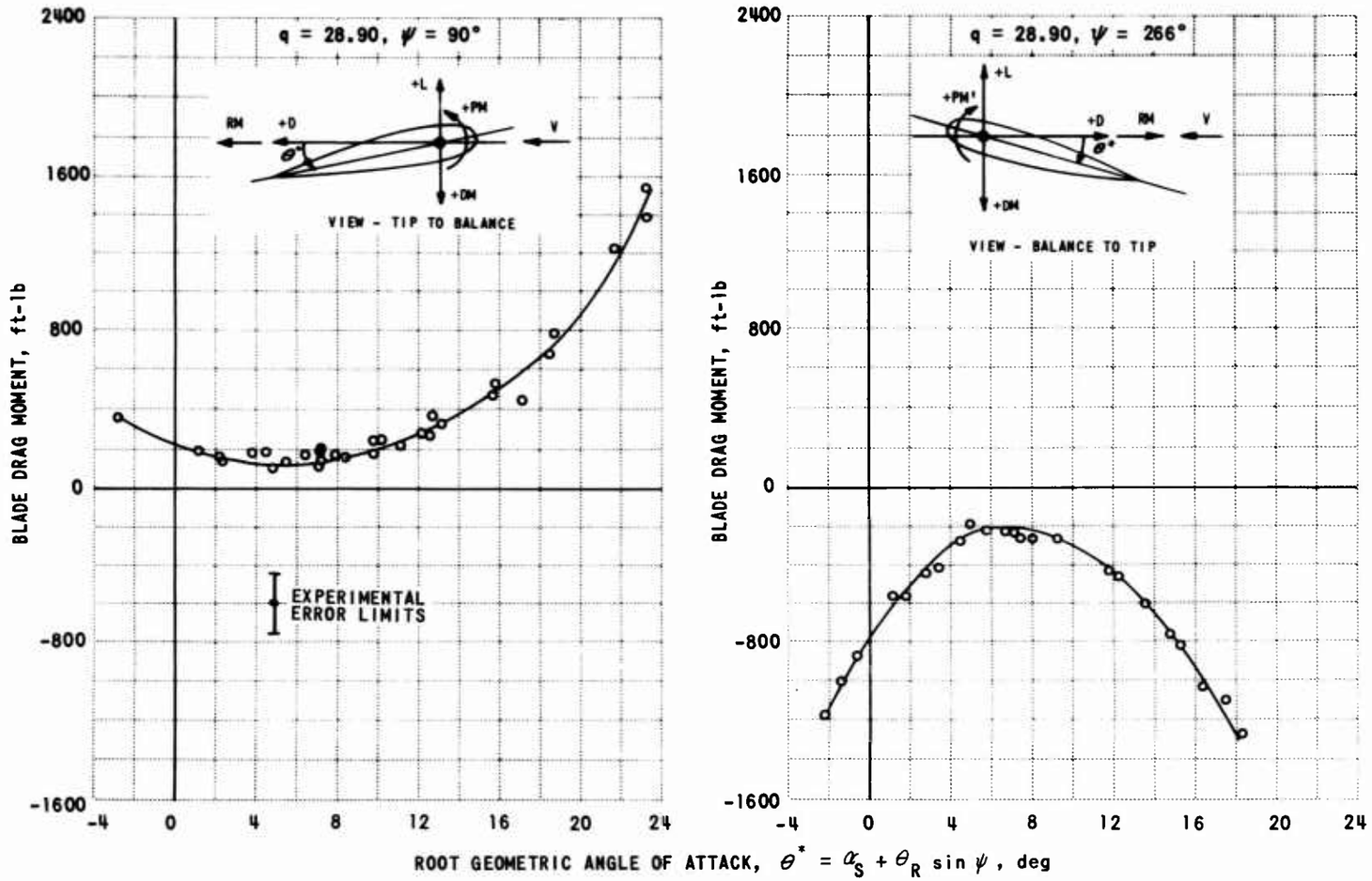

Figure 42. BLADE DRAG MOMENT VS ROOT GEOMETRIC ANGLE OF ATTACK FOR ψ = 90 AND 266 DEGREES

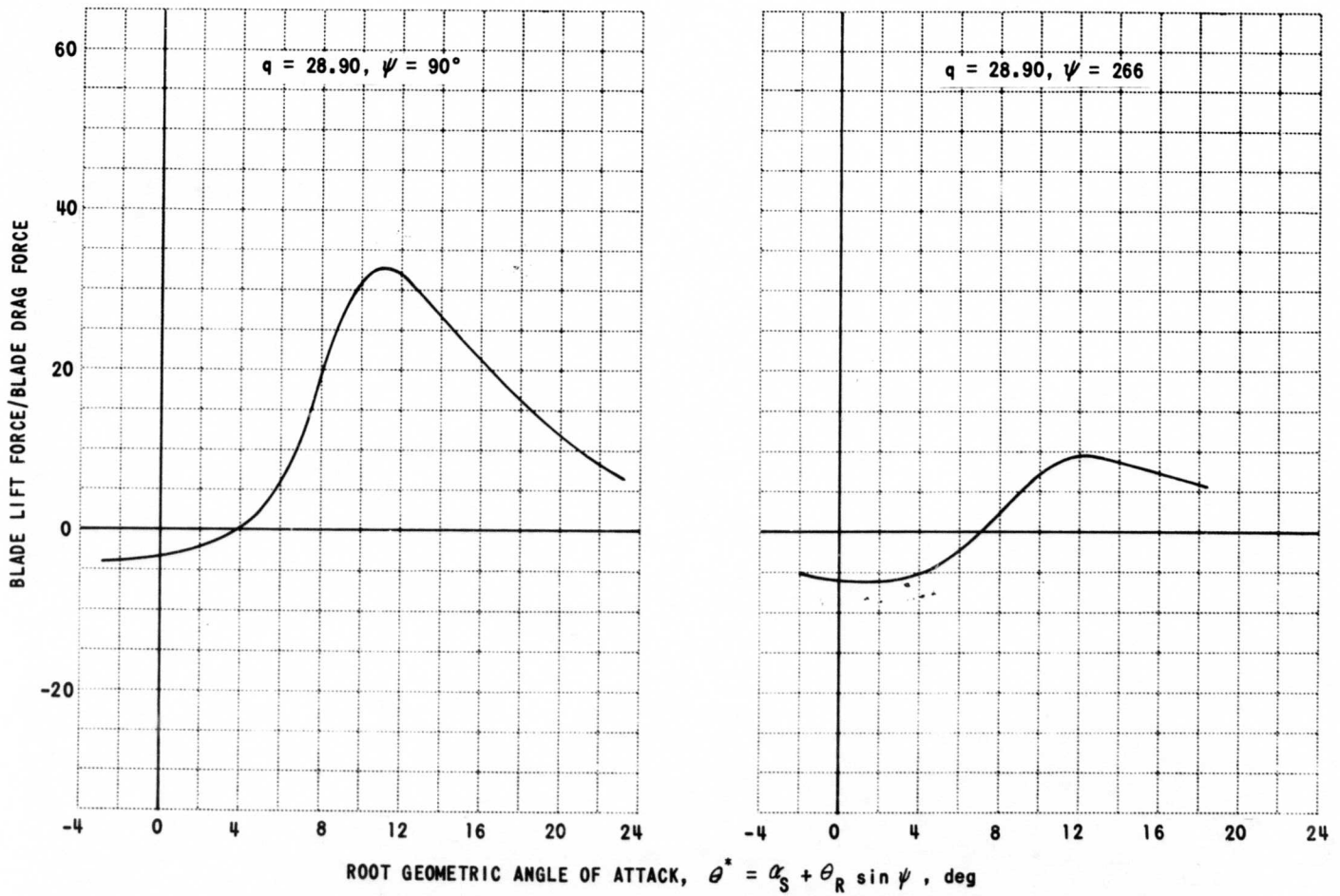

Figure 43. BLADE LIFT FORCE/BLADE DRAG FORCE VS ROOT GEOMETRIC ANGLE OF ATTACK FOR ψ = 90 AND 266 DEGREES

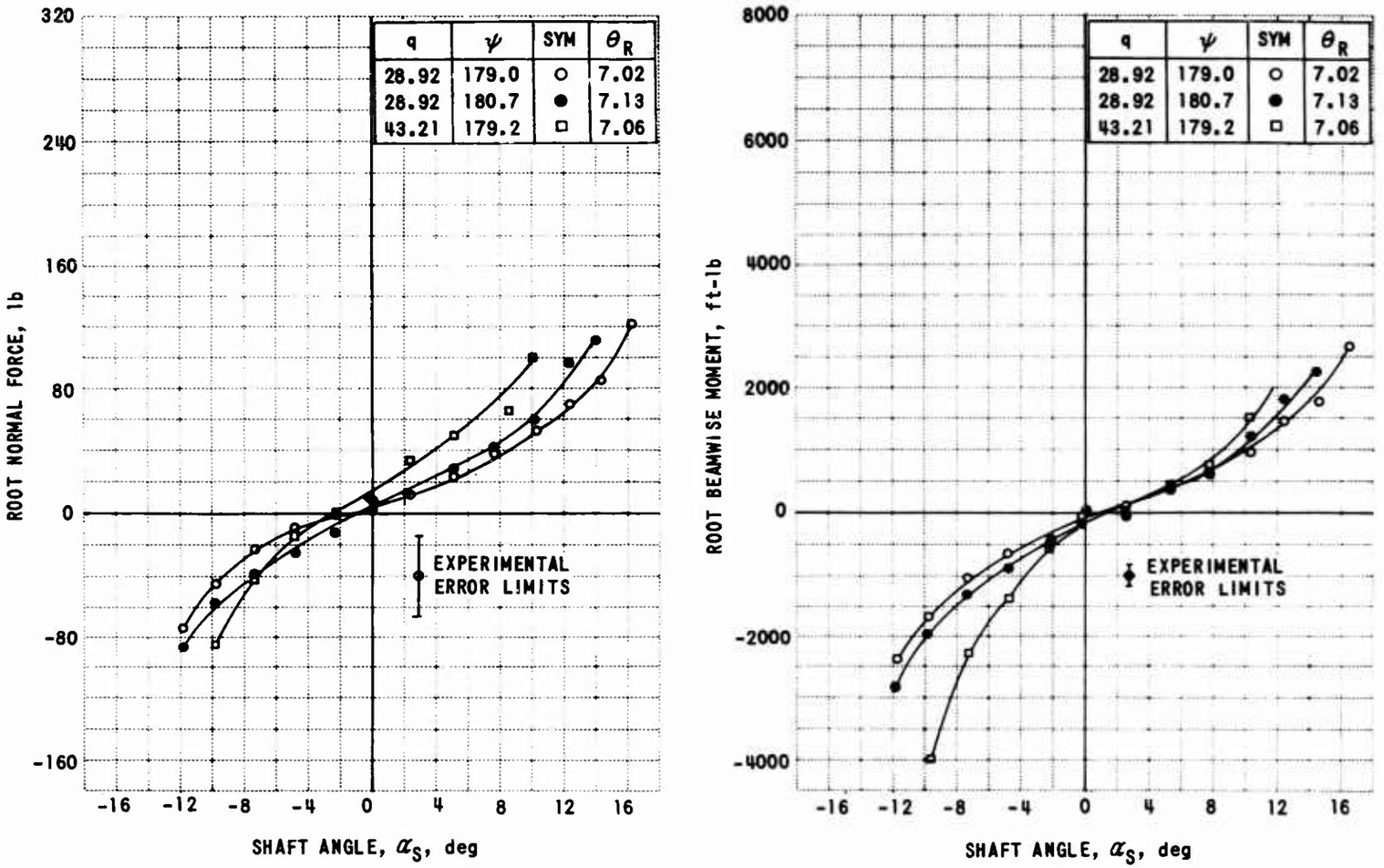

Figure 44. ROOT NORMAL FORCE AND BEAMWISE MOMENT VS SHAFT ANGLE FOR ψ = 180 DEGREES

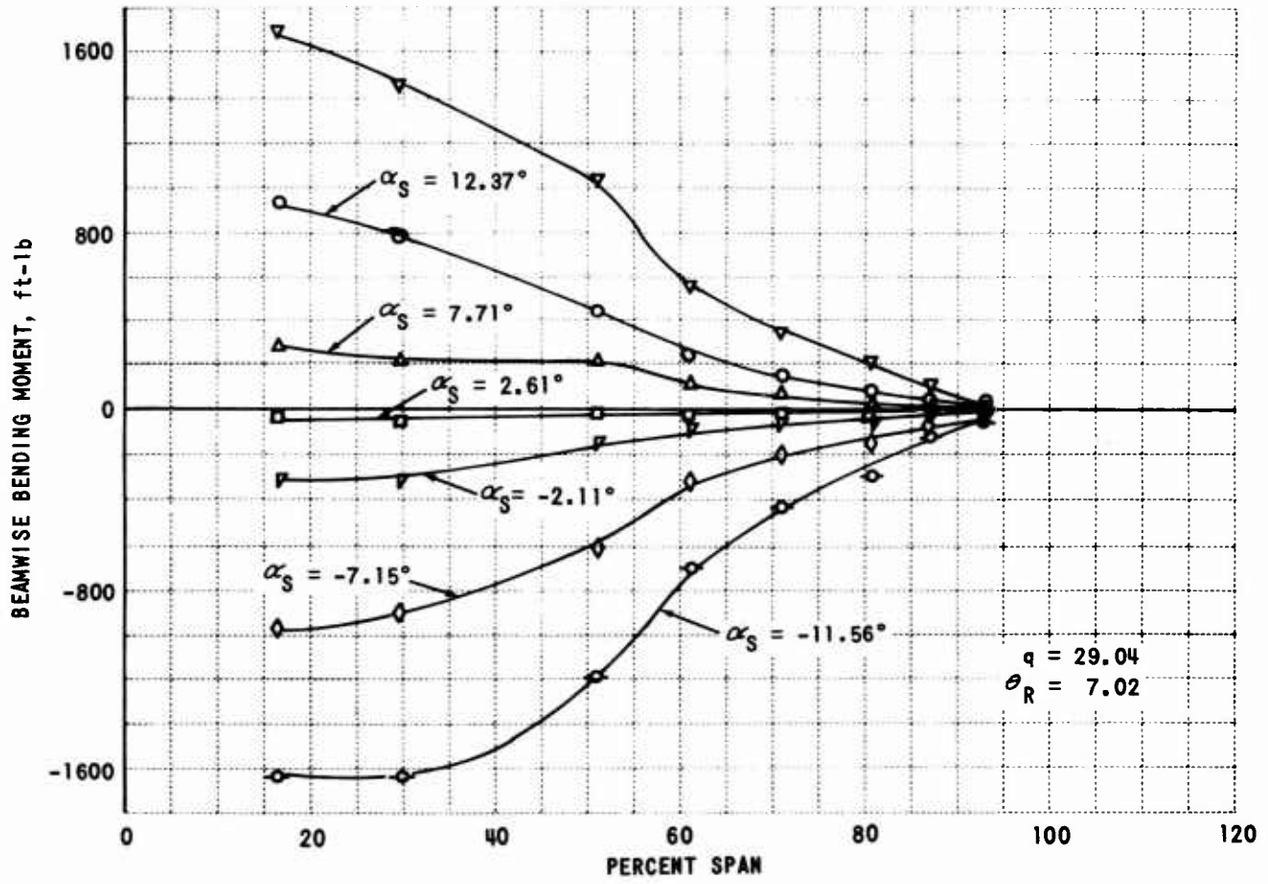

Figure 45. BENDING MOMENT DISTRIBUTIONS AT ψ = 180 DEGREES FOR VARIOUS SHAFT ANGLES

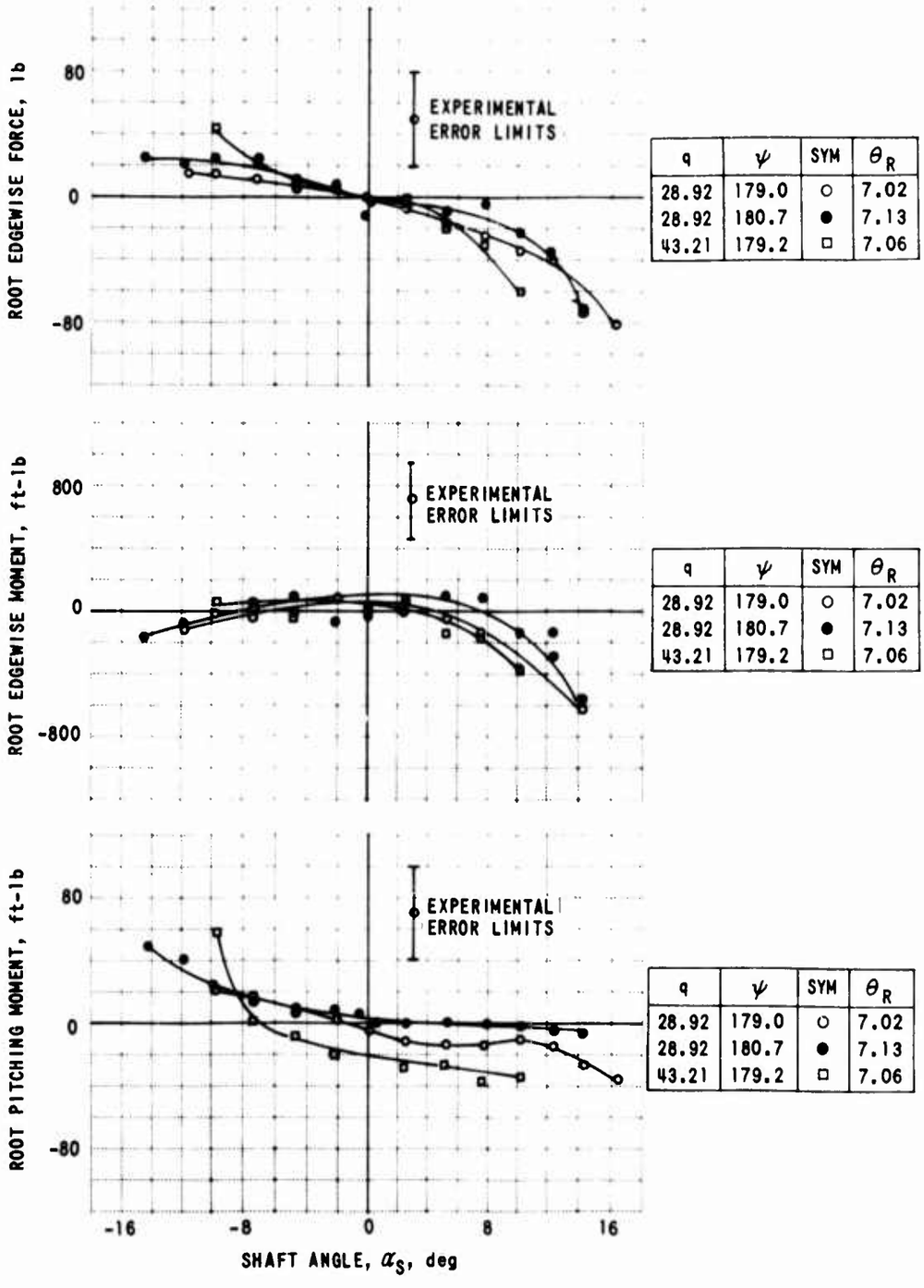

Figure 46. ROOT EDGEWISE FORCE, EDGEWISE MOMENT, AND PITCHING MOMENT VS SHAFT ANGLE FOR ψ = 180 DEGREES

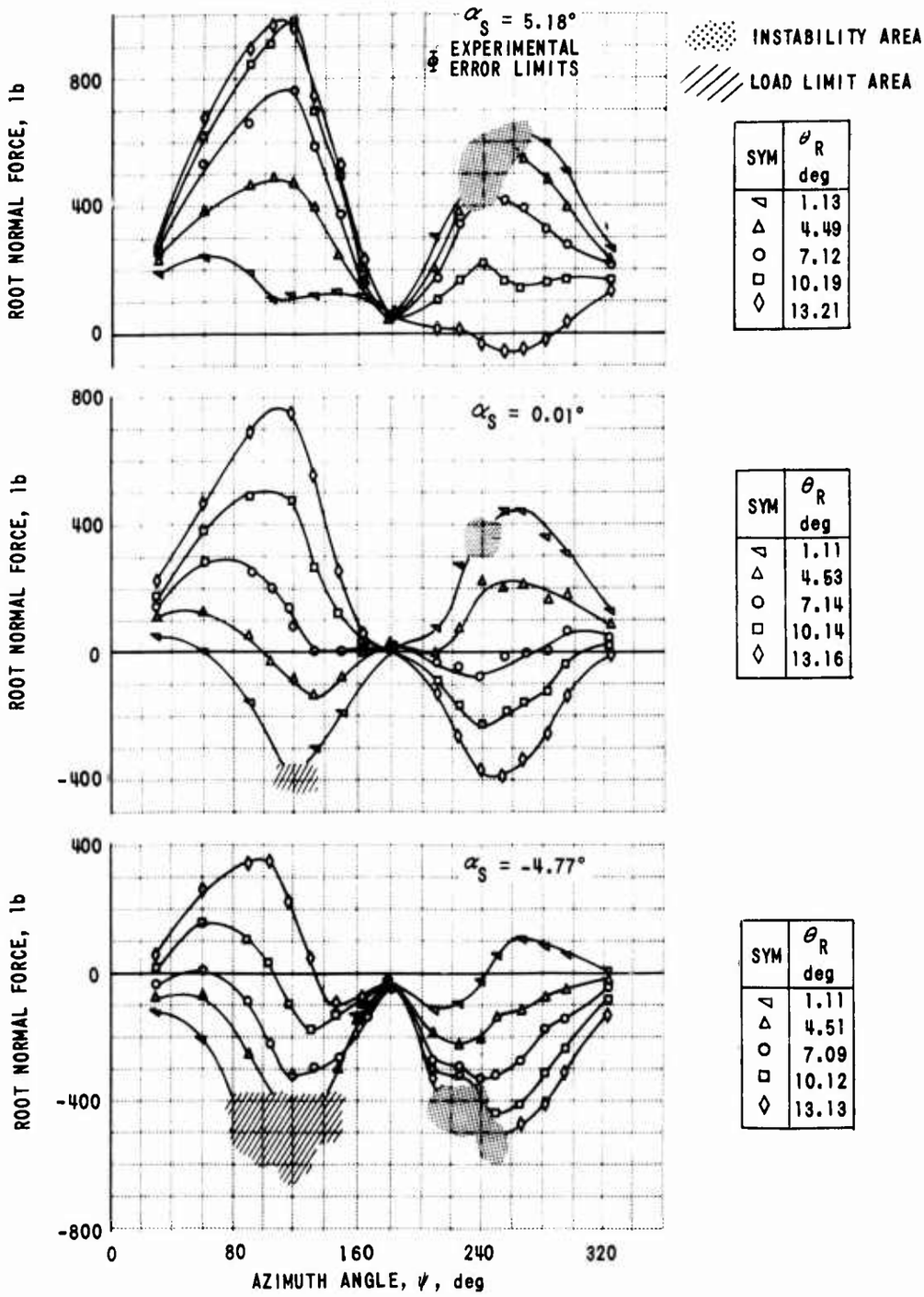

Figure 47. ROOT NORMAL FORCE VS AZIMUTH ANGLE FOR VARIOUS SHAFT ANGLES AT q = 28.93

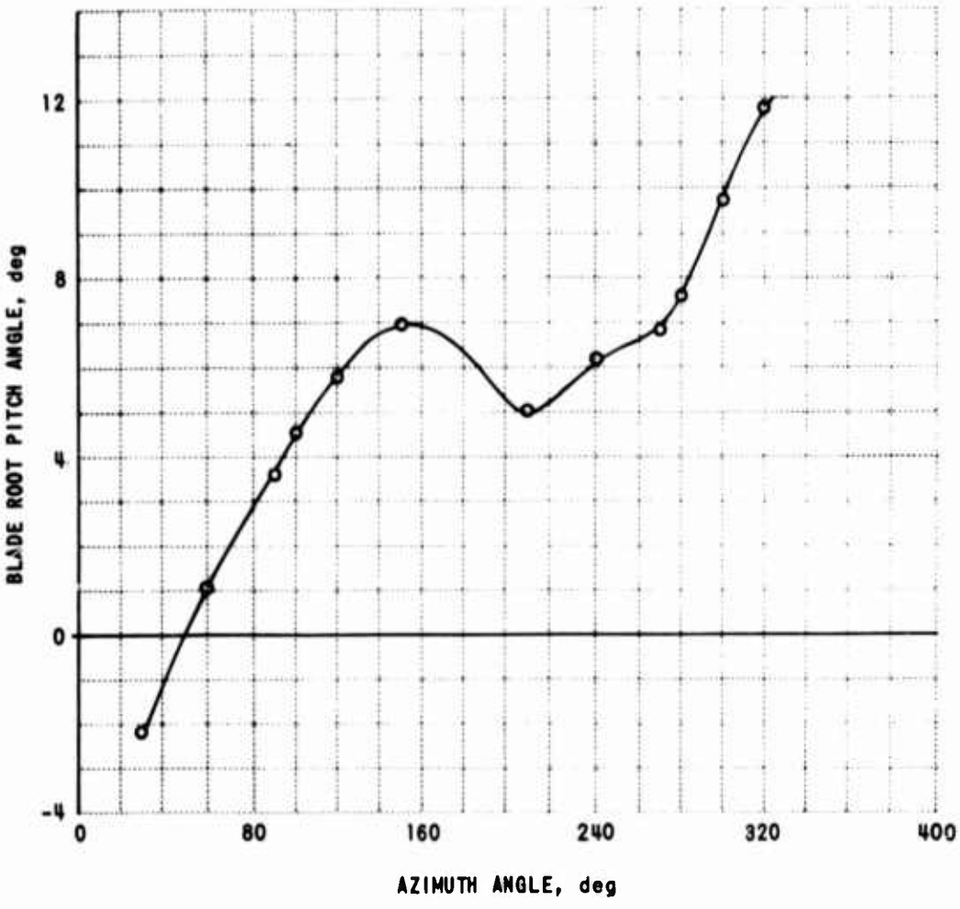

Figure 48. VARIATION OF BLADE ROOT PITCH ANGLE FOR ZERO NORMAL FORCE AT ZERO SHAFT ANGLE

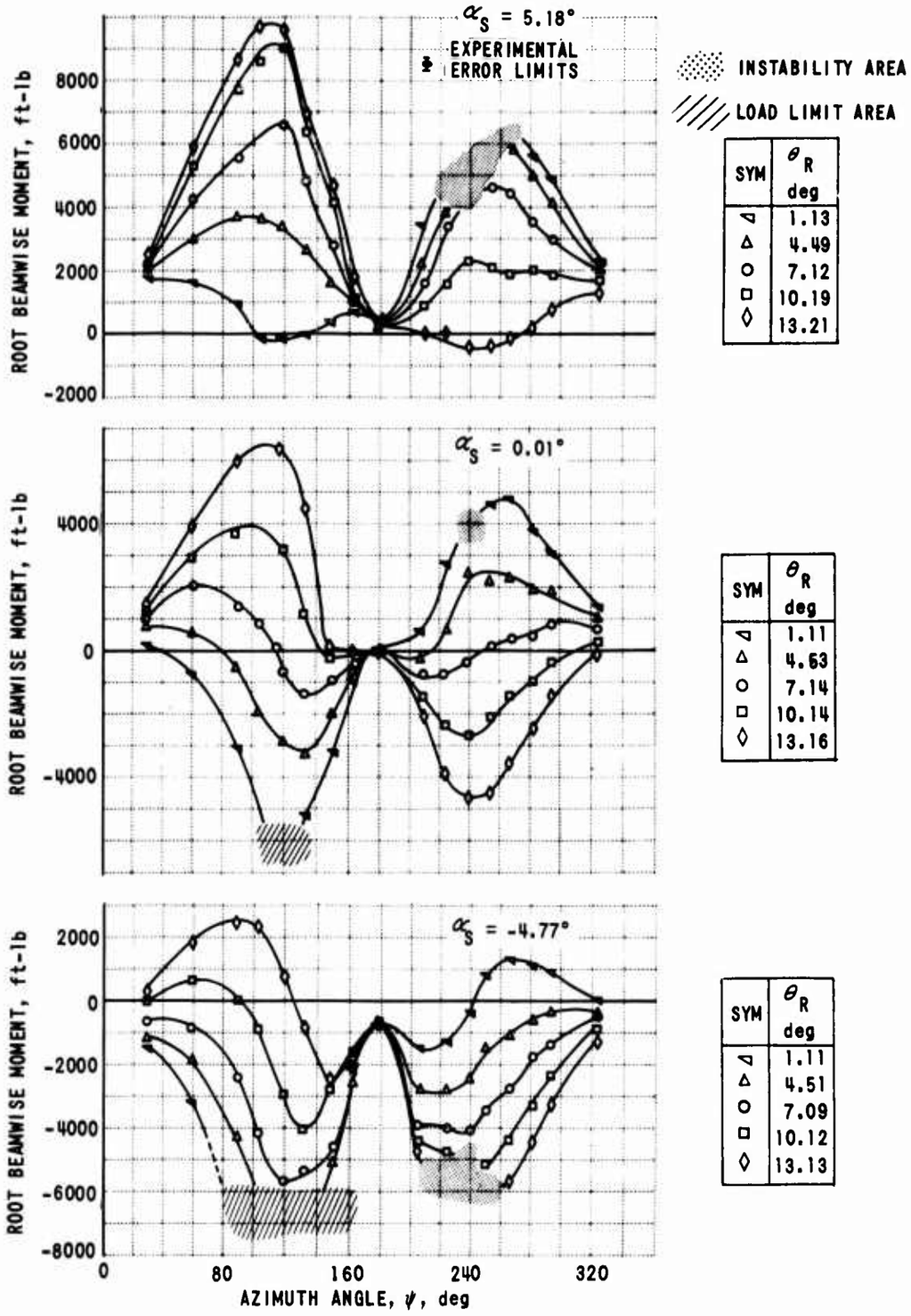

Figure 49. ROOT BEAMWISE MOMENT VS AZIMUTH ANGLE FOR VARIOUS SHAFT ANGLES AT q = 28.93

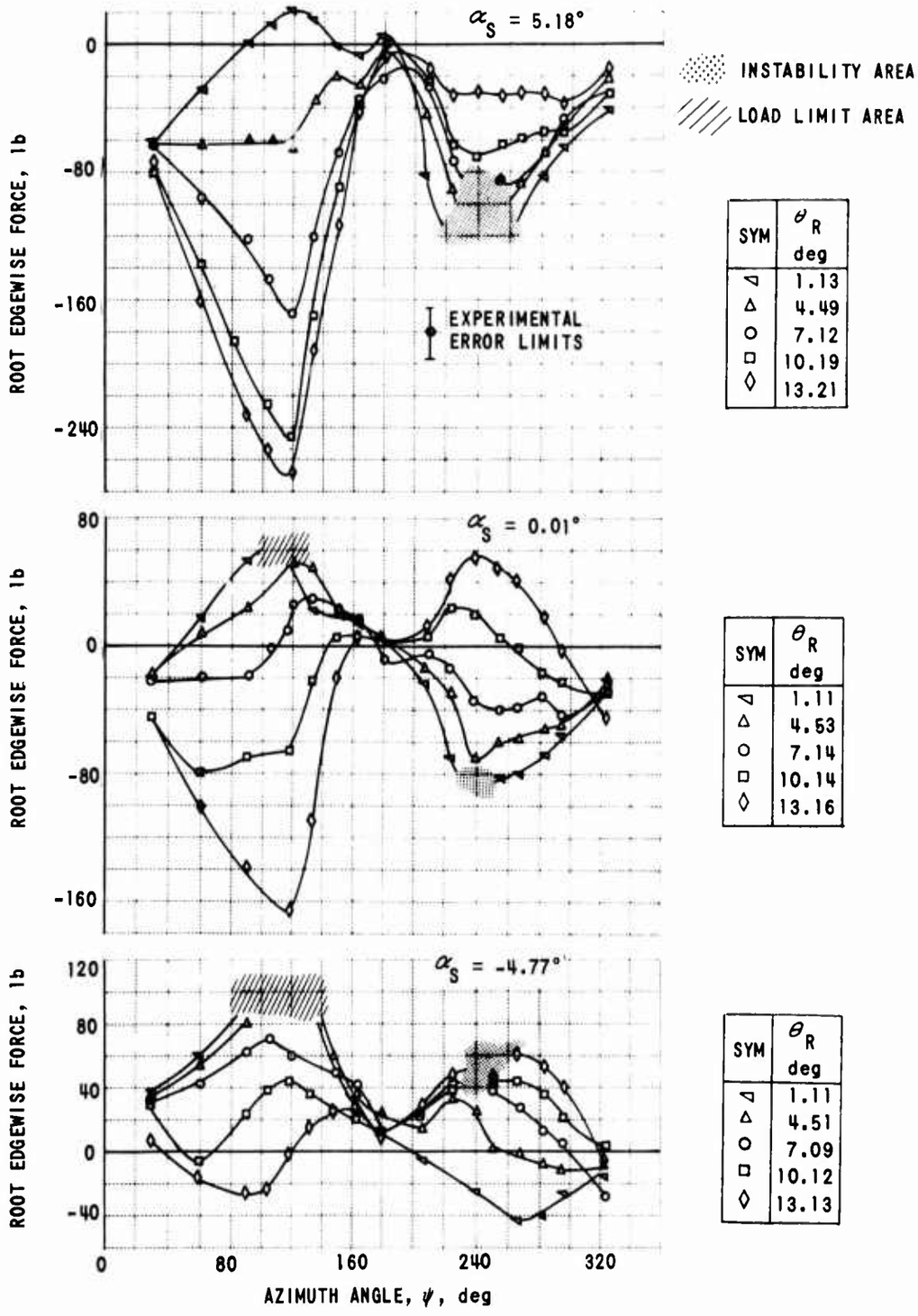

Figure 50. ROOT EDGEWISE FORCE VS AZIMUTH ANGLE FOR VARIOUS SHAFT ANGLES AT q = 28.93

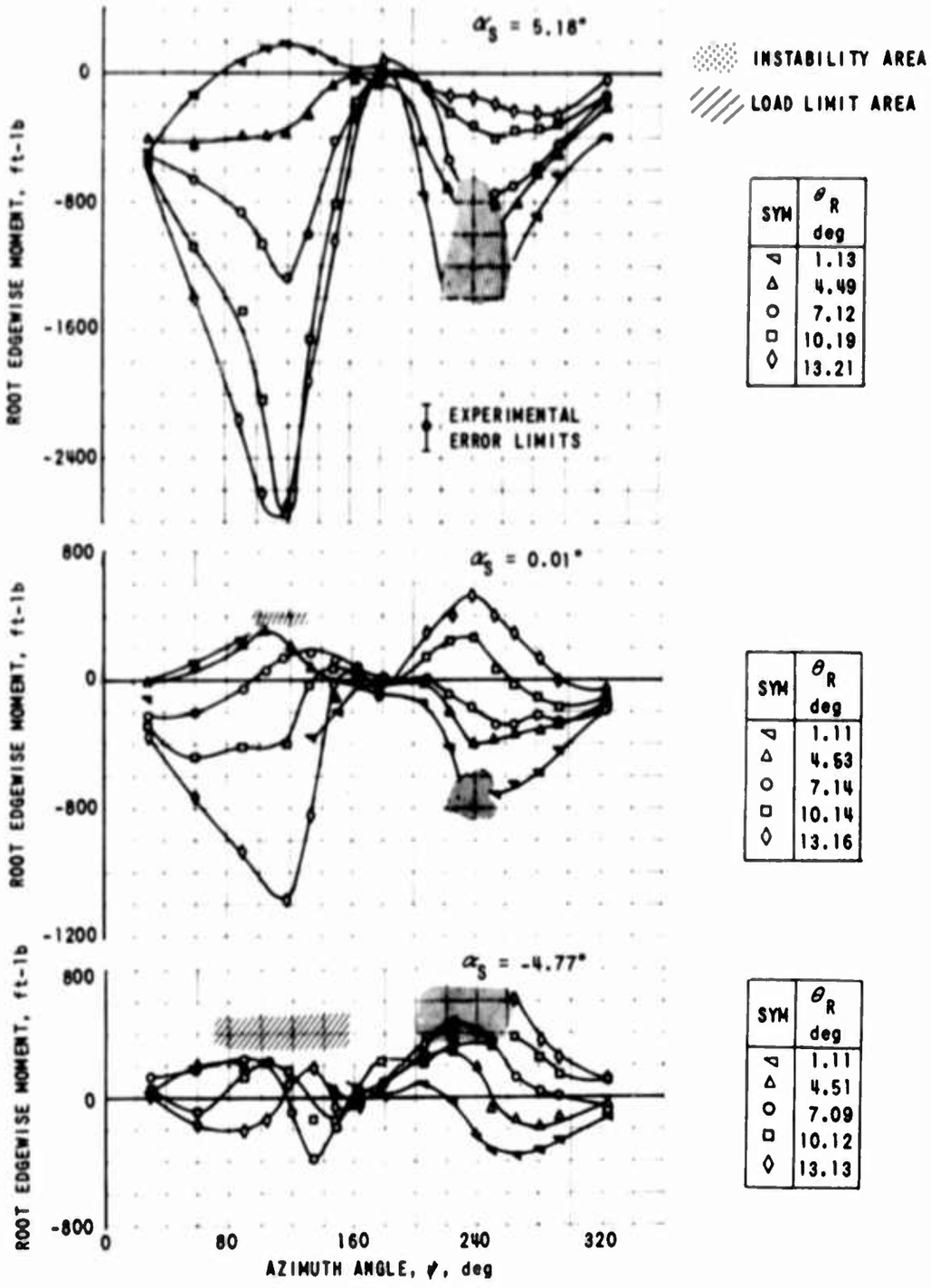

Figure 51. ROOT EDGEWISE MOMENT VS AZIMUTH ANGLE FOR VARIOUS SHAFT ANGLES AT q = 28.93

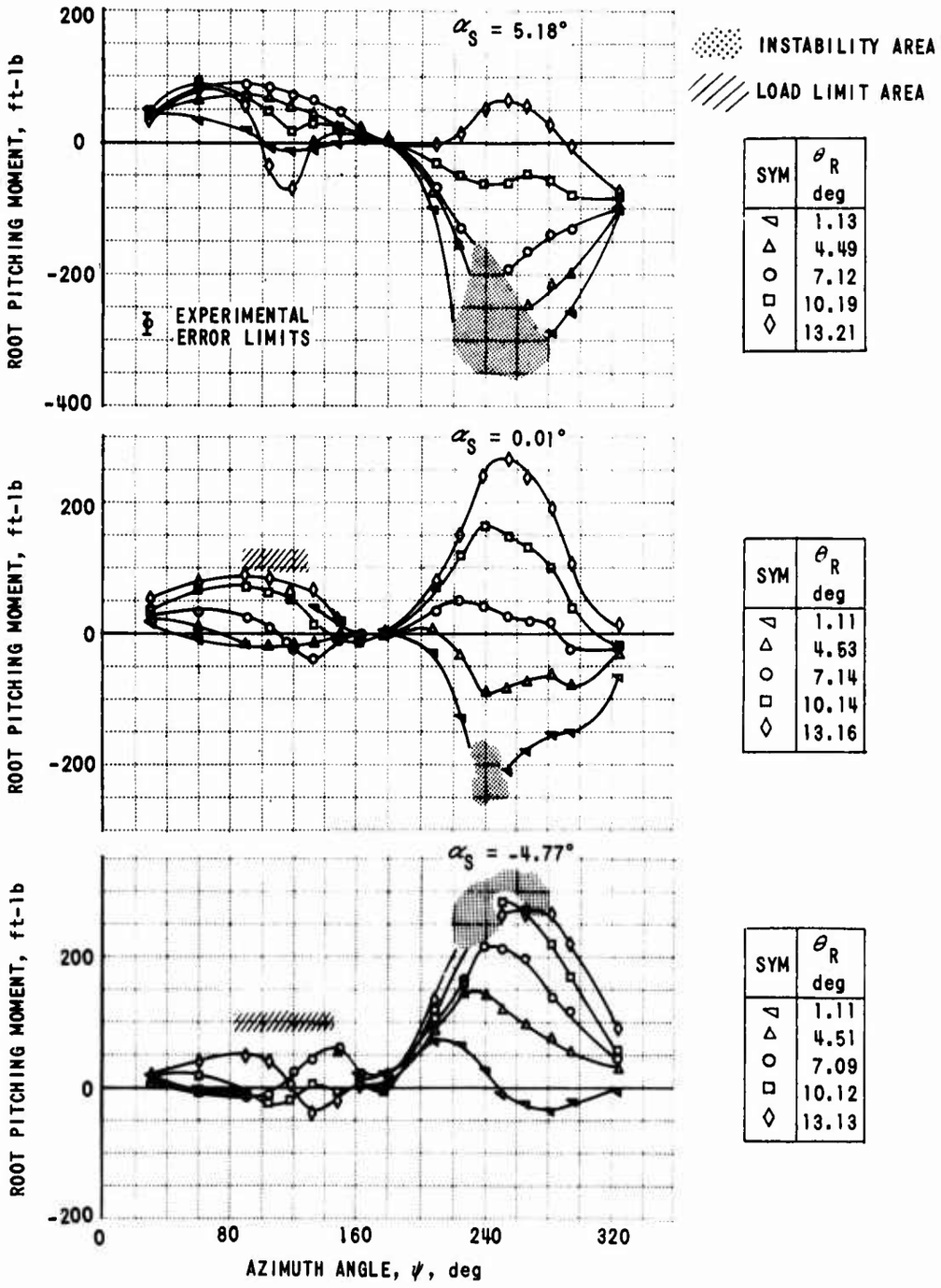

Figure 52. ROOT PITCHING MOMENT VS AZIMUTH ANGLE FOR VARIOUS SHAFT ANGLES AT q = 28.93

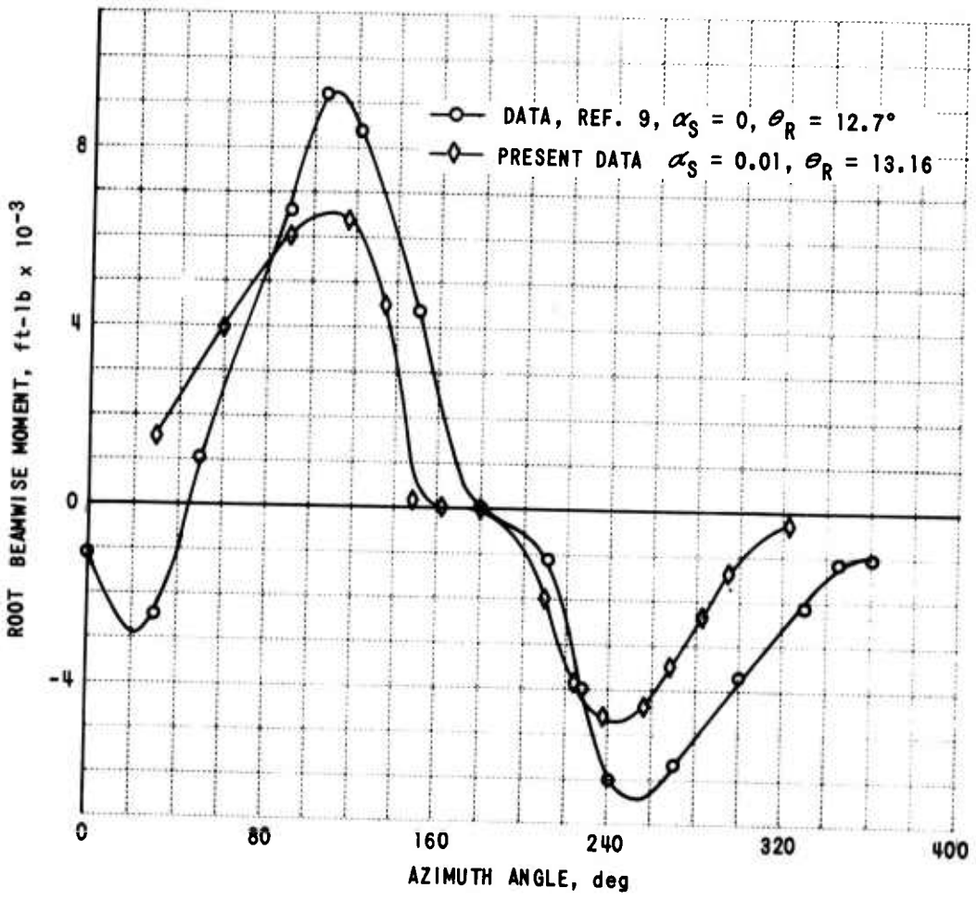

Figure 53. VARIATION OF ROOT BEAMWISE MOMENTS WITH AZIMUTH ANGLE FOR TWO DIFFERENT ROTOR BLADES

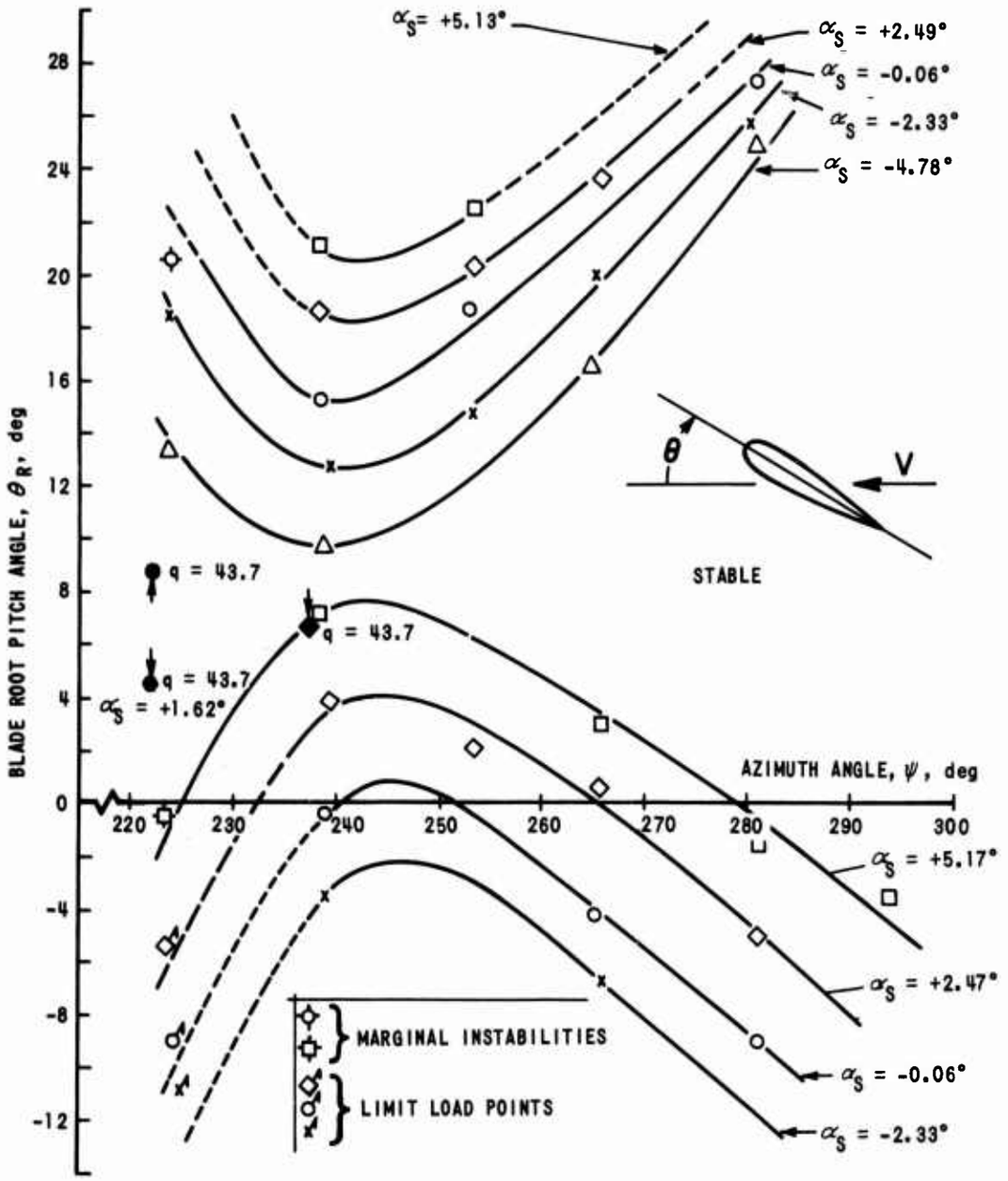

Figure 54 BASIC STABILITY BOUNDARIES

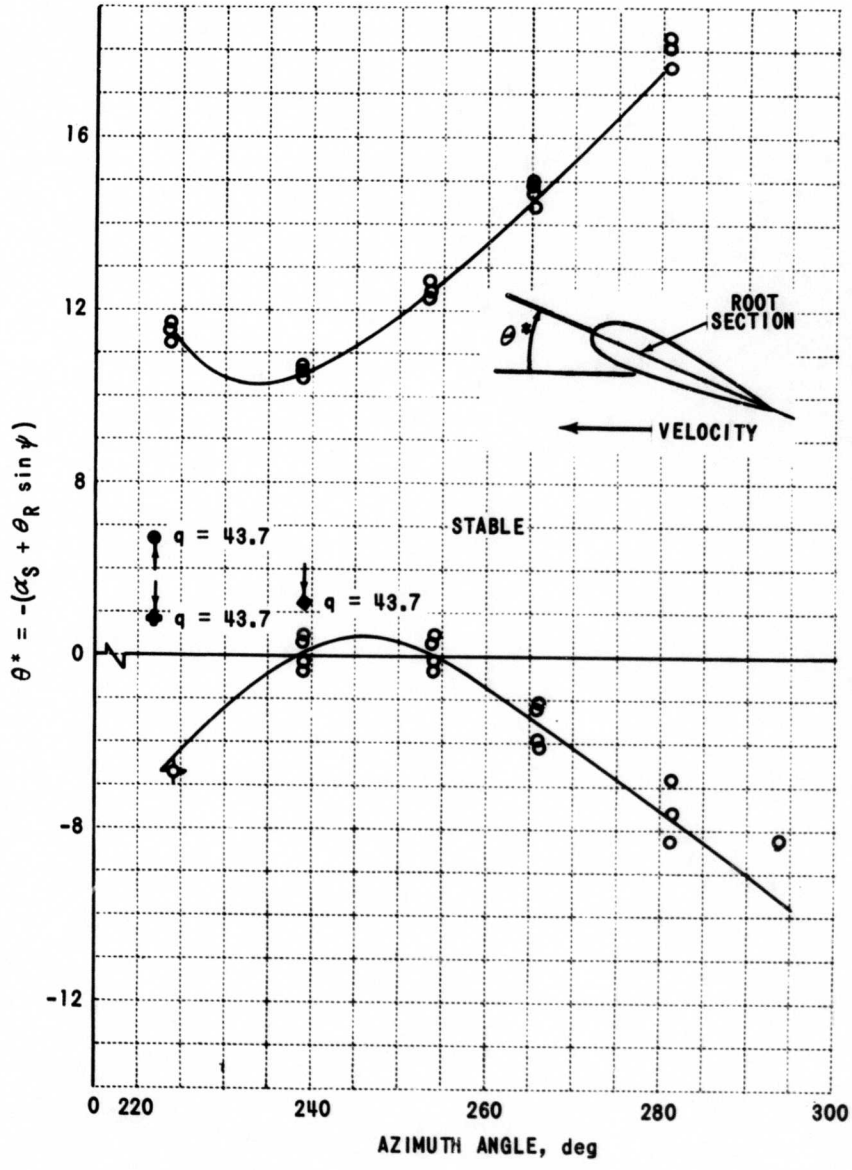

Figure 55. COMPOSITE STABILITY BOUNDARIES

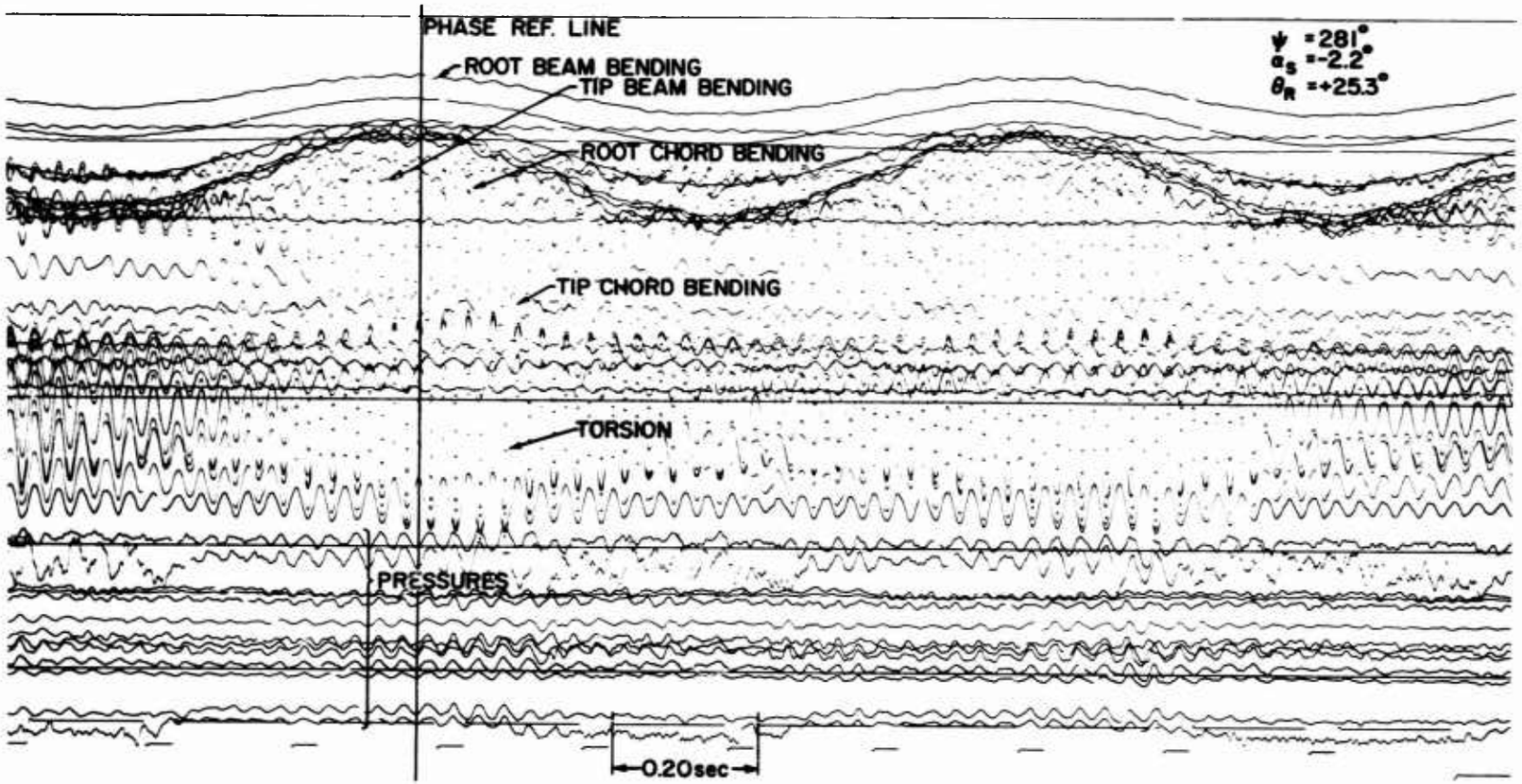

Figure 56. BLADE STRAINS AT STABILITY BOUNDARY

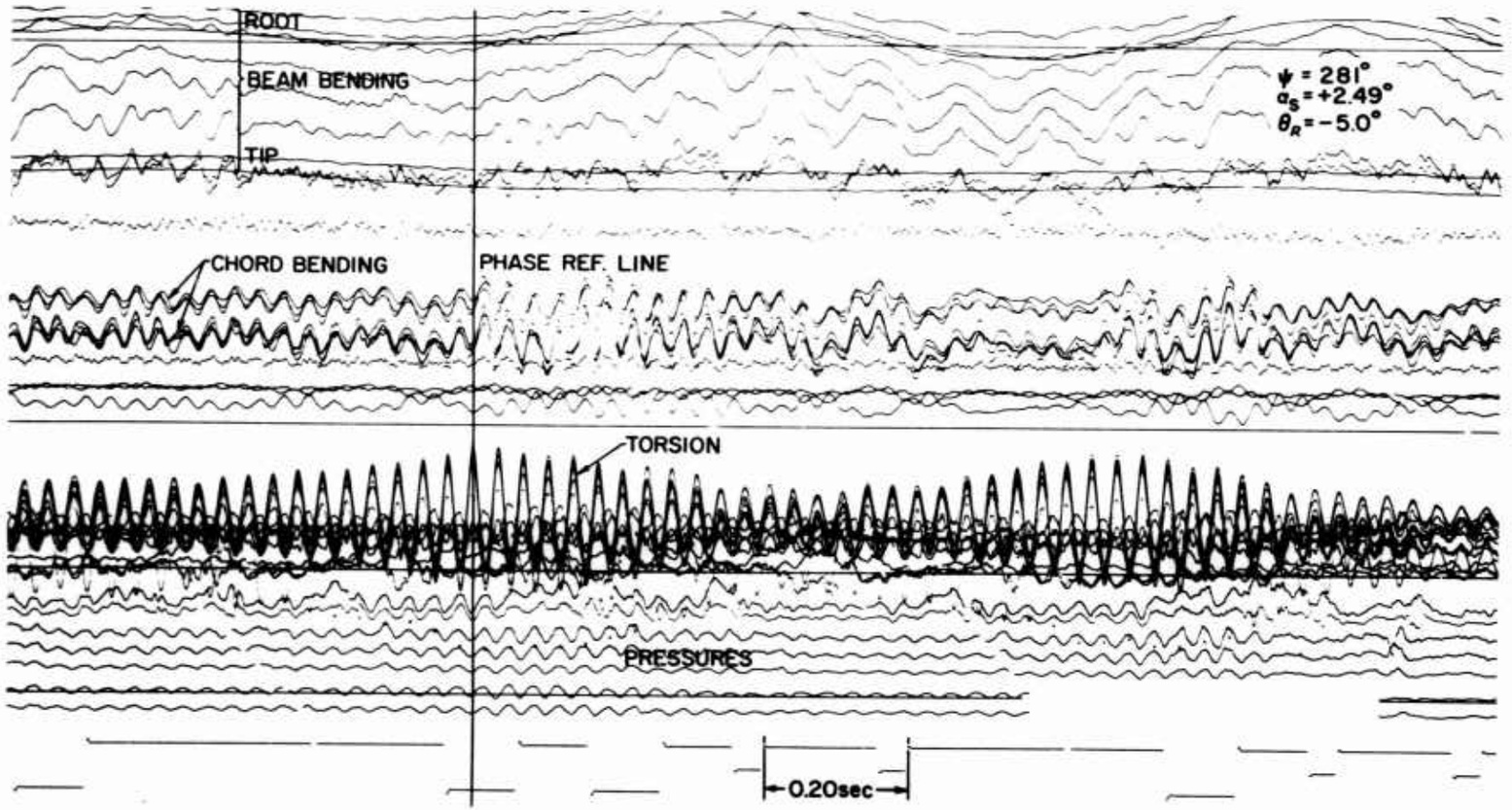

Figure 57. BLADE STRAINS AT STABILITY BOUNDARY

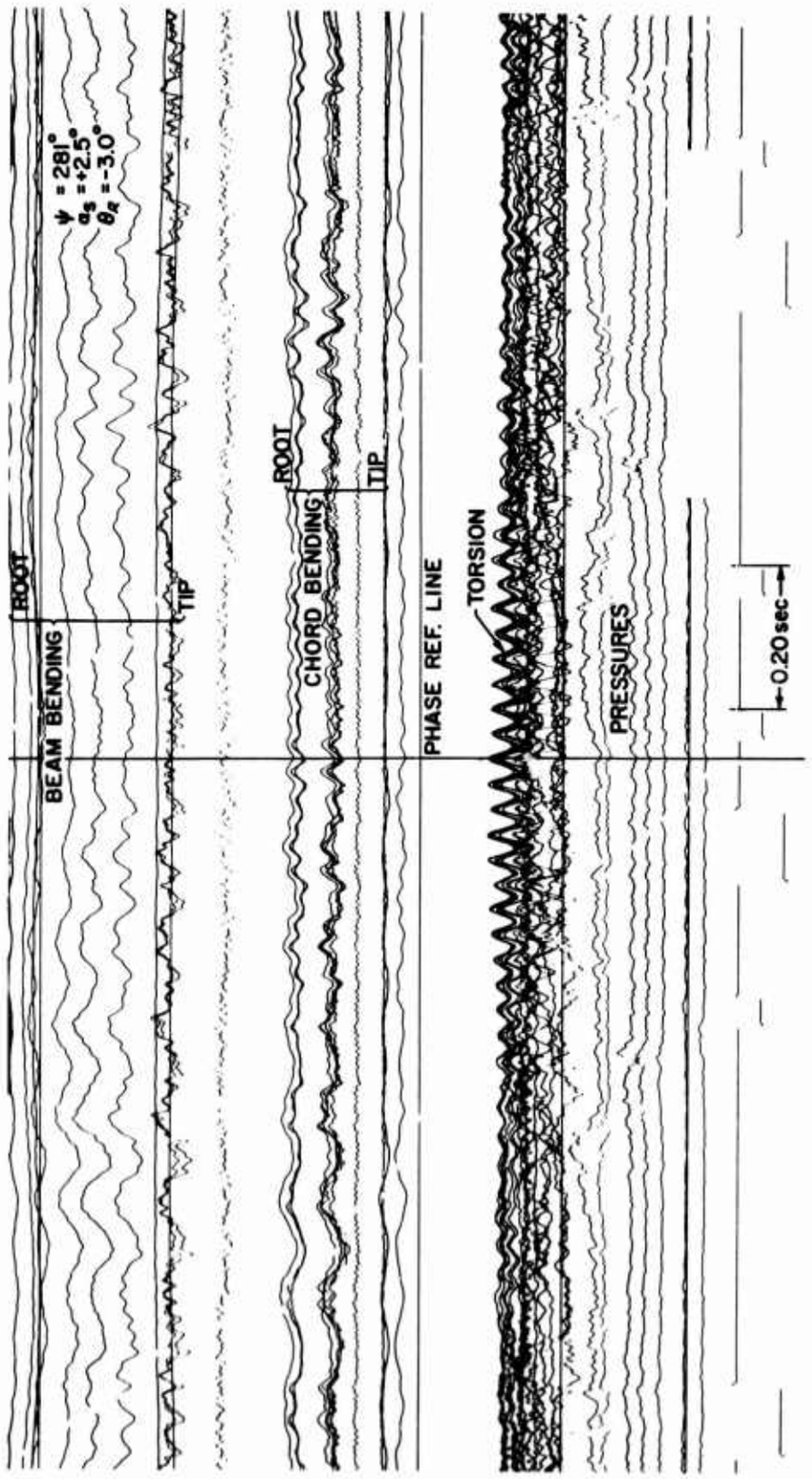

Figure 58. BLADE STRAINS JUST BELOW STABILITY BOUNDARY

APPENDIX

DETAILED DEVELOPMENT OF THE LIFTING SURFACE INTEGRAL EQUATION AND ITS SOLUTION

The basic lifting-surface problem is embodied in the solution to the following integral equations for $\mathcal{L}(x_0, y_0)$, the blade loading:

$$\alpha(x, y) = -\frac{1}{8\pi} \iint_S \frac{\mathcal{L}(x, y_0)}{(y-y_0)^2} \left\{ 1 + \frac{(x-x_0)}{[(x-x_0)^2 + (y-y_0)^2]^{\frac{1}{2}}} \right\} dx_0 dy_0 \qquad (8)$$

This equation is derived in References 3 and 4. The "finite part" of the divergent integrals is understood here (see References 3 and 4). $\alpha(x, y)$ is the local slope of the wing surface in the streamwise direction and is considered as known. S is the wing planform. Equation (8) is the result of representing the rotor blade by a distribution of bound vorticity [whose strength is proportional to $\mathcal{L}(x_0, y_0)$] and the wake by trailing vorticity, whose strength is related to the bound vorticity by the Helmholtz laws. Equation (8) can then be interpreted as a linearized version of flow tangency at the blade surface. Equation (8) is solved by assuming a functional form of $\mathcal{L}(x_0, y_0)$, which is linear in certain unknown constants. The integration indicated is then performed to obtain a linear relation between $\mathcal{L}(x, y)$ and these unknown constants. The unknown constants are then evaluated by requiring exact flow tangency at a compatible number of points (referred to as collocation points) in the rotor planform. The integrations must be performed numerically and require isolation of the strong singularity in the kernel of Equation (8).

The overall approach to the problem was that employed by Hsu (Reference 5). However, the details of the problem are vastly complicated owing to the nonsymmetrical planform under consideration. Because of the rectangular planforms that are under consideration at arbitrary yaw angles, it is advantageous to make the following transformations of independent variables, the first being a rotation of axis such that

$$x = \xi' \cos\psi - \eta' \sin\psi$$

$$y = \xi' \sin\psi - \eta' \cos\psi$$

then, a nonuniform stretching by letting

$$\xi = \xi'/c$$

$$\eta = \eta'/b$$

where c is one-half of the chord of the wing and b is one-half of the wing span. As can be seen, this transformation reduces the wing to a yawed square. Equation (8) then becomes

$$\alpha'(\xi,\eta) = -\frac{bc}{8\pi}\int_{-1}^{1}\int_{-1}^{1}\frac{\mathcal{L}'(\xi_0,\eta_0)}{[c\sin\psi(\xi-\xi_0)+b\cos\psi(\eta-\eta_0)]^2}\left\{1+\frac{c\cos\psi(\xi-\xi_0)-b\sin\psi(\eta-\eta_0)}{[c^2(\xi-\xi_0)^2+b^2(\eta-\eta_0)^2]^{\frac{1}{2}}}\right\}d\xi_0\eta_0 \quad (9)$$

It is now assumed that $\mathcal{L}'(\xi_0,\eta_0)$ is of the following form:

$$\mathcal{L}'(\xi_0,\eta_0) = \frac{P_1}{\sqrt{1-\xi_0^2}} + \frac{P_2}{\sqrt{1-\eta_0^2}} \quad (10)$$

where

$$\begin{aligned}P_1 = (1-\eta_0^2)\Big\{&\left[a_{00}+a_{01}\eta_0+a_{02}\eta_0^2+a_{03}\eta_0^3+a_{04}\eta_0^4\right](1-\xi_0)\\&+\left[a_{10}+a_{11}\eta_0+a_{12}\eta_0^2+a_{13}\eta_0^3+a_{14}\eta_0^4\right](1-\xi_0^2)\\&+\left[a_{20}+a_{21}\eta_0+a_{22}\eta_0^2+a_{23}\eta_0^3+a_{24}\eta_0^4\right](1-\xi_0^2)\xi_0\Big\}\\&+\left(\frac{3}{4}-\frac{1}{2}\eta_0-\frac{1}{4}\eta_0^2\right)\left[a_{30}(1-\xi_0)+a_{31}(1-\xi_0^2)+a_{32}(1-\xi_0^2)\xi_0\right]\end{aligned} \quad (11)$$

$$\begin{aligned}P_2 = (1-\xi_0^2)\Big\{&\left[l_{00}+l_{01}\xi_0+l_{02}\xi_0^2+l_{03}\xi_0^3+l_{04}\xi_0^4\right](1-\eta_0)\\&+\left[l_{10}+l_{11}\xi_0+l_{12}\xi_0^2+l_{13}\xi_0^3+l_{14}\xi_0^4\right](1-\eta_0^2)\\&+\left[l_{20}+l_{21}\xi_0+l_{22}\xi_0^2+l_{23}\xi_0^3+l_{24}\xi_0^4\right](1-\eta_0^2)\eta_0\Big\}\\&+\left(\frac{3}{4}-\frac{1}{2}\xi_0-\frac{1}{4}\xi_0^2\right)\left[l_{30}(1-\eta_0)+l_{31}(1-\eta_0^2)+l_{32}(1-\eta_0^2)\eta_0\right]\end{aligned} \quad (12)$$

This form then contains 18 a's and 18 l's, for a total of 36 unknown coefficients for which a solution must be obtained. These mode shapes also restrict the range of ψ such that $\eta = -1$ and $\xi = -1$ must always physically represent the leading edges of the wing, since these lines are the square root singularity lines of the loading modes. This implies that the azimuth angle must be in the range of $0 \le \psi \le \frac{\pi}{2}$. However, this represents no loss of generality, since any yaw position can be transformed to an equivalent aerodynamic problem with ψ in this range.

Equations (10), (11), and (12) can now be substituted in Equation (9) and integrated to yield an expression of the form

$$\begin{aligned}\alpha(\xi,\eta) = {} & A_{00}a_{00} + A_{01}a_{01} + A_{02}a_{02} + A_{03}a_{03} + A_{04}a_{04} + A_{10}a_{10} \\ & + A_{11}a_{11} + A_{12}a_{12} + A_{13}a_{13} + A_{14}a_{14} + A_{20}a_{20} + A_{21}a_{21} \\ & + A_{22}a_{22} + A_{23}a_{23} + A_{24}a_{24} + A_{30}a_{30} + A_{31}a_{31} + A_{32}A_{32} \\ & + L_{00}l_{00} + L_{01}l_{01} + L_{02}l_{02} + L_{03}l_{03} + L_{04}l_{04} + L_{10}l_{10} \\ & + L_{11}l_{11} + L_{12}l_{12} + L_{13}l_{13} + L_{14}l_{14} + L_{20}l_{20} + L_{21}l_{21} \\ & + L_{22}l_{22} + L_{23}l_{23} + L_{24}l_{24} + L_{30}l_{30} + L_{31}l_{31} + L_{32}l_{32} \\ & + L_{33}l_{33} \end{aligned} \tag{13}$$

where

$$A_{xx} = A_{xx}(\xi,\eta)$$

$$L_{xx} = L_{xx}(\xi,\eta)$$

Since $\alpha(\xi,\eta)$ is known, j values of ξ and i values of η such that $i \times j = 36$ can be selected and exact tangency required at these locations (collocation points). Then, Equation (13) represents a system of 36 linear algebraic equations that can be solved for the a's and l's.

To obtain the A's and L's, the integration of Equation (9) is divided into two parts. We first let

$$G_1 = \frac{c\cos\psi(\xi-\xi_0) - b\sin\psi(\eta-\eta_0)}{\left[c^2(\xi-\xi_0)^2 + b^2(\eta-\eta_0)^2\right]^{1/2}} \tag{14}$$

and

$$\bar{\xi}_0 = \xi + \frac{b}{c}\cot\psi(\eta-\eta_0) \tag{15}$$

$$\bar{\eta}_0 = \eta + \frac{c}{b}\tan\psi(\xi-\xi_0) \tag{16}$$

Then, $\alpha'(\xi,\eta)$ can be expressed as

$$\alpha'(\xi,\eta) = I_1 + I_2$$

where

$$I_1 = -\frac{1}{8\pi}\frac{c}{b}\int_{-1}^{1}\int_{-1}^{1}\frac{P_1(\xi_0,\eta_0)}{\sqrt{1-\xi_0^2}\,[\bar{\eta}_0-\eta_0]^2}\,\frac{G_1(\xi_0,\eta_0,\xi,\eta)}{\cos^2\psi}\,d\eta_0 d\xi_0 \tag{17}$$

and

$$I_2 = -\frac{1}{8\pi}\frac{b}{c}\int_{-1}^{1}\int_{-1}^{1}\frac{P_2(\xi_0,\eta_0)}{\sqrt{1-\eta_0^2}\,[\bar{\xi}_0-\xi_0]^2}\,\frac{G_1(\xi_0,\eta_0,\xi,\eta)}{\sin^2\psi}\,d\eta_0 d\xi_0 \tag{18}$$

Only the detailed evaluation of I will be discussed in detail since there are many similarities involved in the two integrations. P_1 and G_1 are regular functions in ξ_0,η_0 and present no problems for integration. However, the square singularity in the denominator of the kernel function requires special treatment before numerical calculation can be accomplished. I_1 is first integrated with respect to η_0.

$$I_1 = -\frac{1}{8\pi}\frac{c}{b}\int_{-1}^{1}\int_{-1}^{1}\frac{P_1(\xi_0-\eta_0)}{\sqrt{1-\xi_0^2}\,[\bar{\eta}_0-\eta_0]^2}\,\frac{G_1(\xi_0,\eta_0,\xi,\eta)}{\cos^2\psi}\,d\eta_0 d\xi_0$$

$$= -\frac{1}{8\pi}\frac{c}{b}\int_{-1}^{1}\int_{-1}^{1}\frac{P_1(\xi_0,\eta_0)-P_1(\xi_0,\eta_0)}{\sqrt{1-\xi_0^2}\,[\bar{\eta}_0-\eta_0]^2}\,\frac{G_1(\xi_0,\eta_0,\xi,\eta)}{\cos^2\psi}\,d\eta_0 d\xi_0$$

$$-\frac{1}{8\pi}\frac{c}{b}\int_{-1}^{1}\frac{P_1(\xi_0,\bar{\eta}_0)}{\sqrt{1-\xi_0^2}}\int_{-1}^{1}\frac{G_1(\xi_0,\eta_0,\xi,\eta)}{\cos^2\psi\,[\bar{\eta}_0-\eta_0]^2}\,d\eta_0 d\xi_0 \tag{19}$$

$$bc\int\frac{G_1(\xi_0,\eta_0,\xi,\eta)}{b^2\cos^2\psi[\bar{\eta}_0-\eta_0]^2}\,d\eta_0 = \frac{(\xi-\xi_0)+\cos\psi\left[(\xi-\xi_0)^2+\frac{b}{c}(\eta-1)^2\right]^{1/2}}{(\xi-\xi_0)\cos\psi\left[\sin\psi(\xi_0-\xi_0)+\frac{b}{c}\cos\psi(\eta+1)\right]}$$

$$-\frac{(\xi-\xi_0)+\cos\psi\left[(\xi-\xi_0)^2+\left(\frac{b}{c}\right)^2(\eta+1)^2\right]^{1/2}}{(\xi-\xi_0)\cos\psi\left[\sin\psi(\xi-\xi_0)+\frac{b}{c}\cos\psi(\eta+1)\right]} \equiv J_5(\xi_0,\xi,\eta) \tag{20}$$

The ξ_0 integration of the last integral in Equation (19) is accomplished numerically by Chebyshev-Gauss quadrature (Reference 5). Briefly, this quadrature can be summarized as

$$\int_{-1}^{1}\frac{f(x)}{\sqrt{1-x^2}}\,dx = \sum_{j=1}^{n}\frac{\pi}{n}f(x_j) \tag{21}$$

where the x_j are selected according to the rule

$$x_j = \cos\left(\frac{2j-1}{2n}\right)\pi \tag{22}$$

where the integral is exact if $f(x)$ is a polynomial of degree less than $2n-1$. Otherwise, the degree of precision is $2n-1$.

Then

$$-\frac{1}{8\pi}\frac{c}{b}\int_{-1}^{1}\frac{P_1(\xi_0,\bar{\eta}_0)}{\sqrt{1-\xi_0^2}}J_s(\xi_0,\xi,\eta)\,d\xi_0$$

$$=-\frac{1}{8r}\sum_{p=1}^{r}P(\xi_p,\bar{\eta}_0)\,J_s(\xi_p,\xi,\eta) \tag{23}$$

and it is to be remembered that

$$\bar{\eta}_0=\bar{\eta}_0(\xi_p,\xi,\eta)$$

Now, continuing treatment of the first integral in Equation (19), we let

$$\frac{P_1(\xi_0,\eta_0)-P_1(\xi_0,\bar{\eta}_0)}{(\bar{\eta}_0-\eta_0)}=H_1(\xi_0,\eta_0) \tag{24}$$

and, using the first term of its Taylor Series expansion, $H_1(\xi_0,\bar{\eta}_0$ is calculated as

$$H_1(\xi_0,\bar{\eta}_0)=-\left.\frac{\partial P_1}{\partial\eta_0}\right|_{\eta_0=\bar{\eta}_0} \tag{25}$$

Then $H_1(\xi_0,\eta_0)$ is a well-defined function. Equation (19) can now be written as

$$I_1=-\frac{1}{8\pi}\frac{c}{b}\int_{-1}^{1}\int_{-1}^{1}\frac{H_1(\xi_0,\eta_0)\,G_1(\xi_0,\eta_0,\xi,\eta)}{\cos^2\psi\sqrt{1-\xi_0^2}(\bar{\eta}_0-\eta_0)}d\eta_0\,d\xi_0-\frac{1}{8r}\sum_{p=1}^{r}\left(P(\xi_0,\bar{\eta}_0)J_s(\xi_p,\xi,\eta)\right)$$

$$=-\frac{1}{8\pi}\frac{c}{b}\int_{-1}^{1}\int_{-1}^{1}\frac{\left[H_1(\xi_0,\eta_0)-H_1(\xi_0,\bar{\eta}_0)\right]G_1(\xi_0,\eta_0,\xi,\eta)}{\cos^2\psi\sqrt{1-\xi_0^2}(\bar{\eta}_0-\eta_0)}d\eta_0\,d\xi_0$$

$$-\frac{1}{8\pi}\frac{c}{b}\int_{-1}^{1}\frac{H_1(\xi_0,\bar{\eta}_0)}{\sqrt{1-\xi_0^2}}\int_{-1}^{1}\frac{G_1(\xi_0,\eta_0,\xi,\eta)}{\cos^2\psi(\bar{\eta}_0-\eta_0)}d\eta_0\,d\xi_0$$

$$-\frac{1}{8\pi}\sum_{p=1}^{r}P_1(\xi_p,\bar{\eta}_0)\,J_s(\xi_p,\xi,\eta) \tag{26}$$

We now let

$$H_2 = \frac{H_1(\xi_0, \eta_0) - H_1(\xi_0, \eta_0)}{\bar{\eta}_0 - \eta_0} = H_2(\xi_0, \eta_0, \xi, \eta)$$

with

$$H_2(\xi_0, \bar{\eta}_0, \xi, \eta) = \left.\frac{\partial^2 P_1}{\partial \eta_0^2}\right|_{\eta_0 = \bar{\eta}_0}$$

and now the first integral in Equation (26) presents no problem for numerical integration. In the second integral, the η_0 integration is performed analytically as

$$\frac{c}{b}\int_{-1}^{1} \frac{G_1(\xi_0, \eta_0, \xi, \eta)}{\cos^2\psi(\bar{\eta}_0 - \eta_0)}\, d\eta_0 = J_2 + J_3 + J_4 \tag{27}$$

where

$$J_2 = \frac{\frac{c}{b}\,\mathrm{sgn}(\xi - \xi_0)}{\cos^2\psi} \ln\left|\frac{A_1}{A_2}\right| \tag{28}$$

$$A_1 = \left\{|\cos\psi|\left[b^2(\eta+1)^2 + c^2(\xi-\xi_0)^2\right]^{\frac{1}{2}} + c|\xi-\xi_0| - \mathrm{sgn}(\xi-\xi_0)\sin\psi\left[b\cos\psi(\eta+1) + c\sin\psi(\xi-\xi_0)\right]\right\}\left[b\cos\psi(\eta+1) + c\sin\psi(\xi-\xi_0)\right]$$

$$A_2 = \left\{|\cos\psi|\left[b^2(\eta+1)^2 + c^2(\xi-\xi_0)^2\right]^{\frac{1}{2}} + c|\xi-\xi_0| - \mathrm{sgn}(\xi-\xi_0)\sin\psi\left[b\cos\psi(\eta+1) + c\sin\psi(\xi-\xi_0)\right]\right\}\left[b\cos\psi(\eta-1) + c\sin\psi(\xi-\xi_0)\right]$$

$$J_3 = \frac{\frac{c}{b}}{\cos^2\psi} \ln\left|b\cos\psi(\eta+1) + c\sin\psi(\xi-\xi_0)\right| - \frac{c}{b}\frac{\sin\psi}{\cos^2\psi}\,\mathrm{sgn}(\cos\psi)\ln\left|\left[b^2(\eta+1)^2 + c^2(\xi-\xi_0)^2\right]^{\frac{1}{2}} + b(\eta+1)\,\mathrm{sgn}(\cos\psi)\right| \tag{29}$$

$$J_4 = -\frac{\frac{c}{b}}{\cos^2\psi} \ln\left|b\cos\psi(\eta+1) + c\sin\psi(\xi-\xi_0)\right| + \frac{c}{b}\frac{\sin\psi}{\cos^2\psi}\,\mathrm{sgn}(\cos\psi)\ln\left|\left[b^2(\eta-1)^2 + c^2(\xi-\xi_0)^2\right]^{\frac{1}{2}} + b(\eta-1)\,\mathrm{sgn}(\cos\psi)\right| \tag{30}$$

Examination of J_3 shows that it is singular at $\xi_0 = \bar{\xi}_0 = \xi + \frac{b}{c}\cot\psi(\eta+1)$ if $-1 \le \bar{\xi}_0 \le 1$. J_4 is singular at $\xi_0 = \bar{\xi}_{02} = \xi + \frac{b}{c}\cot\psi(\eta+1)$ if $-1 \le \xi_{02} \le 1$. These singularities must be isolated before the ξ_0 integration can be completed. Then, the second integral in Equation (26) is evaluated as

$$\frac{c}{b}\int_{-1}^{1}\frac{H_1(\xi_0,\bar{\eta}_0)}{\sqrt{1-\xi_0^2}}\int_{-1}^{1}\frac{G_1(\xi_0,\eta_0,\xi,\eta)}{\cos^2\psi(\bar{\eta}_0-\eta_0)}\,d\eta_0\,d\xi_0 = \int_{-1}^{1}\frac{H_1(\xi_0,\bar{\eta}_0)}{\sqrt{1-\xi_0^2}}\left\{J_2+J_3+J_4\right\}d\xi_0$$

$$= \int_{-1}^{1}\frac{H_1(\xi_0,\bar{\eta}_0)}{\sqrt{1-\xi^2}}J_2(P_0,\xi,\eta)\,d\xi_0 + \int_{-1}^{1}\left\{\frac{H_1(\xi_0,\bar{\eta}_0)}{\sqrt{1-\xi_0^2}} - \frac{H_1(\bar{\xi}_0,\bar{\eta}_0)}{\sqrt{1-\bar{\xi}_{01}^2}}\right\}J_2(\xi_0,\xi,\eta)\,d\xi_0$$

$$- \frac{H_1(\bar{\xi}_0,\bar{\eta}_0)}{\sqrt{1-\xi_{01}^2}}\int_{-1}^{1}J_3(\xi_0,\xi,\eta)\,d\xi_0 + \int_{-1}^{1}\left\{\frac{H_1(\xi_0,\eta_0)}{\sqrt{1-\xi_0^2}} - \frac{H_1(\bar{\xi}_{02},\bar{\eta}_0)}{\sqrt{1-\bar{\xi}_{02}^2}}\right\}J_4(\xi_0,\xi,\eta)\,d\xi_0$$

$$- \frac{H_1(\bar{\xi}_{02},\bar{\eta}_0)}{\sqrt{1-\bar{\xi}_{02}^2}}\int_{-1}^{1}J_4(\xi_0,\xi,\eta)\,d\xi_0 \qquad (31)$$

The following integrals are evaluated analytically:

$$\int_{-1}^{1}J_3(\xi_0,\xi,\eta)\,d\xi_0 = J_3(\xi,\eta) = \frac{-\frac{c}{b}}{c\sin\psi\cos^2\psi}\left\{\left[b\cos\psi(\eta+1)+c\sin\psi(\xi-1)\right]\ln\left|b\cos\psi(\eta+1)\right.\right.$$

$$\left.+c\sin\psi(\xi-1)\right| - \left[b\cos\psi(\eta+1)+c\sin\psi(\xi+1)\right]\ln\left|b\cos\psi(\eta+1)+c\sin\psi(\xi+1)\right| + 2c\sin\psi\Big\}$$

$$+\frac{\frac{c}{b}\sin\psi\,\mathrm{sgn}(\cos\psi)}{c\cos^2\psi}\left\{2b(\eta+1)\ln 2b(\eta+1) - c(\xi+1)\ln\left|\left[b^2(\eta+1)^2+c^2(\xi+1)^2\right]^{\frac{1}{2}}+b(\eta+1)\right|\right.$$

$$-b(\eta+1)\ln 2\left|\left[b^2(\eta+1)^2+c^2(\xi+1)^2\right]^{\frac{1}{2}}+c(\xi+1)\right| + c(\xi+1)\ln\left|\left[b^2(\eta+1)^2+c^2(\xi+1)^2\right]^{\frac{1}{2}}+b(\eta+1)\right|$$

$$\left.-b(\eta+1)\ln 2\left|\left[b^2(\eta+1)^2+c^2(\xi-1)^2\right]^{\frac{1}{2}}+c(1-\xi)\right|+2a\right\} \qquad (32)$$

$$\int_{-1}^{1}J_4(\xi_0,\xi,\eta)\,d\xi_0 = J_4(\xi,\eta) = \frac{\frac{c}{b}}{c\sin\psi\cos^2\psi}\left\{\left[b\cos\psi(\eta-1)+c\sin\psi(\xi-1)\right]\ln\left|b\cos\psi(\eta-1)\right.\right.$$

$$\left.+c\sin\psi(\xi-1)\right| - \left[b\cos\psi(\eta-1)+c\sin\psi(\xi+1)\right]\ln\left|b\cos\psi(\eta-1)+c\sin\psi(\xi-1)\right| + 2c\sin\psi\Big\}$$

$$+\frac{\frac{c}{b}\sin\psi\,\mathrm{sgn}(\cos\psi)}{c\cos^2\psi}\left\{2b(\eta-1)\ln 2b(1-\eta) - c(\xi+1)\ln\left|\left[b^2(\eta-1)^2+c^2(\xi+1)^2\right]+b(\eta-1)\right|\right.$$

$$-b(\eta-1)\ln 2\left|\left[b^2(\eta-1)^2+c^2(\xi+1)^2\right]^{\frac{1}{2}}+c(\xi+1)\right| + c(\xi-1)\ln\left|\left[b^2(\eta-1)^2+c^2(\xi-1)^2\right]+b(\eta-1)\right|$$

$$\left.-b(\eta-1)\ln 2\left|\left[b^2(\eta-1)^2+c^2(\xi-1)^2\right]^{\frac{1}{2}}+c(1-\xi)\right|+2c\right\} \qquad (33)$$

Also, let

$$H_3(\xi_0, \xi, \eta) = H_1(\xi_0, \bar{\eta}_0) - H_1(\bar{\xi}_0, \bar{\eta}_0)\frac{\sqrt{1-\xi_0^2}}{\sqrt{1-\bar{\xi}_{01}^2}} \tag{34}$$

$$H_4(\xi_0, \xi, \eta) = H_1(\xi_0, \bar{\eta}_0) - H_1(\bar{\xi}_{02}, \bar{\eta}_0)\frac{\sqrt{1-\xi_0^2}}{\sqrt{1-\bar{\xi}_{02}^2}} \tag{35}$$

$$J_1 = \frac{c}{\delta}\frac{}{\cos^2\psi} G_1(\xi_0, \eta_0, \xi, \eta) \tag{36}$$

Then, Equation (26) becomes

$$\begin{aligned} I_1 = &-\frac{\pi}{8r\omega}\sum_{\rho=1}^{r}\sum_{\beta=1}^{\omega}(1-\eta_\beta^2)^{\frac{1}{2}} H_2(\xi_\rho, \eta_\beta, \xi, \eta) J_1(\xi_\rho, \eta_\beta, \xi, \eta) \\ &-\frac{1}{8r}\sum_{\rho=1}^{r}\Big\{H_1(\xi_\rho, \bar{\eta}_0, \xi, \eta) J_2(\xi_\rho, \xi, \eta) + H_3(\xi_\rho, \xi, \eta) J_3(\xi_\rho, \xi, \eta) \\ &+ H_4(\xi_\rho, \xi, \eta) J_4(\xi_\rho, \xi, \eta) + P_1(\xi_\rho, \bar{\eta}_0) J_5(\xi_\rho, \xi, \eta)\Big\} \\ &-\frac{1}{8\pi}\left\{\frac{H_1(\bar{\xi}_{01}, \bar{\eta}_0, \xi, \eta)}{\sqrt{1-\bar{\xi}_{01}^2}} J_6(\xi, \eta) + \frac{H_1(\bar{\xi}_{02}, \bar{\eta}_0, \xi, \eta)}{\sqrt{1-\bar{\xi}_{02}^2}} J_7(\xi, \eta)\right\} \end{aligned} \tag{37}$$

which, when ξ, η are chosen, is in form for direct numerical evaluation.

The unknown a's are contained in H_1, H_2, H_3, H_4, and P_1; and, before solution can be accomplished, they must be separated so that Equation (37) will be in the form of Equation (13). I_2 is then treated similarly to I_1, and the resulting expression is

$$\begin{aligned} I_2 = &-\frac{\pi}{8r\omega}\sum_{\rho=1}^{r}\sum_{\beta=1}^{\omega}(1-\xi_\rho^2) S_2(\xi_\rho, \eta_\beta, \xi, \eta) K_1(\xi_\rho, \eta_\beta, \xi, \eta) \\ &-\frac{1}{8\omega}\Big\{S_1(\bar{\xi}_0, \eta_\beta, \xi, \eta) K_2(\eta_\beta, \xi, \eta) + S_3(\eta_\beta, \xi, \eta) K_3(\eta_\beta, \xi, \eta) \\ &+ S_4(\xi_\rho, \xi, \eta) K_4(\eta_\beta, \xi, \eta) + P_2(\bar{\xi}_0, \eta_\beta) K_5(\eta_\beta, \xi, \eta)\Big\} \\ &-\frac{1}{8\pi}\left\{\frac{S_1(\bar{\xi}_0, \bar{\eta}_0, \xi, \eta)}{\sqrt{1-\bar{\eta}_{01}^2}} K_6(\xi, \eta) + \frac{S_1(\bar{\xi}_0, \bar{\eta}_0, \xi, \eta)}{\sqrt{1-\bar{\eta}_{02}^2}} K_7(\xi, \eta)\right\} \end{aligned} \tag{38}$$

where

$$S_1 = \frac{P_0(\xi_0,\eta_0) - P_1(\bar{\xi}_0,\eta_0)}{(\xi_0 - \bar{\xi}_0)} + S_1(\xi_0,\eta_0) \tag{39}$$

and

$$S_1(\bar{\xi}_0,\eta_0) = -\left.\frac{\partial P_1}{\partial \xi_0}\right|_{\xi_0=\bar{\xi}_0} \tag{40}$$

$$S_2(\xi_0,\eta_0) = \frac{S_1(\xi_0,\eta_0) - S_1(\bar{\xi}_0,\eta_0)}{\xi_0 - \bar{\xi}_0} \tag{41}$$

with

$$S_2(\bar{\xi}_0,\eta_0) = \left.\frac{\partial^2 P_1}{\partial \xi_0^2}\right|_{\xi_0=\bar{\xi}_0} \tag{42}$$

$$S_3(\bar{\eta}_0,\xi,\eta) = S_1(\xi_0,\eta_0) - S_1(\bar{\xi}_0,\bar{\eta}_0)\frac{\sqrt{1-\eta_0^2}}{\sqrt{1-\bar{\eta}_0^2}} \tag{43}$$

$$S_4(\eta_0,\xi,\eta) = S_1(\bar{\xi}_0,\eta_0) - S_1(\bar{\xi}_0,\bar{\eta}_0)\frac{\sqrt{1-\eta_0^2}}{\sqrt{1-\bar{\eta}_0^2}} \tag{44}$$

$$\bar{\xi}_0 = \xi - \frac{b}{c}\cot\psi(\eta-\eta_0) \tag{45}$$

$$\bar{\eta}_0 = \eta - \frac{c}{b}\tan\psi(\xi-1) \tag{46}$$

$$\bar{\eta}_{0_2} = \eta - \frac{c}{b}\tan\psi(\xi+1) \tag{47}$$

$$K_1(\xi_0,\eta_0,\xi,\eta) = \frac{b}{c}\frac{}{\sin^2\psi}G_1(\xi_0,\eta_0,\xi,\eta) \tag{48}$$

$$K_2 = \frac{sgn(\eta-\eta_0)}{\sin^2\psi}\frac{b}{c}\ln\left|\frac{\lambda_0}{\lambda_0}\right| \tag{49}$$

where

$$A_3 = \left\{|\sin\psi|\left[b^2(\eta-\eta_0)^2+c^2(\xi-1)^2\right]^{\frac{1}{2}}+b|\eta-\eta_0|-\cos\psi\,\mathrm{sgn}(\eta-\eta_0)\left[c\sin\psi(\xi-1)\right.\right.$$
$$\left.\left.+b\cos\psi(\eta-\eta_0)\right]\right\}\left[c\sin\psi(\xi+1)+b\cos\psi(\eta-\eta_0)\right] \qquad (50)$$

$$A_4 = \left\{|\sin\psi|\left[b^2(\eta-\eta_0)^2+c^2(\xi+1)^2\right]^{\frac{1}{2}}+b|\eta-\eta_0|-\cos\psi\,\mathrm{sgn}(\eta-\eta_0)\left[c\sin\psi(\xi-1)\right.\right.$$
$$\left.\left.+b\cos\psi(\eta-\eta_0)\right]\right\}\left[c\sin\psi(\xi-1)+b\cos\psi(\eta-\eta_0)\right] \qquad (51)$$

$$K_3(\eta_0,\xi,\eta) = \frac{-\frac{b}{c}}{\sin^2\psi}\ln\left|c\sin\psi(\xi-1)+b\cos\psi(\eta-\eta_0)\right|$$
$$-\mathrm{sgn}(\sin\psi)\frac{\cos\psi}{\sin^2\psi}\ln\left|\left[b^2(\eta-\eta_0)^2+c^2(\xi-1)^2\right]^{\frac{1}{2}}+c(\xi-1)\,\mathrm{sgn}(\sin\psi)\right| \qquad (52)$$

$$K_4(\eta_0,\xi,\eta) = \frac{-\frac{b}{c}}{\sin^2\psi}\ln\left|c\sin\psi(\xi+1)+b\cos\psi(\eta-\eta_0)\right|$$
$$+\mathrm{sgn}(\sin\psi)\frac{\cos\psi}{\sin^2\psi}\ln\left|\left[b^2(\eta-\eta_0)^2+c^2(\xi+1)^2\right]^{\frac{1}{2}}+c(\xi+1)\,\mathrm{sgn}(\sin\psi)\right| \qquad (53)$$

$$K_5(\eta_0,\xi,\eta) = \frac{b(\eta-\eta_0)-\sin\psi\left[c^2(\xi-1)^2+b^2(\eta_0-\eta)^2\right]^{\frac{1}{2}}}{\sin\psi(\eta-\eta_0)\left[c\sin\psi(\xi-1)+b\cos\psi(\eta-\eta_0)\right]}$$
$$-\frac{b(\eta-\eta_0)-\sin\psi\left[c^2(\xi+1)^2+b^2(\eta_0-\eta)^2\right]^{\frac{1}{2}}}{\sin\psi(\eta-\eta_0)\left[c\sin\psi(\xi+1)+b\cos\psi(\eta-\eta_0)\right]} \qquad (54)$$

$$K_6(\xi,\eta) = \frac{\frac{b}{c}}{b\cos\psi\sin^2\psi}\left\{\left[b\cos\psi(\eta-1)+c\sin\psi(\xi-1)\right]\ln\left|b\cos\psi(\eta-1)+c\sin\psi(\xi-1)\right|\right.$$
$$-\left[b\cos\psi(\eta+1)+c\sin\psi(\xi-1)\right]\ln\left|b\cos\psi(\eta+1)+c\sin\psi(\xi-1)\right|+2b\cos\psi\Big\}$$
$$-\frac{\frac{b}{c}\cos\psi}{b\sin^2\psi}\left\{2c(1-\xi)\ln 2c(1-\xi)-b(\eta+1)\ln\left|\left[b^2(\eta+1)^2+c^2(\xi-1)^2\right]^{\frac{1}{2}}+c(1-\xi)\right|\right.$$
$$+2b+c(1-\xi)\ln 2\left|\left[b^2(\eta+1)^2+c^2(\xi-1)^2\right]^{\frac{1}{2}}+b(\eta+1)\right|$$
$$\left.+b(\eta-1)\ln\left[b^2(\eta-1)^2+c^2(\xi-1)^2\right]^{\frac{1}{2}}+c(1-\xi)\right|+c(1-\eta)\ln 2\left[b^2(\eta-1)^2+c^2(\xi-1)^2\right]^{\frac{1}{2}}+b(1-\eta)\Big|\Big\} \qquad (55)$$

$$K_7(\xi,\eta) = -\frac{\frac{b}{c}}{b\cos\psi\sin^2\psi}\Big\{[b\cos\psi(\eta-1)+c\sin\psi(\xi+1)]\ln|b\cos\psi(\eta-1)+c\sin\psi(\xi+1)|$$

$$-[b\cos\psi(\eta+1)+c\sin\psi(\xi+1)]\ln|b\cos\psi(\eta+1)+c\sin\psi(\xi+1)|+2b\cos\psi\Big\}$$

$$+\frac{\frac{b}{c}\cos\psi}{b\sin^2\psi}\Big\{2c(1+\xi)\ln 2c(\xi+1)-b(\eta+1)\ln\left|[b^2(\eta+1)^2-c^2(\xi+1)^2]-c(\xi+1)\right|+2b$$

$$+c(\xi+1)\ln 2\left|[b^2(\eta+1)^2+c^2(\xi+1)^2]+b(\eta+1)\right|+b(\eta-1)\ln\left|[b^2(\eta-1)^2+c^2(\xi+1)^2]^{\frac{1}{2}}\right.$$

$$\left.-c(\xi+1)\right|+c(\xi+1)\ln 2\left|[b^2(\eta-1)^2+c^2(\xi+1)^2]^{\frac{1}{2}}+b(1-\eta)\right|\Big\} \qquad (56)$$

Here, K_6 and K_7 have been specialized for the range of ψ of interest.

For convenience, we introduce the following functions:

$$Q_{00} = \left\{\frac{(1-\eta_0^2)-(1-\eta_0^2)}{\bar\eta_0-\eta_0} - 2\bar\eta_0\right\}\frac{1}{\bar\eta_0-\eta_0}$$

$$Q_{01} = \left\{\frac{\eta_0(1-\eta_0^2)-\bar\eta_0(1-\eta_0^2)}{\bar\eta_0-\eta_0} - 3\bar\eta_0^2+1\right\}\frac{1}{\bar\eta_0-\eta_0}$$

$$Q_{02} = \left\{\frac{\eta_0^2(1-\eta_0^2)-\eta_0^2(1-\eta_0^2)}{\bar\eta_0-\eta_0} - 4\bar\eta_0^3+2\bar\eta_0\right\}\frac{1}{\bar\eta_0-\eta_0}$$

$$Q_{03} = \left\{\frac{\eta_0^3(1-\eta_0^2)-\bar\eta_0^3(1-\bar\eta_0^2)}{\bar\eta_0-\eta_0} - 5\bar\eta_0^4+3\bar\eta_0^2\right\}\frac{1}{\bar\eta_0-\eta_0}$$

$$Q_{04} = \left\{\frac{\eta_0^4(1-\eta_0^2)-\bar\eta_0^4(1-\bar\eta_0^2)}{\bar\eta_0-\eta_0} - 6\bar\eta_0^5+4\bar\eta_0^3\right\}\frac{1}{\bar\eta_0-\eta_0}$$

$$Q_{10} = \left\{\frac{(\frac{1}{2}-\frac{1}{2}\eta_0-\frac{1}{2}\eta_0^2)-(\frac{1}{2}-\frac{1}{2}\bar\eta_0-\frac{1}{2}\bar\eta_0^2)}{\bar\eta_0-\eta_0} - \frac{1}{2}(1+\bar\eta_0)\right\}$$

$$R_{00} = 2\bar{\eta}_0$$

$$R_{01} = (3\bar{\eta}_0^2 - 1)$$

$$R_{02} = (4\bar{\eta}_0^3 - 2\bar{\eta}_0)$$

$$R_{03} = (5\bar{\eta}_0^4 - 3\bar{\eta}_0^2)$$

$$R_{04} = (6\bar{\eta}_0^5 - 4\bar{\eta}_0^3)$$

$$\left.\begin{aligned} T_{06} &= \frac{1-\bar{\xi}_{01}}{(1-\xi_{01}^2)^{1/2}} \\ T_{16} &= (1-\bar{\xi}_{01}^2)^{\frac{1}{2}} \\ T_{26} &= \bar{\xi}_{01}(1-\bar{\xi}_{01}^2)^{\frac{1}{2}} \end{aligned}\right\} \quad T_{x6} = 0 \quad \text{for} \quad |\bar{\xi}_{01}| \geq 1$$

$$\left.\begin{aligned} T_{07} &= \frac{1-\bar{\xi}_{02}}{(1-\xi_{02})^{\frac{1}{2}}} \\ T_{17} &= (1-\bar{\xi}_{02}^2)^{\frac{1}{2}} \\ T_{27} &= \bar{\xi}_{02}(1-\xi_{02}^2)^{\frac{1}{2}} \end{aligned}\right\} \quad T_{x7} = 0 \quad \text{for} \quad |\bar{\xi}_{02}| \geq 1$$

$$D_{00} = \left\{ \frac{(1-\xi_p^2) - (1-\bar{\xi}_0^2)}{\bar{\xi}_0 - \xi_p} - 2\xi_p \right\} \frac{1}{\bar{\xi}_0 - \xi_p}$$

$$D_{01} = \left\{ \frac{\xi_p(1-\xi_p^2) - \bar{\xi}_0(1-\bar{\xi}_0^2)}{\bar{\xi}_0 - \xi_p} - 3\bar{\xi}_0^2 + 1 \right\} \frac{1}{\bar{\xi}_0 - \xi_p}$$

$$D_{02} = \left\{ \frac{\xi_p^2(1-\xi_p^2) - \bar{\xi}_0^2(1-\bar{\xi}_0^2)}{\bar{\xi}_0 - \xi_p} - 4\bar{\xi}_0^3 + 2\bar{\xi}_0 \right\} \frac{1}{\bar{\xi}_0 - \xi_p}$$

$$D_{03} = \left\{ \frac{\xi_p^3(1-\xi_p^2) - \bar{\xi}_0^3(1-\bar{\xi}_0^2)}{\bar{\xi}_0 - \xi_p} - 5\bar{\xi}_0^4 + 3\bar{\xi}_0^2 \right\} \frac{1}{\bar{\xi}_0 - \xi_p}$$

$$D_{04} = \left\{ \frac{\xi_p^4(1-\xi_p^2) - \bar{\xi}_0^4(1-\bar{\xi}_0^2)}{\bar{\xi}_0 - \xi_p} - 6\bar{\xi}_0^5 + 4\bar{\xi}_0^3 \right\} \frac{1}{\bar{\xi}_0 - \xi_p}$$

$$D_{30} = \left\{ \frac{\left(\frac{3}{4} - \frac{1}{2}\xi_P - \frac{1}{4}\xi_P^2\right) - \left(\frac{3}{4} - \frac{1}{2}\bar{\xi}_0 - \frac{1}{4}\bar{\xi}_0^2\right)}{\bar{\xi}_0 - \xi_P} - \frac{1}{2}(1+\bar{\xi}_0) \right\} \frac{1}{\bar{\xi}_0 - \xi_P}$$

$$\left.\begin{aligned} M_{06} &= \frac{1-\bar{\eta}_{01}}{(1-\bar{\eta}_{01}^2)^{\frac{1}{2}}} \\ M_{16} &= (1-\bar{\eta}_{01}^2)^{\frac{1}{2}} \\ M_{26} &= \bar{\eta}_{01}(1-\bar{\eta}_{01}^2)^{\frac{1}{2}} \end{aligned}\right\} \qquad M_{x6} = 0 \text{ for } |\bar{\eta}_{01}| \geq 1$$

$$\left.\begin{aligned} M_{07} &= \frac{1-\bar{\eta}_{02}}{(1-\eta_{02}^2)^{\frac{1}{2}}} \\ M_{17} &= (1-\bar{\eta}_{02}^2)^{\frac{1}{2}} \\ M_{27} &= \bar{\eta}_{02}(1-\bar{\eta}_{02}^2)^{\frac{1}{2}} \end{aligned}\right\} \qquad M_{x7} = 0 \text{ for } |\bar{\eta}_{02}| \geq 1$$

$$N_{00} = 2\bar{\xi}_0$$

$$N_{01} = 3\bar{\xi}_0^2 - 1$$

$$N_{02} = 4\bar{\xi}_0^3 - 2\bar{\xi}_0$$

$$N_{03} = 5\bar{\xi}_0^4 - 3\bar{\xi}_0^2$$

$$N_{04} = 6\bar{\xi}_0^5 - 4\bar{\xi}_0^3$$

$$N_{30} = -\frac{1}{2}(1+\bar{\xi}_0)$$

Then the A's and L's can be expressed as follows:

$$A_{00} = -\frac{\pi}{8r\Delta} \sum_{p=1}^{r} \sum_{\beta=1}^{\Delta} (1-\eta_\beta^2)^{\frac{1}{2}} (1-\xi_P) Q_{00} J_1 - \frac{1}{8r} \sum_{p=1}^{r} \Big\{ (1-\xi_P) R_{00} J_2$$

$$+ \left[(1-\xi_P) R_{00} + 2(1-\xi_P^2)^{\frac{1}{2}} T_{06} \right] J_3 + \left[(1-\xi_P) R_{00} - 2(1-\xi_P^2)^{\frac{1}{2}} T_{07} \right] J_4$$

$$+ (1-\xi_P)(1-\bar{\eta}_0^2) J_5 - \frac{1}{4\pi} T_{06} J_6 + \frac{1}{4\pi} T_{07} J_7$$

$$A_{01} = -\frac{1}{8r\mathcal{N}}\sum_{p=1}^{r}\sum_{\beta=1}^{\mathcal{N}}(1-\eta_\beta^2)^{\frac{1}{2}}(1-\xi_p)\,Q_{01}J_1 - \frac{1}{8r}\sum_{p=1}^{r}\Big\{(1-\xi_p)R_{01}J_2$$
$$+\left[(1-\xi_p)R_{01} - 2(1-\xi_p^2)^{\frac{1}{2}}T_{06}\right]J_3 + \left[(1-\xi_p)R_{01} - 2(1-\xi_p^2)^{\frac{1}{2}}T_{07}\right]J_4$$
$$+(1-\xi_p)(1-\bar{\eta}_0^2)\,\eta_0 J_5\Big\} - \frac{1}{4\pi}T_{06}J_6 - \frac{1}{4\pi}T_{07}J_7$$

$$A_{02} = -\frac{\pi}{8r\mathcal{N}}\sum_{p=1}^{r}\sum_{\beta=1}^{\mathcal{N}}(1-\eta_\beta^2)^{\frac{1}{2}}(1-\xi_p)\,Q_{02}J_1 - \frac{1}{8r}\sum_{p=1}^{r}\Big\{(1-\xi_p)R_{02}J_2$$
$$+\left[(1-\xi_p)R_{01} - 2(1-\xi_p^2)^{\frac{1}{2}}T_{06}\right]J_3 + \left[(1-\xi_p)R_{02} - 2(1-\xi_p^2)^{\frac{1}{2}}T_{07}\right]J_4$$
$$+(1-\xi_p)(1-\bar{\eta}_0^2)\,\bar{\eta}_0^2 J_5\Big\} - \frac{1}{4\pi}T_{06}J_6 - \frac{1}{4\pi}T_{07}J_{07}$$

$$A_{03} = -\frac{\pi}{8r\mathcal{N}}\sum_{p=1}^{r}\sum_{\beta=1}^{\mathcal{N}}(1-\eta_\beta^2)^{\frac{1}{2}}(1-\xi_p)\,Q_{03}J_1 - \frac{1}{8r}\sum_{p=1}^{r}\Big\{(1-\xi_p)R_{03}J_2$$
$$+\left[(1-\xi_p)R_{03} - 2(1-\xi_p^2)^{\frac{1}{2}}T_{06}\right]J_3 + \left[(1-\xi_p)R_{03} - 2(1-\xi_p^2)^{\frac{1}{2}}T_{07}\right]J_4$$
$$+(1-\xi_p)(1-\bar{\eta}_0^2)\,\bar{\eta}_0^3 J_5\Big\} - \frac{1}{4\pi}T_{06}J_6 - \frac{1}{4\pi}T_{07}J_7$$

$$A_{04} = -\frac{\pi}{8r\mathcal{N}}\sum_{p=1}^{r}\sum_{\beta=1}^{\mathcal{N}}(1-\eta_\beta^2)^{\frac{1}{2}}(1-\xi_p)\,Q_{04}J_1 - \frac{1}{8r}\sum_{p=1}^{r}\Big\{(1-\xi_p)R_{04}J_2$$
$$+\left[(1-\xi_p)R_{04} + 2(1-\xi_p^2)^{\frac{1}{2}}T_{06}\right]J_3 + \left[(1-\xi_p)R_{04} - 2(1-\xi_p^2)^{\frac{1}{2}}T_{07}\right]J_4$$
$$+(1-\xi_p)(1-\bar{\eta}_0^2)\,\bar{\eta}_0^4 J_5\Big\} - \frac{1}{4\pi}T_{06}J_6 + \frac{1}{4\pi}T_{07}J_7$$

$$A_{10} = -\frac{\pi}{8r\mathcal{N}}\sum_{p=1}^{r}\sum_{\beta=1}^{\mathcal{N}}(1-\eta_\beta^2)^{\frac{1}{2}}(1-\xi_p^2)\,Q_{00}J_1 - \frac{1}{8r}\sum_{p=1}^{r}\Big\{(1-\xi_p^2)R_{00}J_2$$
$$+\left[(1-\xi_p^2)R_{00} + 2(1-\xi_p^2)^{\frac{1}{2}}T_{16}\right]J_3 + \left[(1-\xi_p^2)R_{00} - 2(1-\xi_p^2)^{\frac{1}{2}}T_{17}\right]J_4$$
$$+(1-\xi_p^2)(1-\bar{\eta}_0^2)\,J_5\Big\} - \frac{1}{4\pi}T_{16}J_6 + \frac{1}{4\pi}T_{17}J_7$$

$$A_{11} = -\frac{\pi}{8r\Delta}\sum_{p=1}^{r}\sum_{\beta=1}^{\Delta}(1-\eta_\beta^2)^{\frac{1}{2}}(1-\xi_p^2)\,Q_{01}\,J_1 - \frac{1}{8r}\sum_{p=1}^{r}\Big\{(1-\xi_p^2)\,R_{01}\,J_2$$
$$+\left[(1-\xi_p^2)\,R_{01} - 2(1-\xi_p^2)^{\frac{1}{2}}\,T_{16}\right]J_3 + \left[(1-\xi_p^2)\,R_{01} - 2(1-\xi_p^2)^{\frac{1}{2}}\,T_{17}\right]J_4$$
$$+(1-\xi_p^2)(1-\bar{\eta}_0^2)\,\bar{\eta}_0\,J_5\Big\} - \frac{1}{4\pi}\,T_{16}\,J_6 - \frac{1}{4\pi}\,T_{17}\,J_7$$

$$A_{12} = -\frac{\pi}{8rs}\sum_{p=1}^{r}\sum_{\beta=1}^{\Delta}(1-\eta_\beta^2)^{\frac{1}{2}}(1-\xi_p^2)\,Q_{02}\,J_1 - \frac{1}{8r}\sum_{p=1}^{r}\Big\{(1-\xi_p^2)\,R_{02}\,J_2$$
$$+\left[(1-\xi_p^2)\,R_{02} + 2(1-\xi_p^2)^{\frac{1}{2}}\,T_{16}\right]J_3 + \left[(1-\xi_p^2)\,R_{02} - 2(1-\xi_p^2)^{\frac{1}{2}}\,T_{17}\right]J_4$$
$$+(1-\xi_p^2)(1-\bar{\eta}_0^2)\,\bar{\eta}_0^2\,J_5\Big\} - \frac{1}{4\pi}\,T_{16}\,T_6 + \frac{1}{4\pi}\,T_{17}\,J_7$$

$$A_{13} = -\frac{\pi}{8r\Delta}\sum_{p=1}^{r}\sum_{\beta=1}^{\Delta}(1-\eta_\beta^2)^{\frac{1}{2}}(1-\xi_p^2)\,Q_{03}\,J_1 - \frac{1}{8r}\sum_{p=1}^{r}\Big\{(1-\xi_p^2)\,R_{03}\,J_2$$
$$+\left[(1-\xi_p^2)\,R_{03} - 2(1-\xi_p^2)^{\frac{1}{2}}\,T_{16}\right]J_3 + \left[(1-\xi_p^2)\,R_{03} - 2(1-\xi_p^2)^{\frac{1}{2}}\,T_{17}\right]J_4$$
$$+(1-\xi_p^2)(1-\bar{\eta}_0^2)\,\bar{\eta}_0^3\,J_5\Big\} - \frac{1}{4\pi}\,T_{16}\,J_6 - \frac{1}{4\pi}\,T_{17}\,J_7$$

$$A_{14} = -\frac{\pi}{8r\Delta}\sum_{p=1}^{r}\sum_{\beta=1}^{\Delta}(1-\eta_\beta^2)^{\frac{1}{2}}(1-\xi_p^2)\,Q_{04}\,J_1 - \frac{1}{8r}\sum_{p=1}^{r}\Big\{(1-\xi_p^2)\,R_{04}\,J_2$$
$$+\left[1-\xi_p^2)\,R_{04} + 2(1-\xi_p^2)^{\frac{1}{2}}\,T_{16}\right]J_3 + \left[(1-\xi_p^2)\,R_{04} + 2(1-\xi_p^2)^{\frac{1}{2}}\,T_{17}\right]J_4$$
$$+(1-\xi_p^2)(1-\bar{\eta}_0^2)\,\bar{\eta}_0^4\,J_5\Big\} - \frac{1}{4\pi}\,T_{16}\,J_6 + \frac{1}{4\pi}\,T_{17}\,J_7$$

$$A_{20} = -\frac{\pi}{8r\Delta}\sum_{p=1}^{r}\sum_{\beta=1}^{\Delta}(1-\eta_\beta^2)^{\frac{1}{2}}\,\xi_p(1-\xi_p^2)\,Q_{00}\,J_1 - \frac{1}{8r}\sum_{p=1}^{r}\Big\{\xi_p(1-\xi_p^2)\,R_{01}\,J_2$$
$$+\left[\xi_p(1-\xi_p^2)\,R_{00} + 2(1-\xi_p^2)^{\frac{1}{2}}\,T_{26}\right]J_3 + \left[\xi_p^2(1-\xi_p^2)\,R_{00} - 2(1-\xi_p^2)^{\frac{1}{2}}\,T_{27}\right]J_4$$
$$+\xi_p(1-\xi_p^2)(1-\bar{\eta}_0^2)\,J_5\Big\} - \frac{1}{4\pi}\,T_{26}\,J_6 + \frac{1}{4\pi}\,T_{27}\,J_7$$

$$A_{21} = -\frac{\pi}{8r}\sum_{p=1}^{r}\sum_{\beta=1}^{M}(1-\eta_\beta^2)^{\frac{1}{2}}\xi_p(1-\xi_p^2)Q_{01}J_1 - \frac{1}{8r}\sum_{p=1}^{r}\Big\{\xi_p(1-\xi_p^2)R_{01}J_2$$
$$+\left[\xi_p(1-\xi_p^2)R_{01} - 2(1-\xi_p^2)^{\frac{1}{2}}T_{26}\right]J_3 + \left[\xi_p(1-\xi_p^2)R_{01} - 2(1-\xi_p^2)^{\frac{1}{2}}T_{27}\right]J_4$$
$$+\xi_p(1-\xi_p^2)(1-\bar{\eta}_0^2)\bar{\eta}_0^2 J_5\Big\} - \frac{1}{4\pi}T_{26}J_6 - \frac{1}{4\pi}T_{27}J_7$$

$$A_{22} = -\frac{\pi}{8rM}\sum_{p=1}^{r}\sum_{\beta=1}^{M}(1-\eta_\beta^2)^{\frac{1}{2}}\xi_p(1-\xi_p^2)Q_{02}J_1 - \frac{1}{8r}\sum_{p=1}^{r}\Big\{\xi_p(1-\xi_p^2)R_{02}J_2$$
$$+\left[\xi_p(1-\xi_p^2)R_{02} + 2(1-\xi_p^2)^{\frac{1}{2}}T_{26}\right]J_3 + \left[\xi_p(1-\xi_p^2)R_{02} - 2(1-\xi_p^2)^{\frac{1}{2}}T_{27}\right]J_4$$
$$+\xi_p(1-\xi_p^2)(1-\bar{\eta}_0^2)\bar{\eta}_0^2 J_5\Big\} - \frac{1}{4\pi}T_{26}J_6 + \frac{1}{4\pi}T_{27}J_7$$

$$A_{23} = -\frac{1}{8rs}\sum_{p=1}^{r}\sum_{\beta=1}^{M}(1-\eta_\beta^2)^{\frac{1}{2}}\xi_p(1-\xi_p^2)Q_{03}J_1 - \frac{1}{8r}\sum_{p=1}^{r}\Big\{\xi_p(1-\xi_p^2)R_{03}J_2$$
$$+\left[\xi_p(1-\xi_p^2)R_{03} + 2(1-\xi_p^2)^{\frac{1}{2}}T_{26}\right]J_3 + \left[\xi_p(1-\xi_p^2)R_{03} - 2(1-\xi_p^2)^{\frac{1}{2}}T_{27}\right]J_4$$
$$+\xi_p(1-\xi_p^2)(1-\bar{\eta}_0^2)\bar{\eta}_0^3 J_5\Big\} - \frac{1}{4\pi}T_{26}J_6 - \frac{1}{4\pi}T_{27}J_7$$

$$A_{24} = -\frac{1}{8rM}\sum_{p=1}^{r}\sum_{\beta=1}^{M}(1-\eta_\beta^2)^{\frac{1}{2}}\xi_p(1-\xi_p^2)Q_{04}J_1 - \frac{1}{8r}\sum_{p=1}^{r}\Big\{\xi_p(1-\xi_p^2)R_{04}J_2$$
$$+\left[\xi_p(1-\xi_p^2)R_{04} + 2(1-\xi_p^2)^{\frac{1}{2}}T_{26}\right]J_3 + \left[\xi_p(1-\xi_p^2)R_{04} - 2(1-\xi_p^2)^{\frac{1}{2}}T_{27}\right]J_4$$
$$+\xi_p(1-\xi_p^2)(1-\bar{\eta}_0^2)\bar{\eta}_0^4 J_5\Big\} - \frac{1}{4\pi}T_{26}J_6 + \frac{1}{4\pi}T_{27}J_7$$

$$A_{30} = -\frac{\pi}{8rM}\sum_{p=1}^{r}\sum_{\beta=1}^{M}(1-\eta_\beta^2)^{\frac{1}{2}}(1-\xi_p)Q_{30}J_1 + \frac{1}{8}\sum_{p=1}^{r}\Big\{(1-\xi_p)R_{30}\left[J_2+J_3+J_4\right]$$
$$+T_{07}(1-\xi_p^2)^{\frac{1}{2}}J_4 - (1-\xi_p)\left(\frac{3}{4} - \frac{1}{2}\bar{\eta}_0 - \frac{1}{4}\bar{\eta}_0^2\right)J_5\Big\} - \frac{1}{8\pi}T_{07}J_7$$

$$A_{31} = -\frac{\pi}{8r\Delta}\sum_{p=1}^{r}\sum_{\beta=1}^{\Delta}(1-\eta_\beta^2)^{\frac{1}{2}}(1-\xi_p^2)\,Q_{30}\,J_1 + \frac{1}{8}\sum_{p=1}^{r}\Big\{(1-\xi_p)R_{30}\,[J_2+J_3+J_4]$$

$$-T_{17}(1-\xi_p^2)^{\frac{1}{2}}J_4 - (1-\xi_p^2)\Big(\frac{3}{4}-\frac{1}{2}\bar{\eta}_0-\frac{1}{4}\bar{\eta}_0^2\Big)J_5\Big\} - \frac{1}{8\pi}T_{17}\,J_7$$

$$A_{32} = -\frac{1}{8r\Delta}\sum_{p=1}^{r}\sum_{\beta=1}^{\Delta}(1-\eta_\beta^2)^{\frac{1}{2}}(1-\xi_p^2)\,\xi_p\,Q_{30}\,J_1 + \frac{1}{8}\sum_{p=1}^{r}\Big\{(1-\xi_p^2)R_{30}(J_2+J_3+J_4)$$

$$-T_{27}(1-\xi_p^2)^{\frac{1}{2}}J_4 - \xi_p(1-\xi_p^2)\Big(\frac{3}{4}-\frac{1}{2}\bar{\eta}_0-\frac{1}{4}\bar{\eta}_0^2\Big)J_5\Big\} - \frac{1}{8\pi}T_{27}\,J_7$$

$$L_{00} = -\frac{\pi}{8r\Delta}\sum_{p=1}^{r}\sum_{\beta=1}^{\Delta}(1-\xi_p^2)^{\frac{1}{2}}(1-\eta_\beta)\,D_{00}\,K_1 - \frac{1}{8\Delta}\sum_{\beta=1}^{\Delta}\Big\{N_{00}(1-\eta_\beta)K_2$$

$$+\big[(1-\eta_\beta)N_{00}-2(1-\eta_\beta^2)^{\frac{1}{2}}M_{06}\big]K_3 + \big[(1-\eta_\beta)N_{00}-2(1-\eta_\beta^2)^{\frac{1}{2}}M_{07}\big]K_4$$

$$+(1-\eta_\beta)(1-\bar{\xi}_0^2)K_5\Big\} - \frac{M_{06}K_6}{4\pi} + \frac{M_{07}K_7}{4\pi}$$

$$L_{01} = -\frac{\pi}{8r\Delta}\sum_{p=1}^{r}\sum_{\beta=1}^{\Delta}(1-\xi_p^2)^{\frac{1}{2}}(1-\eta_\beta)\,D_{01}\,K_1 - \frac{1}{8\Delta}\sum_{\beta=1}^{\Delta}\Big\{N_{01}(1-\eta_\beta)K_2$$

$$+\big[(1-\eta_\beta)N_{01}-2(1-\eta_\beta^2)^{\frac{1}{2}}M_{06}\big]K_3 + \big[(1-\eta_\beta)N_{01}-2(1-\eta_\beta^2)^{\frac{1}{2}}M_{07}\big]K_4$$

$$+(1-\eta_\beta)\bar{\xi}_0(1-\bar{\xi}_0^2)K_5\Big\} - \frac{M_{06}K_6}{4\pi} - \frac{M_{07}K_7}{4\pi}$$

$$L_{02} = -\frac{\pi}{8r\Delta}\sum_{p=1}^{r}\sum_{\beta=1}^{\Delta}(1-\xi_p^2)^{\frac{1}{2}}(1-\eta_\beta)\,D_{02}\,K_1 - \frac{1}{8\Delta}\sum_{\beta=1}^{\Delta}\Big\{N_{02}(1-\eta_\beta)K_2$$

$$+\big[(1-\eta_\beta)N_{02}-2(1-\eta_\beta^2)^{\frac{1}{2}}M_{06}\big]K_3 + \big[(1-\eta_\beta)N_{02}+2(1-\eta_\beta^2)^{\frac{1}{2}}M_{07}\big]K_4$$

$$+(1-\eta_\beta)\xi_0^2(1-\bar{\xi}_0^2)K_5\Big\} - \frac{M_{06}K_6}{4\pi} + \frac{M_{07}K_7}{4\pi}$$

$$L_{03} = -\frac{\pi}{8r\Delta}\sum_{p=1}^{r}\sum_{\beta=1}^{\Delta}(1-\xi_p^2)^{\frac{1}{2}}(1-\eta_\beta)\,D_{03}\,K_1 - \frac{1}{8\Delta}\sum_{\beta=1}^{\Delta}\Big\{N_{03}(1-\eta_\beta)K_2$$
$$+\Big[(1-\eta_\beta)N_{03} - 2(1-\eta_\beta^2)^{\frac{1}{2}}M_{06}\Big]K_3 + \Big[(1-\eta_\beta)N_{03} - 2(1-\eta_\beta^2)^{\frac{1}{2}}M_{07}\Big]K_4$$
$$-(1-\eta_\beta)\bar{\xi}_o^2(1-\bar{\xi}_o^2)K_5\Big\} - \frac{M_{06}K_6}{4\pi} - \frac{M_{07}K_7}{4\pi}$$

$$L_{04} = -\frac{\pi}{8r\Delta}\sum_{p=1}^{r}\sum_{\beta=1}^{\Delta}(1-\xi_p^2)^{\frac{1}{2}}(1-\eta_\beta)\,D_{04}\,K_1 - \frac{1}{8\Delta}\sum_{\beta=1}^{\Delta}\Big\{N_{04}(1-\eta_\beta)K_2$$
$$+\Big[(1-\eta_\beta)N_{04} - 2(1-\eta_\beta^2)^{\frac{1}{2}}M_{06}\Big]K_3 + \Big[(1+\eta_\beta)N_{04} + 2(1-\eta_\beta^2)^{\frac{1}{2}}M_{07}\Big]K_4$$
$$+(1-\eta_\beta)\bar{\xi}_o^4(1-\bar{\xi}_o^2)K_5\Big\} - \frac{M_{06}K_6}{4\pi} + \frac{M_{07}K_7}{4\pi}$$

$$L_{10} = -\frac{\pi}{8r\Delta}\sum_{p=1}^{r}\sum_{\beta=1}^{\Delta}(1-\xi_p^2)^{\frac{1}{2}}(1-\eta_\beta^2)\,D_{00}\,K_1 - \frac{1}{8\Delta}\sum_{\beta=1}^{\Delta}\Big\{N_{00}(1-\eta_\beta^2)K_2$$
$$+\Big[(1-\eta_\beta^2)N_{00} - 2(1-\eta_\beta^2)^{\frac{1}{2}}M_{16}\Big]K_3 + \Big[(1-\eta_\beta^2)N_{00} - 2(1-\eta_\beta^2)^{\frac{1}{2}}M_{17}\Big]K_4$$
$$+(1-\eta_\beta^2)(1-\bar{\xi}_o^2)K_5\Big\} - \frac{M_{16}K_6}{4\pi} - \frac{M_{17}K_7}{4\pi}$$

$$L_{11} = -\frac{\pi}{8r\Delta}\sum_{p=1}^{r}\sum_{\beta=1}^{\Delta}(1-\xi_p^2)^{\frac{1}{2}}(1-\eta_\beta^2)\,D_{01}\,K_1 - \frac{1}{8\Delta}\sum_{\beta=1}^{\Delta}\Big\{N_{01}(1-\eta_\beta^2)K_2$$
$$+\Big[(1-\eta_\beta^2)N_{01} - 2(1-\eta_\beta^2)^{\frac{1}{2}}M_{16}\Big]K_3 + \Big[(1-\eta_\beta^2)N_{01} - 2(1-\eta_\beta^2)^{\frac{1}{2}}M_{17}\Big]K_4$$
$$+(1-\eta_\beta^2)\bar{\xi}_o(1-\bar{\xi}_o^2)K_5\Big\} - \frac{M_{16}K_6}{4\pi} - \frac{M_{17}K_7}{4\pi}$$

$$L_{12} = -\frac{\pi}{8r\Delta}\sum_{p=1}^{r}\sum_{\beta=1}^{\Delta}(1-\xi_p^2)^{\frac{1}{2}}(1-\eta_\beta^2)\,D_{02}\,K_1 - \frac{1}{8\Delta}\sum_{\beta=1}^{\Delta}\Big\{N_{02}(1-\eta_\beta^2)K_2$$
$$+\Big[(1-\eta_\beta^2)N_{02} - 2(1-\eta_\beta^2)^{\frac{1}{2}}M_{16}\Big]K_3 + \Big[(1-\eta_\beta^2)N_{02} + 2(1-\eta_\beta^2)^{\frac{1}{2}}M_{17}\Big]K_4$$
$$+(1-\eta_\beta^2)\bar{\xi}_o^2(1-\bar{\xi}_o^2)K_5\Big\} - \frac{M_{16}K_6}{4\pi} + \frac{M_{17}K_7}{4\pi}$$

$$L_{13} = -\frac{\pi}{8r\omega}\sum_{p=1}^{r}\sum_{\beta=1}^{\omega}(1-\xi_p^2)^{\frac{1}{2}}(1-\eta_\beta^2)\,D_{03}K_1 - \frac{1}{8\omega}\sum_{\beta=1}^{\omega}\Big\{N_{03}(1-\eta_\beta^2)K_2$$
$$+\left[(1-\eta_\beta^2)N_{03} - 2(1-\eta_\beta^2)^{\frac{1}{2}}M_{16}\right]K_3 + \left[(1-\eta_\beta^2)N_{03} - 2(1-\eta_\beta^2)^{\frac{1}{2}}M_{17}\right]K_4$$
$$+(1-\eta_\beta^2)\bar{\xi}_0^3(1-\bar{\xi}_0^2)K_5\Big\} - \frac{M_{16}K_6}{4\pi} - \frac{M_{17}K_7}{4\pi}$$

$$L_{14} = -\frac{\pi}{8r\omega}\sum_{p=1}^{r}\sum_{\beta=1}^{\omega}(1-\xi_p^2)^{\frac{1}{2}}(1-\eta_\beta^2)\,D_{03}K_1 - \frac{1}{8\omega}\sum_{\beta=1}^{\omega}\Big\{N_{04}(1-\eta_\beta^2)K_2$$
$$+\left[(1-\eta_\beta^2)N_{04} - 2(1-\eta_\beta^2)^{\frac{1}{2}}M_{16}\right]K_3 + \left[(1-\eta_\beta^2)N_{04} + 2(1-\eta_\beta^2)^{\frac{1}{2}}M_{17}\right]K_4$$
$$+(1-\eta_\beta^2)\bar{\xi}_0^4(1-\bar{\xi}_0^2)K_5\Big\} - \frac{M_{16}K_6}{4\pi} + \frac{M_{17}K_7}{4\pi}$$

$$L_{20} = -\frac{\pi}{8r\omega}\sum_{p=1}^{r}\sum_{\beta=1}^{\omega}(1-\xi_p^2)^{\frac{1}{2}}(1-\eta_\beta^2)\,\eta_\beta\,D_{00}K_1 - \frac{1}{8\omega}\sum_{\beta=1}^{\omega}\Big\{N_{00}\eta_\beta(1-\eta_\beta)K_2$$
$$+\left[\eta_\beta(1-\eta_\beta^2)N_{00} - 2(1-\eta_\beta^2)^{\frac{1}{2}}M_{26}\right]K_3 + \left[\eta_\beta(1-\eta_\beta^2)N_{00} + 2(1-\eta_\beta^2)^{\frac{1}{2}}M_{27}\right]K_4$$
$$+\eta_\beta(1-\eta_\beta^2)(1-\bar{\xi}_0^2)K_5\Big\} - \frac{M_{26}K_6}{4\pi} + \frac{M_{27}K_7}{4\pi}$$

$$L_{21} = -\frac{\pi}{8r\omega}\sum_{p=1}^{r}\sum_{\beta=1}^{\omega}(1-\xi_p^2)^{\frac{1}{2}}\eta_\beta(1-\eta_\beta^2)\,D_{01}K_1 - \frac{1}{8\omega}\sum_{\beta=1}^{\omega}\Big\{N_{01}\eta_\beta(1-\eta_\beta^2)K_2$$
$$+\left[\eta_\beta(1-\eta_\beta^2)N_{01} - 2(1-\eta_\beta^2)^{\frac{1}{2}}M_{26}\right]K_3 + \left[\eta_\beta(1-\eta_\beta^2)N_{01} - 2(1-\eta_\beta^2)^{\frac{1}{2}}M_{27}\right]K_4$$
$$+\eta_\beta(1-\eta_\beta^2)\bar{\xi}_0(1-\bar{\xi}_0^2)K_5\Big\} - \frac{M_{26}K_6}{4\pi} - \frac{M_{27}K_7}{4\pi}$$

$$L_{22} = -\frac{\pi}{8r\omega}\sum_{p=1}^{r}\sum_{\beta=1}^{\omega}(1-\xi_p^2)^{\frac{1}{2}}\eta_\beta(1-\eta_\beta^2)\,D_{02}K_1 - \frac{1}{8\omega}\sum_{\beta=1}^{\omega}\Big\{N_{02}\eta_\beta(1-\eta_\beta^2)K_2$$
$$+\left[\eta_\beta(1-\eta_\beta^2)N_{02} - 2(1-\eta_\beta^2)^{\frac{1}{2}}M_{26}\right]K_3 + \left[\eta_\beta(1-\eta_\beta^2)N_{02} + 3(1-\eta_\beta^2)^{\frac{1}{2}}M_{27}\right]K_4$$
$$+\eta_\beta(1-\eta_\beta^2)\bar{\xi}_0^2(1-\bar{\xi}_0^2)K_5\Big\} - \frac{M_{26}K_6}{4\pi} + \frac{M_{27}K_7}{4\pi}$$

$$L_{23} = -\frac{\pi}{8rM}\sum_{\rho=1}^{r}\sum_{\beta=1}^{M}(1-\xi_\rho^2)^{\frac{1}{2}}\eta_\beta(1-\eta_\beta^2)D_{03}K_1 - \frac{1}{8M}\sum_{\beta=1}^{M}\Big\{N_{03}\eta_\beta(1-\eta_\beta^2)K_2$$
$$+\Big[\eta_\beta(1-\eta_\beta^2)N_{03} - 2(1-\eta_\beta^2)^{\frac{1}{2}}M_{26}\Big]K_3 + \Big[\eta_\beta(1-\eta_\beta^2)N_{03} - 2(1-\eta_\beta^2)^{\frac{1}{2}}M_{27}\Big]K_4$$
$$+\eta_\beta(1-\eta_\beta^2)\bar{\xi}_0^3(1-\bar{\xi}_0^2)K_5\Big\} - \frac{M_{26}K_6}{4\pi} - \frac{M_{27}K_7}{4\pi}$$

$$L_{24} = -\frac{\pi}{8rM}\sum_{\rho=1}^{r}\sum_{\beta=1}^{M}(1-\xi_\rho^2)^{\frac{1}{2}}\eta_\beta(1-\eta_\beta^2)D_{04}K_1 - \frac{1}{8M}\sum_{\beta=1}^{M}\Big\{N_{04}\eta_\beta(1-\eta_\beta^2)K_2$$
$$+\Big[\eta_\beta(1-\eta_\beta^2)N_{04} - 2(1-\eta_\beta^2)^{\frac{1}{2}}M_{26}\Big]K_3 + \Big[\eta_\beta(1-\eta_\beta^2)N_{04} + 2(1-\eta_\beta^2)^{\frac{1}{2}}M_{27}\Big]K_4$$
$$+\eta_\beta(1-\eta_\beta^2)\bar{\xi}_0^4(1-\bar{\xi}_0^2)K_5\Big\} - \frac{M_{26}K_6}{4\pi} + \frac{M_{27}K_7}{4\pi}$$

$$L_{30} = -\frac{\pi}{8rM}\sum_{\rho=1}^{r}\sum_{\beta=1}^{M}(1-\xi_\rho^2)^{\frac{1}{2}}(1-\eta_\beta)D_{30}K_1 + \frac{1}{8M}\sum_{\beta=1}^{M}\Big\{(1-\eta_\beta)N_{30}(K_2+K_3+K_4)$$
$$-(1-\eta_\beta)\Big(\frac{3}{4}-\frac{1}{2}\bar{\xi}_0-\frac{1}{4}\bar{\xi}_0^2\Big)K_5 - M_{06}(1-\eta_\beta^2)^{\frac{1}{2}}K_3\Big\} - \frac{1}{8\pi}M_{06}K_6$$

$$L_{31} = -\frac{\pi}{8rM}\sum_{\rho=1}^{r}\sum_{\beta=1}^{M}(1-\xi_\rho^2)^{\frac{1}{2}}(1-\eta_\beta^2)D_{30}K_1 + \frac{1}{8M}\sum_{\beta=1}^{M}\Big\{(1-\eta_\beta^2)N_{30}(K_2+K_3+K_4)$$
$$-M_{16}(1-\eta_\beta^2)^{\frac{1}{2}}K_3 - (1-\eta_\beta^2)\Big(\frac{3}{4}-\frac{1}{2}\bar{\xi}_0-\frac{1}{4}\bar{\xi}_0^2\Big)K_5\Big\} - \frac{1}{8\pi}M_{16}K_6$$

$$L_{32} = -\frac{\pi}{8rM}\sum_{\rho=1}^{r}\sum_{\beta=1}^{M}(1-\xi_\rho^2)^{\frac{1}{2}}(1-\eta_\beta^2)\eta_\beta D_{30}K_1 + \frac{1}{8M}\sum_{\beta=1}^{M}\Big\{(1-\eta_\beta^2)\eta_\beta N_{30}(K_2+K_3+K_4)$$
$$-M_{26}(1-\eta_\beta^2)^{\frac{1}{2}}K_3 - (1-\eta_\beta^2)\eta_\beta\Big(\frac{3}{4}-\frac{1}{2}\bar{\xi}_0-\frac{1}{4}\bar{\xi}_0^2\Big)K_5\Big\} - \frac{1}{8\pi}M_{26}K_6$$

Unclassified

Security Classification

DOCUMENT CONTROL DATA - R & D

(Security classification of title, body of abstract and indexing annotation must be entered when the overall report is classified)

1. ORIGINATING ACTIVITY (Corporate author)
Cornell Aeronautical Laboratory, Inc.
4455 Genesee Street
Buffalo, New York 14221

2a. REPORT SECURITY CLASSIFICATION
Unclassified

2b. GROUP

3. REPORT TITLE
The Aerodynamic and Aeroelastic Characteristics of a Full-Scale Rotor Blade Stopped in Flight

4. DESCRIPTIVE NOTES (Type of report and inclusive dates)
Final Technical Report

5. AUTHOR(S) (First name, middle initial, last name)
Richard P. White, Jr.

6. REPORT DATE	7a. TOTAL NO. OF PAGES	7b. NO. OF REFS
April 1969	137	18

8a. CONTRACT OR GRANT NO.	9a. ORIGINATOR'S REPORT NUMBER(S)
DA 44-177-AMC-366(T)	USAAVLABS Technical Report 69-7
b. PROJECT NO. Task 1F162204A13902	
c.	9b. OTHER REPORT NO(S) (Any other numbers that may be assigned this report) BB-2296-S-1
d.	

10. DISTRIBUTION STATEMENT
[redacted]

11. SUPPLEMENTARY NOTES	12. SPONSORING MILITARY ACTIVITY
	U.S. Army Aviation Materiel Laboratories Fort Eustis, Virginia

13. ABSTRACT

This report presents the results of a research program to obtain a consistent set of blade strain and air-load data for a blade of a stoppable rotor configuration arbitrarily oriented with respect to the free stream. The research program summarized herein obtained data for such a blade configuration over a wide range of shaft tilt angles, blade pitch angles, and azimuth angles.

DD FORM 1 NOV 68 1473 REPLACES DD FORM 1473, 1 JAN 64, WHICH IS OBSOLETE FOR ARMY USE.

Unclassified

Security Classification

14. KEY WORDS	LINK A		LINK B		LINK C	
	ROLE	WT	ROLE	WT	ROLE	WT
Helicopter rotors						
Stopped rotors						
Rotor blade aerodynamics						
Rotor blade aeroelastics						
Wind-tunnel tests (rotor)						